Improved inspection and micrometrology of embedded structures in multi-layered ceramics

Development of optical coherence tomographic methods and tools

Rong Su

Doctoral Thesis

Stockholm, Sweden 2014

Improved inspection and micrometrology of embedded structures in multi-layered ceramics -- Development of optical coherence tomographic methods and tools

Copyright © Rong Su, 2014

TRITA IIP-14-01
ISSN 1650-1888
ISBN 978-91-7595-090-7

Industrial Metrology and Optics
Department of Production Engineering
KTH Royal Institute of Technology
SE-100 44 Stockholm, Sweden

Printed in 2014 by Universitetsservice US AB

To my parents and Xue

“Nature uses only the longest threads to weave her patterns, so each small piece of her fabric reveals the organization of the entire tapestry.”

Richard Feynman

Abstract

Roll-to-roll manufacturing of micro components based on advanced printing, structuring and lamination of ceramic tapes is rapidly progressing. This large-scale and cost-effective manufacturing process of ceramic micro devices is however prone to hide defects within the visually opaque tape stacks. To achieve a sustainable manufacturing with zero defects in the future, there is an urgent need for reliable inspection systems. The systems to be developed have to perform high-resolution in-process quality control at high speed. Optical coherence tomography (OCT) is a promising technology for detailed in-depth inspection and metrology. Combined with infrared screening of larger areas it can solve the inspection demands in the roll-to-roll ceramic tape processes. In this thesis state-of-art commercial and laboratory OCT systems, operating at the central wavelength of 1.3 µm and 1.7 µm respectively, are evaluated for detecting microchannels, metal prints, defects and delaminations embedded in alumina and zirconia ceramic layers at hundreds of micrometers beneath surfaces.

The effect of surface roughness induced scattering and scattering by pores on the probing radiation, is analyzed by experimentally captured and theoretically simulated OCT images of the ceramic samples, while varying surface roughnesses and operating wavelengths. By extending the Monte Carlo simulations of the OCT response to the mid-infrared the optimal operating wavelength is found to be 4 µm for alumina and 2 µm for zirconia. At these wavelengths we predict a sufficient probing depth of about 1 mm and we demonstrate and discuss the effect of rough surfaces on the detectability of embedded boundaries.

For high-precision measurement a new and automated 3D image processing algorithm for analysis of volumetric OCT data is developed. We show its capability by measuring the geometric dimensions of embedded structures in ceramic layers, extracting features with irregular shapes and detecting geometric deformations. The method demonstrates its suitability for industrial applications by rapid inspection of manufactured samples with high accuracy and robustness.

The new inspection methods we demonstrate are finally analyzed in the context of measurement uncertainty, both in the axial and lateral cases, and reveal that scattering in the sample indeed affects the lateral measurement uncertainty. Two

types of image artefacts are found to be present in OCT images due to multiple reflections between neighboring boundaries and inhomogeneity of refractive index. A wavefront aberration is found in the OCT system with a scanning scheme of two galvo mirrors, and it can be corrected using our image processing algorithm.

Keywords: Metrology, Optical Coherence Tomography, Ceramics, Embedded Structure, Multilayer, Nondestructive Testing, Optical Inspection, Critical Dimension Measurement, Infrared Imaging, Scattering, Mie Calculation, Image Processing, Monte Carlo Simulation.

Acknowledgments

I started my PhD career when Professor Lars Mattsson told me, “I can offer you a job”. That was one of the most important moments in my life as it is now. Then he introduced me to this very interesting and challenging field – Industrial Metrology and Optics. I feel very lucky to have had a supervisor who is internationally renowned for high quality research and has a lot of experience in questioning measurement results and instrument uncertainties. His guidance has helped me to avoid the worst mistakes in my research and he has taken me in the right direction of doing scientific research. Besides this, I received a large degree of freedom in conducting my work, which has trained me in working and thinking independently. His rigorousness definitely helps to increase the scientific values of my publications. What Prof. Mattsson has given to me will for sure benefit the rest of my life.

The other key person I wish to thank is my co-supervisor Dr. Peter Ekberg. I started the first conversation with him by asking questions about a technical problem I had. In the first moment he seemed skeptical about this strange PhD student, but thirty seconds later he completely concentrated on the technical problem. After that, during the past three years, he has been supporting me with his expertise in image processing and he has presented many innovative ideas leading to very fruitful discussions. He has influenced me deeply with his extreme enthusiasm in technology and philosophy of life.

There are many excellent scientists involved in the research behind my thesis. Special thanks go to Dr. Mikhail Kirillin and Dr. Ekaterina Sergeeva at the Laboratory of Biophotonics, Institute of Applied Physics of the Russian Academy of Sciences, for generously sharing their knowledge in the discussion on light scattering theory and Monte Carlo ray tracing method, and their collaboration on the Monte Carlo simulations of OCT images. I would also like to give special thanks to Prof. Arne Roos at the Ångström Laboratory, Uppsala University for providing the spectrophotometers with very good working conditions. Dr. Ernest W. Chang and Prof. Seok H. Yun at the Wellman Center for Photomedicine at Massachusetts General Hospital and Harvard Medical School are greatly acknowledged for their collaboration in letting me have samples measured on their long wavelength optical

coherence tomography (OCT) system. Dr. Michael Leitner at Thorlabs is acknowledged for conducting the spectral-domain OCT tests.

I would also like to thank all partners in the European project Multilayer (FP7-NMP4-2007-214122) who contributed to the success of the project, which was selected by the European Commission for the Horizon 2020 media campaign. In particular I would like to thank Dr. Johanna Stiernstedt, Dr. Anja Haertel, Dr. Petko Petkov, and Dr. Dominik Jurków for providing the ceramic samples and the laser milling technology.

Other researchers and scientists who have shared their experience or supported me in the experimental work are Prof. David Stifter at the Johannes Kepler University of Linz, Dr. Daniel Woods at Michelson Diagnostics, Prof. Zhe Zhao at KTH Materials Science and Engineering, and Ms. Joanna Hornatowska at Innventia AB.

It has been a real pleasure working with Jonny Gustafsson, Bita Daemi, Caroline Hyll, Nils Abramson, Attila Témun, and Richard Lindqvist in the metrology group, and many thanks to all my colleagues in the Department of Production Engineering who create this wonderful working environment.

It would be impossible to get any achievement without love and support from my mom, dad, and my wife Xue. I wish they will always be healthy and happy.

List of appended papers

Paper 1

R. Su, M. Kirillin, D. Jurków, K. Malecha, L. Golonka, and L. Mattsson, “Optical coherence tomography – a potential tool for roughness assessment of free and embedded surfaces of laser-machined alumina ceramic”, peer-reviewed and published in the *Proceedings of the 8th International Conference on Multi-Material Micro Manufacture*, H. Kück, H. Reinecke, and S. Dimov, eds., (Stuttgart, 2011), page 140-144.

> *Su investigated and discovered the effect of surface roughness on OCT detection and the potential of OCT for assessing embedded surfaces. He was also responsible for the oral presentation he gave at the conference and made the draft of the proceedings text.*

Paper 2

R. Su and L. Mattsson, “Evaluation of optical inspection methods for non-destructive assessment of embedded microstructures and defects in ceramic materials”, peer-reviewed and published in the *Proceedings of the 9th International Conference on Multi-Material Micro Manufacture*, H. Noll, N. Adamovic, and S. Dimov, eds., (Vienna, 2012), page 109-112.

> *Su summarized the metrology achievements made in the Multilayer project and gave an oral presentation of it at the conference. Su is the main author.*

Paper 3

R. Su, M. Kirillin, P. Ekberg, A. Roos, E. Sergeeva, and L. Mattsson, “Optical coherence tomography for quality assessment of embedded microchannels in alumina ceramic”, Optics Express, vol. 20, 4603-4618 (2012).

> *Su initiated and established the collaboration with physicists at the Institute of Applied Physics of the Russian Academy of Science for Monte Carlo*

simulation, designed the test samples, conducted the spectrophotometry and OCT experiments, and analyzed the results. Su also participated in the development of the image processing algorithm and the improvement of the simulation. Su is the main author. This paper has been selected for publication in the Virtual Journal for Biomedical Optics, Vol. 7, Iss. 4.

Paper 4

R. Su, E. W. Chang, P. Ekberg, L. Mattsson, and S. H. Yun, "Enhancement of probing depth and measurement accuracy of optical coherence tomography for metrology of multi-layered ceramics", peer-reviewed and published in the *Proceedings of 1st International Symposium on Optical Coherence Tomography for Non-Destructive Testing*, (Linz, 2013), page 71-73.

Su conducted the experiments at Wellman center for photomedicine and investigated the potential of longer wavelength optical coherence tomography for multi-layered ceramics. Su also developed the image processing algorithm for noise reduction in volumetric OCT images and made an oral presentation at the conference. Su is the main author.

Paper 5

M. Kirillin, R. Su, E. Sergeeva, L. Mattsson, and R. Myllyla, "Monte Carlo simulation in optical coherence tomography for quality inspection of materials", peer-reviewed and published in the *Proceedings of 1st International Symposium on Optical Coherence Tomography for Non-Destructive Testing*, (Linz, 2013), page 65-67.

Su contributed to the modification and improvement of the Monte Carlo simulation of OCT images of multi-layered ceramic materials, and gave an oral presentation at the conference.

Paper 6

R. Su, M. Kirillin, E. W. Chang, E. Sergeeva, S. H. Yun, and L. Mattsson, "Perspectives of mid-infrared optical coherence tomography for inspection and micrometrology of industrial ceramics", accepted by Optics Express (2014).

Su modified the light scattering model for characterizing the optical properties of ceramic layers, conducted the OCT experiments, participated in the modification of the Monte Carlo simulation of OCT images, and analyzed the results. Su is the main author.

Paper 7

P. Ekberg, R. Su, E. W. Chang, S. H. Yun, and L. Mattsson, "Fast and accurate metrology of multi-layered ceramic materials by an automated boundary detection algorithm developed for optical coherence tomography data", J. Opt. Soc. Am. A 31, 217-226 (2014).

Su initiated and established the collaboration with scientists at Wellman center for photomedicine, Harvard Medical School, where Su designed and conducted the OCT experiments as a short-term scholar. Su also participated in the development of the image processing algorithm, and analyzed the performance of the algorithm. Su drafted the text jointly with Peter Ekberg. This paper has been selected for publication in the Virtual Journal for Biomedical Optics, Vol. 9, Iss. 4.

Paper 8

R. Su, P. Ekberg, M. Leitner, and L. Mattsson, "Accurate and automated image segmentation of 3D optical coherence tomography data suffering from low signal to noise levels", submitted to IEEE transactions on image processing (2014).

Su developed the major part of the image processing algorithm, designed the experiments at Thorlabs GmbH (Lübeck), and analyzed the results. The method provides a general solution to segmentation and noise reduction problem in OCT and other 3D imaging technologies, e.g. ultrasound imaging. Su is the main author.

Other publications

1. R. Su and L. Mattsson, "Depth profiling in alumina ceramic by optical coherence tomography", peer-reviewed and published in *Proceedings of the 7th International Conference on Multi-Material Micro Manufacture*, B. Fillon, C. Khan-Malek, S. Dimov, ed., (Bourg en Bresse, 2010), page 316–319.

2. Y. Li, R. Su, M. Hedlind, P. Ekberg, T. Kjellberg, and L. Mattsson, "Model based in-process monitoring with optical coherence tomography", Procedia CIRP, Volume 2, 2012, Pages 70–73.

3. R. Su, "Assessment of optical coherence tomography for metrology applications in high-scattering ceramic materials", Licentiate thesis, KTH Royal Institute of Technology, ISBN 978-91-7501-398-5 (June 2012).

Table of contents

1 INTRODUCTION……………………………….. 1

1.1 PROBLEM STATEMENT 3

1.2 METHODOLOGY OF THE THESIS...4

2 BACKGROUND……………………………...5

2.1 CERAMICS PROCESSING 5

2.1.1 Roll-to-roll multi-layered 3D shaping technology...5

2.1.2 Ceramic materials and micro-processing technology 6

2.2 LIGHT SCATTERING IN CERAMICS 7

2.2.1 Light scattering by pores and grains...8

2.2.2 Characterization of light scattering by pores...10

2.2.3 Light scattering by roughness of ceramic surface..14

2.3 METROLOGY OF PORES AND POROSITY IN CERAMICS...17

2.3.1 Techniques of measuring pores 18

2.3.2 In-line transmission method and its modification 19

2.4 NON-DESTRUCTIVE 3D INSPECTION OF CERAMICS...20

2.4.1 Optical coherence tomography 20

2.4.2 Other techniques...23

3 THEORY OF OPTICAL COHERENCE TOMOGRAPHY 25

3.1 THEORY OF TIME-DOMAIN OCT...25

3.2 THEORY OF FOURIER-DOMAIN OCT 31

3.2.1 Spectral domain OCT...35

3.2.2 Swept-source OCT 36

3.3 PROBING DEPTH 37

3.3.1 Scatter-limited probing depth 38

3.3.2 Potential of mid-IR OCT..38

4 MONTE CARLO SIMULATION OF OCT IMAGES 41

4.1 INTRODUCTION 41

4.2 BASIC PRINCIPLE OF THE MONTE CARLO METHOD 41

4.2.1 Sampling of the photon free pathlength 42

4.2.2 Sampling of the scattering angles 43

4.2.3 Geometrical treatment of photon transport...46

4.3 MONTE CARLO SIMULATION OF OCT IMAGES 48
5 PROCESSING OF OCT IMAGES..... 51
5.1 RIDGE DETECTION ALGORITHM 52
5.1.1 Concept 52
5.1.2 Candidate ridge detection 53
5.1.3 Sub-pixel refinement algorithm 54
5.2 3D CORRELATION DETECTION ALGORITHM 56
5.2.1 Concept 56
5.2.2 Method 57
6 EXPERIMENTAL..... 65
6.1 THE ALUMINA AND ZIRCONIA CERAMIC SAMPLES 65
6.1.1 Manufacturing of the ceramic tapes 65
6.1.2 Microstructures 66
6.1.3 Laser milling of the ceramic samples 67
6.1.4 Optical constants 68
6.2 OPTICAL MEASUREMENT 70
6.2.1 Spectrophotometry 70
6.2.2 OCT imaging systems 70
6.2.3 Scanning white light interferometry 72
6.3 NUMERICAL METHODS 72
6.3.1 Mie calculation 72
6.3.2 The Monte Carlo simulation 72
7 EXPERIMENTAL RESULTS 75
7.1 OPTICAL PROPERTIES OF THE CERAMIC SAMPLES 75
7.2 DIMENSIONAL MEASUREMENTS WITH OCT 78
7.2.1 Microchannels in the free surface 79
7.2.2 Embedded microchannels in alumina 80
7.2.3 Embedded microchannels in zirconia 83
7.3 DEFECTS DETECTION 87
7.4 ENHANCED PROBING DEPTH BY 1.7μM OCT 89
8 SIMULATION RESULTS 93
8.1 GEOMETRIC MODELS AND INPUT PARAMETERS 93
8.2 COMPARISONS OF A-SCANS 95
8.3 SIMULATED NEAR- TO MID-IR OCT IMAGES FOR ALUMINA 97
8.4 SIMULATED NEAR- TO MID-IR OCT IMAGES FOR ZIRCONIA 99

9 DISCUSSIONS **103**
9.1 EVALUATION OF THE DEVELOPED IMAGE PROCESSING ALGORITHM 103
9.1.1 Discussion of the terminology *104*
9.1.2 Evaluations based on OCT B-scans *105*
9.1.3 Evaluations based on volumetric OCT data *107*
9.2 MEASUREMENT UNCERTAINTY OF OCT IN CERAMICS 109
9.2.1 Critical dimension (CD) measurement *109*
9.2.2 Ambiguities and errors in OCT imaging *114*
9.3 FUTURE WORK 117
10 CONCLUSION **119**
REFERENCES **122**

1 Introduction

Back in the middle of 19th century, the rotary printing press (shown in Fig. 1) was invented by Richard March Hoe. By letting the images to be printed be attached to a cylinder millions of copies of a page could be reproduced in a single day. Today, thanks to the continuous revolution of technology mass production of newspapers with much lower price can be run at a much faster pace.

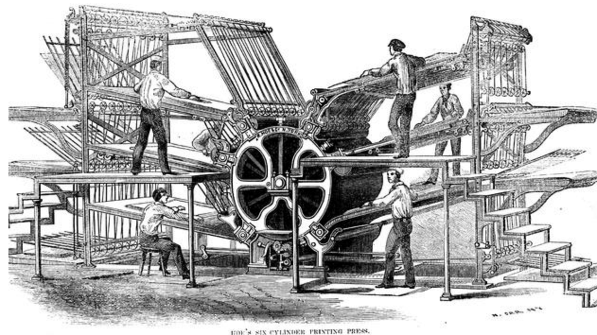

Fig. 1. Early rotary printing press from the 1860s. [1]

Based on a similar concept but using different materials, the advanced “roll-to-roll multi-material layered 3D shaping technology” is aiming for manufacturing of multi-functional micro devices with complex 3D structures [2].

Ceramics such as alumina and zirconia are selected as the basic building materials because they have unique properties of high thermal and chemical stability, mechanical and electrical strength, and electric resistivity [3].

The outputs of this technology may provide a solution to the manufacturing for the emerging markets with components such as micro-fluidic devices for medical applications or micro-reactions, integrated devices packaged with embedded micro-electro-mechanical systems (MEMS) and optical fibers, bio-reactors, microwave devices for terahertz applications, high efficient cooling systems (integrated heat pipes or micro heat-exchangers), micro sources of energy and different types of sensors at very large scale. Meanwhile, the manufacturing costs will be much reduced.

In parallel with the development of roll-to-roll manufacturing technology, there is a high demand for quality inspection and process control utilizing non-destructive, non-contact, high-resolution, and in-process 3D monitoring systems. A potential inspection system suggested by our metrology group in the Multilayer project is shown in Fig. 2. For ceramic micro devices the possible features to be inspected are surface roughness, geometric dimensions of the machined or printed micro parts, embedded defects, cracks, delaminated layers, inclusions and embedded features after assembly process.

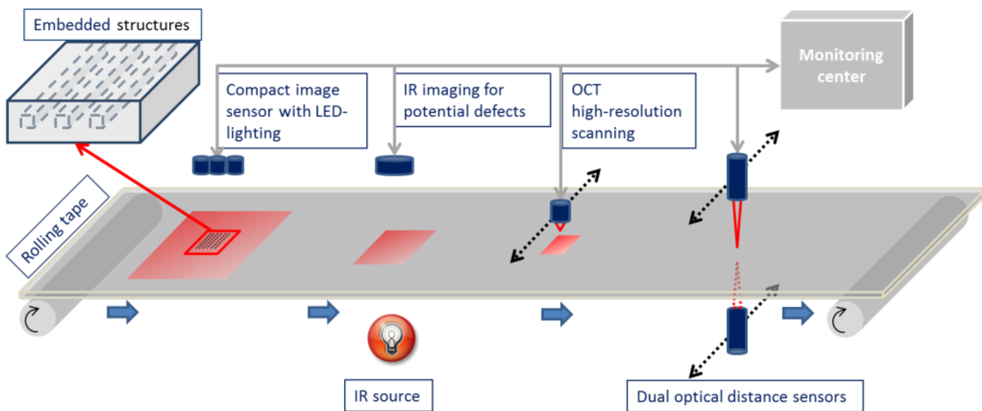

Fig. 2. Schematic illustration of a potential quality inspection and process control system for the rolled multi-material layered 3D shaping technology of ceramic micro devices.

Good measurements and monitoring can improve the product quality and tolerances effectively. It also saves unnecessary cost due to poor performance and shorter life cycle. Another significant benefit of developing new measurement technologies is to provide a fast feedback loop for reconfigurations of materials and

features at the early stage, during the research and development process of new ceramic micro devices.

The major inspection problem is that the ceramic materials appear opaque in the visible wavelength range because of the strong light scattering within the material. Thus, conventional measurement techniques cannot verify the embedded features and defects without significant errors. A promising technology, investigated and developed in this thesis, is the recently invented optical coherence tomography (OCT) owing to the development of the modern optical communication technology and advanced photonic devices such as broadband light sources and detectors working at near infrared (IR) wavelengths. This technology provides a 3D imaging modality of materials similar to e.g. ultrasound. However, until recently OCT was mainly focused on the biomedical area, and OCT has not been optimized for industrial materials. Also, because of the limited time passed since its invention, there is a lack of knowledge about the measurement uncertainty of this technology, particularly when the dimensional tolerances approach micrometer level.

In order to enhance the knowledge in this part this thesis contributes with a feasibility analysis of the technique to reveal its potential as a metrology tool. Several optical coherence tomography microscopes have therefore been thoroughly modelled and analyzed in this work and new methods have been devised on improving the technique and its image analysis to be useful for quality inspection and in-process monitoring in ceramic micro manufacturing. In addition a discussion is presented on the possible sources of measurement uncertainty in OCT regarding different optical phenomena in the high scatter materials.

This thesis is laid out by starting with the background information regarding micro processing of ceramic materials, the scattering models of microstructures and roughnesses. Then the optical inspection technologies for embedded structures in materials, the theory of OCT, Monte Carlo simulation of OCT images, and the dedicated image processing method are described in detail. The experimental and simulation results are finally presented before a discussion of measurement uncertainty in OCT when applied to scattering materials.

1.1 Problem statement

As indicated in the introduction above a dedicated OCT system for industrial ceramic materials does not exist today, and the measurement uncertainty is also unknown. This leads to two problems:

1) The penetration depth of light/electromagnetic waves in ceramics limits the detection of embedded features and defects using current OCT systems. What can be improved to solve that problem?

2) How does the interaction between the incident radiation and the ceramic materials/interfaces influence the OCT measurement uncertainty? That is an unsolved question so far.

1.2 Methodology of the thesis

The fundamental assumptions of this thesis, which is performed in the area of metrology, the science of measurement, and optics, are based on physics and mathematics. Therefore, we follow the common methodology of experimental physics research, where the problems and hypotheses are firstly formulated, and then the consequences of the hypotheses are tested by both experiments and simulations. The hypotheses are:

1) There exist certain OCT wavelengths regions that optimize the light/electromagnetic wave penetration in alumina and zirconia ceramic materials and therefore improve the detection of embedded features and defects;

2) Optical phenomena, such as light scattering, diffraction, refraction, and reflection may cause measurement uncertainty in OCT;

3) Dedicated image processing algorithm may enhance the accuracy of dimensional metrology using OCT.

2 Background

2.1 Ceramics processing

2.1.1 Roll-to-roll multi-layered 3D shaping technology

The latest development of roll-to-roll manufacturing technology can be found in several European projects in the past 6 years for different materials and applications, such as high efficiency flexible solar modules [4], polymer and printed electronics [5], organic electroluminescence (OLED) for intelligent lighting applications [6], wireless sensor devices on paper surfaces [7], flexible organic tandem cells [8], and the advanced ceramic MEMS in this thesis [9]. The common goal of these projects is to develop a set of solutions for the large-scale and cost-effective production. The concept of the Multilayer project, on which this thesis is largely based, is demonstrated in Fig. 3.

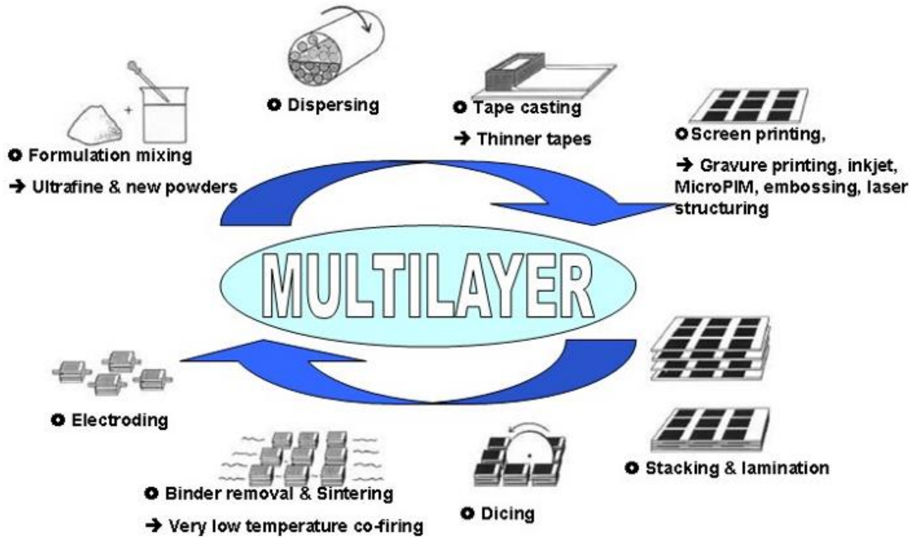

Fig. 3. Concept of the roll-to-roll manufacturing routes of the ceramic micro devices in the Multilayer project. The major processes include tape casting, tape structuring, printing, stacking and lamination, and sintering. [9]

2.1.2 Ceramic materials and micro-processing technology

The selected ceramic materials in this thesis are alumina (aluminum oxide, Al_2O_3) and zirconia (zirconium dioxide, ZrO_2). These materials have very high melting point (>2000 °C), high mechanical hardness, resistance to abrasive wear and good dimensional stability. They also possess high electric resistivity, and are stable against attacks from most chemicals and can be used in harmful environments. Alumina, which has a relatively high thermal conductivity, can be applied in cooling systems for heat dissipation, whereas zirconia with a low thermal conductivity can be applied as a high thermal resistance coating.

The manufacturing of tape based alumina and zirconia ceramic samples includes three important processes: tape casting, tape structuring and sintering. Tape casting is a forming technique for producing a thin, flat ceramic layer in green state (a ceramic before it is fired) from a slurry where the ceramic powder particles are

suspended [10]. Usually a binder that holds the powder together is added. The binder provides the plasticity for forming and also the strength for handling the tape in the green state.

Tape structuring is carried out on the green state. Various technologies can be applied, such as punching, embossing, laser-milling, and in-mold labeling. More details about the structuring technologies may be found in the references [11-16].

The process of transforming ceramic powder particles into dense products below the melting point is called sintering [3]. For example, in this thesis the ceramic green state tapes with binders are sintered in furnaces at very high temperatures. During the sintering process the binder is burnt away and the crystalline alumina or zirconia grains grow. Pores filled by gas (air in this thesis) may remain in the dense ceramic after sintering.

2.2 Light scattering in ceramics

Ceramics are not unfamiliar to us and many have used ceramic plates for carrying foods. The highly-dense polycrystalline alumina and zirconia samples used in this thesis have the similar white appearance as the ceramic plates, but are much smaller in sizes (a few square centimeters) and thicknesses (< 0.5mm).

The white appearance is the result of strong light scattering in the visible wavelengths region. The origin of the scattering may be residual pores after sintering, crystalline grains, surface roughness and impurities. Many researchers have investigated the optical properties of ceramics and different models have been established to relate light scattering to the microstructural properties of ceramics. However, there is no general solution that can explain the scattering mechanism in different kinds of ceramics. Even if we restrict ourselves to just alumina the electromagnetic scattering models have different validity regions because the microstructure of the material can be significantly influenced by the ceramic powders, binder systems, sintering temperatures, sintering time and many other factors. In the following section we will focus on the scattering in highly-dense sintered alumina and zirconia ceramic materials for the roll-to-roll micromanufacturing.

2.2.1 Light scattering by pores and grains

So far, the most successful models are based on the assumptions that the light scattering in dense alumina and zirconia ceramics is caused by residual pores and/or by the birefringence of crystalline grains. The schematic microstructure of dense alumina and zirconia ceramic are illustrated in Fig. 4, as well as the light scattering by birefringence and pores.

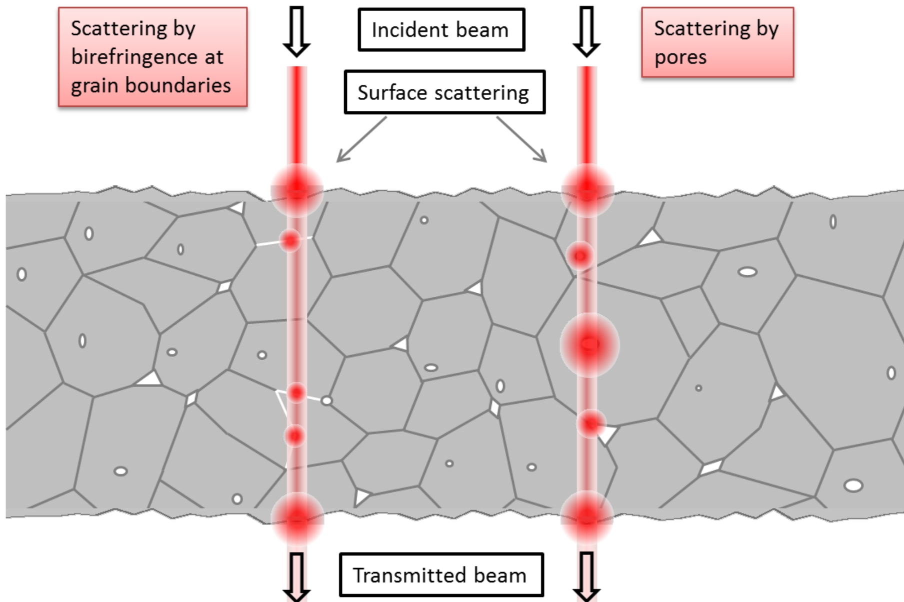

Fig. 4. Schematic illustration of the microstructure of dense alumina and zirconia ceramic and the light scattering. The cross sectional view of a thin ceramic layer is shown, where the polygons represent the crystalline grains and the small white regions represent the pores filled by air. The pores existing within grains are usually close to spheres, and those present at grain corners may have arbitrary shapes. The diffuse red circular areas represent scattering events that occur. The sizes of these circles illustrate the strength of the scattering. An un-polarized ray of light will be scattered in all directions, but the angular dependence of the scattered intensity may not be isotropic as will be discussed later in section 2.2.2 and 4.2.2.

The light scattering by pores is caused by the large differences of the refractive indices between the ceramic material and air. The strength of the scattering is affected by the pore sizes and its volumetric concentration which is called porosity. The light scattering caused by birefringence is due to the small refractive index change at the interfaces of crystallites because of the anisotropic orientations of the optical axis of the crystalline grains. In this case the strength of the scattering is related to the number of grains that the ray of light passes and the average difference of refractive index at the grain boundaries. The existence of extremely large grains may lead to light scattering in the anomalous diffraction regime and weaken the mechanical strength, but the probability of extremely large grains is small in our ceramic samples thanks to the progress made in sintering technology, by which the sizes of pores and grains can be made comparable to or even smaller than the wavelength of the incident radiation.

Three models have been used in the literature to evaluate the strength and angular distribution of light scattering by pores and birefringence in alumina and zirconia ceramics. The Rayleigh scattering model is an approximation that refers to light scattering by small particles i.e. pores and grains that are much smaller than the incident wavelength. This is the so-called Rayleigh regime and in the visible region this model is restricted to pore and grain sizes in nanometer scale, which is not the case in our ceramic samples. For alumina ceramics the more common Rayleigh-Gans-Debye (RGD) approximation is used to model the light scattering by the birefringence of crystalline grains where the average difference of refractive indices at the grain boundaries is around 0.005 [17,18]. However, this model is found to be invalid for zirconia where the birefringence is much larger, around 0.03-0.04 [19].

The model providing a rigorous mathematical solution to electromagnetic scattering by homogeneous and isotropic spheres is often referred to as Mie theory, named after the German physicist Gustav Mie [20]. The original paper by Mie in 1908 described how to compute light scattering by spherical particles with arbitrary size using the classical Maxwell equations. This is a general numerical solution that includes Rayleigh and RGD approximations as special cases, although Mie scattering regime is usually referred to as the regime where the particle size is comparable to the wavelength. Thanks to the progress of modern computers the extreme demand of computational power is no longer a problem. Today, a number of algorithms and programs are available, and a full description of the theory can

also be found, e.g. by van de Hulst [21] and Bohren [22]. The theory has also been extended to be applicable for non-spherical and polydisperse particles [23].

It has been shown that Mie theory considering polydisperse spherical pores and grains with an analytic size distribution are suitable scattering models for the sintered alumina and zirconia ceramic samples [19,24-26]. In this thesis the porosities of the samples are larger than 0.2%, and the total grain boundary scattering is around a few percent of the scattering induced by the pores. Thus, the grain-to-grain scattering is negligible in this thesis.

2.2.2 Characterization of light scattering by pores

Light scattering in ceramics is a complex phenomenon, and this section is focused on how to characterize and measure it. The method of calculating the scattering by an air-filled pore is equivalent to that of the scattering from a particle in air [27].

It has been shown that light absorption is negligible in the wavelength region from 0.5μm to 5μm for sintered alumina and zirconia ceramics [19,25]. The total light extinction is therefore determined by scattering only at these wavelengths. The light scattering due to the presence of pores in the sintered highly-dense alumina and zirconia can be characterized numerically by the scattering cross section C_{sca}. Generally speaking, the scattering cross section of a single particle can be determined by measuring the received optical power with and without the particle interposed between the light source and the detector. As shown in Fig. 5, the net effect is equivalent to that the particle is casting a shadow on the detector A, and reducing the detecting area by the area C_{sca} [22,23].

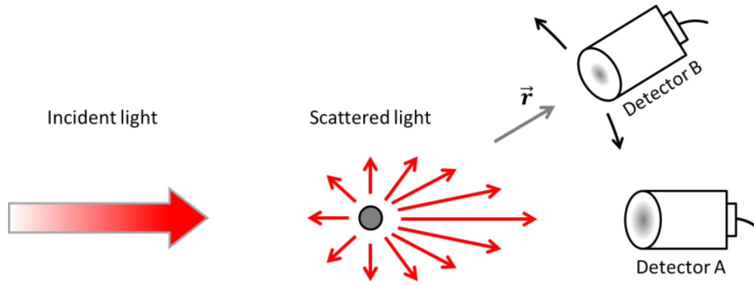

Fig. 5. Measurement of the light scattering by a small particle. The scattering cross section C_{sca} is characterized by the detector A. The angular distribution of the scattering is measured by the detector B.

This area C_{sca} is not simply given by the geometrical projection area of the particle $G_A = \pi r^2$ (where r is the particle radius), but can be greater or much smaller than G_A. A dimensionless quantity called the efficiency factor for scattering Q_{sca} is defined as [23]

$$Q_{sca} = \frac{C_{sca}}{G_A} \tag{2.1}$$

The differential scattering cross section $\mathrm{d}C_{sca}(\hat{\boldsymbol{r}})$ describes the power scattered into unit solid angle about a certain direction $\hat{\boldsymbol{r}}$ per incident power, and can be determined from the measured intensity in detector B in Fig. 5. The angular distribution of the scattered light can be measured by placing detector B anywhere around the particle, i.e. measurement of $\mathrm{d}C_{sca}(\hat{\boldsymbol{r}})$ around 4π sr.

The obtained angular distribution function $\mathrm{p}(\hat{\boldsymbol{r}})$ is called the phase function. It is dimensionless and normalized to the total scattering cross section C_{sca} and is defined as

$$\mathrm{p}(\hat{\boldsymbol{r}}) = \frac{\mathrm{d}C_{sca}(\hat{\boldsymbol{r}})}{C_{sca}} \tag{2.2}$$

The phase function can be seen as the probability density function of the light being scattered into a unit solid angle about a certain direction. It is normalized so that the integral over 4π sr is unity

$$\int_0^{4\pi} \mathrm{p}(\hat{\boldsymbol{r}})\mathrm{d}\hat{\boldsymbol{r}} = \int_0^{4\pi} \frac{\mathrm{d}C_{sca}(\hat{\boldsymbol{r}})}{C_{sca}} \mathrm{d}\hat{\boldsymbol{r}} = 1 \tag{2.3}$$

There are some analytical functions that approximate the phase functions of real particles, e.g. the Henyey-Greenstein phase function which will be described later in section 4.2.2.

Since a large number of pores exist in the ceramic materials the case with scattering by a group of particles must be considered. The prerequisite of the linear combination of the scattering by each particle is the single-scattering approximation [23], which means the particle positions are sufficiently random. So, the total scattering cross section of the volume is obtained as

$$C_{sca} = C_{sca,1} + C_{sca,2} + C_{sca,3} + \cdots C_{sca,\mathrm{N}} \tag{2.4}$$

$$C_{sca} = \sum_{i=1}^{N} C_{sca,i} \tag{2.5}$$

where i is the index of each particle in the volume and N is the total number of the particles. $C_{sca,i}$ represents the scattering cross section of the ith particle. Since the ceramic material has a volume, the total C_{sca} per unit volume V, which is called scattering coefficient μ_s, is calculated as

$$\mu_s = \frac{N}{V} C_{sca} \tag{2.6}$$

The number concentration of pores N/V can also be expressed by the porosity P_V and the volume of each pore V_{pore} as

$$\frac{N}{V} = \frac{P_V}{V_{pore}} \tag{2.7}$$

So equation (2.6) can be rewritten as

$$\mu_s = \frac{3}{4} \frac{P_V}{\pi r^3} C_{sca} \tag{2.8}$$

where r is the pore radius. Note that the unit of μ_s is the reciprocal of length, and the product of μ_s and the thickness of the ceramic layer is a unit-less value that relates to the light scattering directly.

Mie theory allows the calculation of C_{sca} and therefore Q_{sca}. The latter depends on the refractive indices of the pores and the surrounding ceramics, the wavelength, and the sizes of the pores. The full mathematical description can be found elsewhere [21,22].

For the ceramic samples considered in this thesis the lognormal size distribution of pores is assumed, i.e. the probability density function $f(r)$ is

$$f(r) = \frac{1}{r\sqrt{2\pi}\sigma} \exp\left[-\frac{(\ln r - \ln r_m)^2}{2\sigma^2}\right] \tag{2.9}$$

where r_m and σ corresponds to the median and standard deviation of the distribution. The total scattering cross section of the volume in equation (2.5) is then calculated as the ensemble-averaged cross section

$$\langle C_{sca} \rangle = \sum_i p_i C_{sca}(r_i) \tag{2.10}$$

where p_i is the probability of the pores with the radius r_i, and $C_{sca}(r_i)$ is the corresponding scattering cross section. The mean scattering coefficient $\langle \mu_s \rangle$ is calculated as

$$\langle \mu_s \rangle = \frac{P_V}{\langle V_{pore} \rangle} \langle C_{sca} \rangle \tag{2.11}$$

where $\langle V_{pore} \rangle$ is the expected value of the pore volumes,

$$\langle V_{pore} \rangle = \frac{4}{3}\pi \int_0^\infty r^3 f(r) \mathrm{d}r \tag{2.12}$$

The mean scattering coefficient $\langle \mu_s \rangle$ will be used later in section 2.3.2 when the in-line transmission method is introduced to experimentally assess the optical properties of the ceramic samples.

The lognormal size distribution or a zeroth order lognormal distribution [25] of pores has been empirically found suitable for the sintered ceramics. Other distribution functions are also possible to be employed to calculate the ensemble-averaged scattering. The effect of increasing the width of the size distribution σ on the scattering efficiency is simulated in section 9.2 of [23], and the effect of the lognormal-distributed polydisperse pores in sintered alumina on scattering has been

shown by Peelen [26]. Here, these effects are schematically illustrated in Fig. 6 for the alumina and zirconia ceramics.

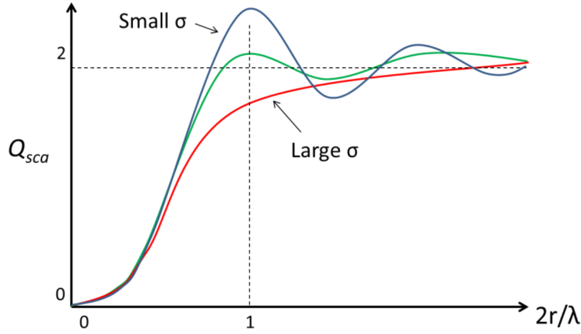

Fig. 6. Schematic plot of the effects of averaging over pores sizes for the lognormal distribution. The horizontal axis represents the spherical pore size relative to the wavelength λ, i.e. the ratio of pore diameter and wavelength. The vertical axis represents the scattering efficiency Q_{sca} as defined in equation ($Q_{sca} = C_{sca}/G_A$) which is a dimensionless quantity correlated to the scattered power. The blue, green, and red lines show the calculations with relatively small, intermediate, and relatively large width of the pore size distribution σ, respectively.

As shown in Fig. 6, with a relatively small σ the blue line shows the scattering from almost identical spherical pores, where the resonance effect is pronounced and particularly strong scattering occurs when the pore diameter is comparable to the wavelength, $2r/\lambda \sim 1$. The position of the strongest scattering peak also depends on the relative refractive index between the pore and the ceramic medium, hence the peak can show up at a position larger than or smaller than $2r/\lambda = 1$. An intermediate σ means that the pores differ in sizes, so the resonance effect is less pronounced. As shown by the red line, this effect is averaged out with a relatively large σ when the pores sizes are much dispersed. Another effect is that $Q_{sca} \rightarrow 2$ as $2r/\lambda \rightarrow \infty$, which is within the domain of geometrical optics approximation.

2.2.3 Light scattering by roughness of ceramic surface

If the ceramic sample is not polished on its surfaces or the polishing is not fine enough, light scattering caused by the surfaces has to be taken into account when

measuring embedded features in the material by the OCT technique. Thus, it is important to understand how to evaluate the surface scattering for ceramics.

Light scattering by surface roughness has been studied intensively over the last century, and is an important issue in optical imaging. Surface scattering effects can be considered as a diffraction phenomenon due to random height distributions of surface microtopographic features. Most natural and processed surfaces possess roughnesses, irregularities or characteristic features that scatter light. Generally speaking, the scattered radiant power is related to the magnitude of the random height deviation of a surface, and the angular distribution of the scattered light is determined by the distribution of the spatial frequency spectrum. A good introduction on light scattering and surface roughness can be found in [28].

Light scattering from a known surface may be predicted by several approximate scattering theories that are available in the literature and each has its limitations and validity conditions [29]. The bi-directional reflectance distribution function (BRDF) is defined as the ratio of the scattered radiance and the incident irradiance, and is mostly used for representing scattering measurements. The Rayleigh-Rice theory can be applied for calculating scattering from smooth surfaces (roughness is much smaller than the wavelength) for arbitrary incident and scattering angles. The Kirchhoff theory is valid for small-angle incident and scattering from rougher surfaces. The generalized Harvey-Shack theory based on a linear-systems approach is found to be identical to the modified Kirchhoff theory and is valid for both smooth and rough surfaces at large incident and scatter angles [29].

A few researchers have used the Kirchhoff theory for predicting light scattering from dielectric rough surfaces in both reflection and transmission directions, and found good agreements with experimental results [30-32]. This theory is considered in this thesis for the alumina and zirconia ceramics that are dielectric in the wavelength regions of interest.

It has been shown that surface roughness calculated from scattering measurements is comparable with roughness measured directly by profiling methods if the comparisons are made using the same spatial wavelengths and lateral resolutions [28]. The total integrated scattering (TIS) measured with simple instrumentation relates the root-mean-square (rms) roughness in a straightforward way to the total amount of scattered light out of the specular reflection direction. A general expression for the TIS from a conductive surface is [29]

$$TIS = 1 - \exp\left[-\left(\frac{4\pi\delta_{rms}\cos\theta_i}{\lambda}\right)^2\right] \tag{2.13}$$

where δ_{rms} is the rms roughness, θ_i is the incident angle, and λ is the wavelength. The exponential term in this equation indicates the power remains in the specular reflection. If the surface is not supersmooth this term can be calculated as the ratio of the measured specular reflectance R_S and total reflectance R_0 [28]

$$\frac{R_S}{R_0} = \exp\left[-\left(\frac{4\pi\delta_{rms}\cos\theta_i}{\lambda}\right)^2\right] \tag{2.14}$$

Now we restrict the surface scattering problem to the dense alumina and zirconia ceramics where the surface roughness is mainly given by the microtopography of the crystalline grains in the surface. The schematics shown in Fig. 7 demonstrate how the light is scattered from a surface of dense alumina and zirconia ceramic material. The specular components of reflected and transmitted light are reduced and turn into diffuse reflection and transmission.

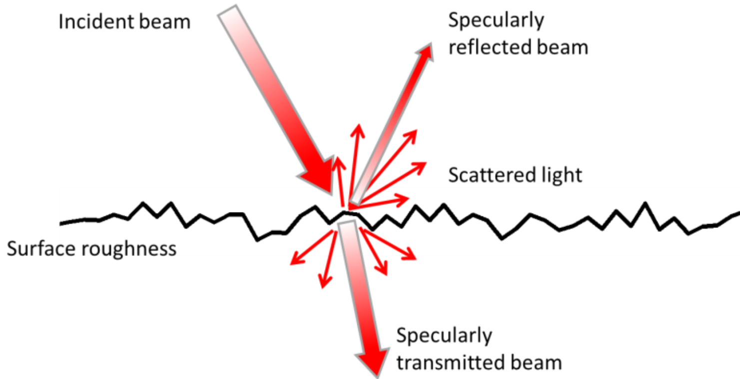

Fig. 7. Schematic illustration of the light scattering that occurs at the interface between air and ceramic material due to surface roughness.

The reflectance and transmittance of a supersmooth ceramic surface at normal incidence can be approximated by the Fresnel reflectance R_F and transmittance T_F

$$R_0 \approx R_F = \frac{(1-n)^2}{(1+n)^2} \tag{2.15}$$

$$T_0 \approx T_F = 1 - R_F \tag{2.16}$$

where n is the refractive index of the ceramic material.

Now substituting R_0 by R_F in equation (2.14), the power that remains in the specular reflection from a ceramic surface at normal incidence from air can be expressed as

$$R_S = R_F \exp\left[-\left(\frac{4\pi\delta_{rms}}{\lambda}\right)^2\right] \tag{2.17}$$

Furthermore, as the validity of the scalar scattering theory for dielectric rough surfaces has been shown in [30-32], the power that remains in the specular transmission from a ceramic surface at normal incidence from air to the material is expressed as

$$T_S = T_F \exp\left[-\left(\frac{2\pi\delta_{rms}}{\lambda}\right)^2 (1-n)^2\right] \tag{2.18}$$

Assuming a normal incident beam with a wavelength of 1 μm (in the air) on an alumina ceramic surface with the root-mean-square (rms) roughness of 100nm, this will result in 80% and 20% loss of the specular reflectance and transmittance, respectively. The losses could be larger when the beam is incident from the material to air due to that the wavelength is shorter in the material. We know that the OCT detection of embedded structures in a scattering medium relies on the ballistic photons. Therefore, surface scattering must be considered in optical coherence tomography for ceramic materials.

2.3 Metrology of pores and porosity in ceramics

By now we have shown how to characterize light scattering from known microstructures of ceramic materials and how to tackle surface roughness and its influence on the specular reflectance. However, the quantitative microstructural information needed is extremely difficult to obtain accurately because the pores are in the sub-micrometer scale. In this section we review several techniques used to measure the statistics of the pores and we also present the modified in-line transmission method in detail that relates transmission losses to the scattering.

2.3.1 Techniques of measuring pores

It is possible to obtain areal microstructural information by measuring on microscope images of a prepared cross section of the ceramic material, e.g. by using micrographs from a scanning electron microscope (SEM), as shown in Fig. 8. However, without proper calibration of the scale bar in a SEM image, obtained under identical conditions regarding surface charging effects and magnification, one cannot expect high quality dimensional measures [33]. It is also un-clear what threshold should be used for extracting the pores edges from the gray scale image. In addition, the 3D size distributions of the pores and grains cannot be directly obtained from the 2D planar images. Some correction method must be used which is referred to as ceramography in ceramics [34], analogous to metallography in metal [35,36], which have fundamental relationships with stereology [37].

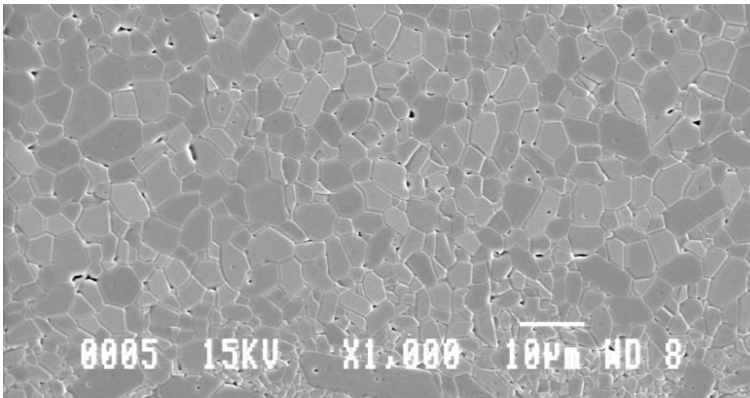

Fig. 8. SEM image of the prepared cross-section of an alumina ceramic sample. Pores appear as the small black areas in the image. Image courtesy of Lars Eklund at Swerea IVF.

3D measurement of pores can be done by X-ray computed microtomography (X-ray μCT) [38,39] and focused ion beam (FIB) nano-tomography [40]. However, the resolution of X-ray μCT is limited in micrometer scale with a sample volume of a few mm^3. The FIB tomography provides nanometer resolution but with an extremely small sample size in the order of μm^3, where large pores may not be detected. Moreover, both techniques are very complicated and expensive.

A simple optical method can be used to retrieve the pore size distribution and porosity by fitting theoretical light scattering, calculated by Mie theory, to the experimental scattering data. The pioneers of that technique, Peelen and Metselaar, fitted the measured in-line transmittance (specular transmittance) curves of sintered alumina layers with the calculated curves [25,26]. They assumed spherical pores with a lognormal size distribution and treated the porosity, and the peak position and width of the distribution as variables. Besides, a similar method has been applied for zirconia ceramic material [24]. The details of this method will be given in next sub-section because it is also used in this thesis.

An alternative was presented by Manara et al. They calculated the light scattering from the measured total transmission and reflection (including both diffuse and specular components) by solving the radiative transfer equation (RTE) using a three-flux approximation [41]. Then they fitted the result to the theoretical light scattering calculated by Mie theory to determine the pore size distribution and porosity of alumina ceramic layers with the thickness of around half millimeters. It was mentioned that the two-flux approximation, e.g. Kubelka-Munk theory [42] does not work well for large optical thicknesses.

2.3.2 In-line transmission method and its modification

It has been found that the fraction of light transmitted through a ceramic material without being scattered is directly related to the scattering coefficient of the ceramic medium by using the Beer-Lambert law [25]

$$T_C = {T_F}^2 \exp(-\langle\mu_s\rangle d) \tag{2.19}$$

where T_C is the in-line transmittance that can be experimentally measured using a spectrophotometer in a wide wavelength range. T_F is the Fresnel transmittance which is determined by the refractive index of the material, and d is the thickness of the ceramic sample of which parallel and flat surfaces are assumed. Consequently, the ensemble-averaged scattering coefficient $\langle\mu_s\rangle$ can be calculated.

By taking the pore size distribution r_m, σ, and the porosity P_V as variables, the calculated scattering coefficient obtained by Mie theory may provide a very close fit to the measured scattering coefficient determined by the in-line transmission measurement. The by-product of this fitting is the anisotropy factor. Besides that,

the microstructural information of the material is obtained from the best fitted pore size distribution and porosity.

In the presence of surface roughness the measured in-line transmittance may be reduced due to surface scattering. The fitting of the scattering coefficients will be affected by accounting the surface scattering as a part of the light scattering by pores. The correction can be simply done by substituting T_F in equation (2.19) by T_S in (2.18). So the in-line transmittance can be stated as

$$T_C = T_F^2 \exp\left[-\left(\frac{2\pi\delta_{rms}}{\lambda}\right)^2 (1-n)^2(1+n^2)\right] \exp(-\langle\mu_s\rangle d) \tag{2.20}$$

where the factor $(1+n^2)$ is added for an adjustment of the wavelength to the refractive index, i.e. the wavelength is λ/n inside the material.

This is a simple model by which we can evaluate the bulk scattering separately without being disturbed by the surface scattering. The obtained bulk scattering parameters are therefore more accurate and that assures the accuracy of the Monte Carlo simulations of OCT images.

2.4 Non-destructive 3D inspection of ceramics

2.4.1 Optical coherence tomography

Optical Coherence Tomography (OCT), reported for the first time in 1991 [43], has become an emerging optical cross-section imaging technique of today [44-47]. The principle will be described in detail in chapter 3. It offers a non-invasive detection possibility, and produces depth-resolved high-resolution two or three dimensional images of the back-scattering from internal microstructures in an object. In general, it is based on the low-coherence reflectometry and measures the "echoes" of backscattered light. As a tomographic imaging modality, a series of 1-D longitudinal (depth) z-scans similar to ultrasound A-scans are performed pointwise along a line in the lateral x-direction. By combining these scans for a given y-position a 2-D cross-sectional image is obtained in the X-Z plane. This is analogous to the ultrasonic pulse-echo imaging (B-scan). By further combining these cross-sectional images recorded at adjacent y-positions a full 3-D tomographic image can be obtained.

OCT was originally developed as an imaging technology in biomedicine for performing “optical biopsy”, i.e. real-time, in vivo visualization of tissue microstructures without invading the sample. Applications include tissues such as the eye, arteries, and nervous tissues [47]. Although the biomedical research has been the main driving force, new applications have appeared and in recent years the technology has spread broadly outside the biomedical field into materials investigations. A review by Stifter [48] provides a detailed overview of the OCT-based methods and applications in the fields of dimensional metrology, material research, non-destructive testing, art diagnostics, botany, microfluidics, data storage, and security applications.

Early applications of OCT in ceramics investigations were shown by Bashkansky et al., where the sizes and distributions of subsurface defects in lead zirconate titanate (PZT) and Hertzian cracks in silicon nitride ceramics were measured [49]. Other materials like single-crystal silicon carbide and Teflon-coated wires have also been investigated by these researchers [50,51]. Veilleux et al. used OCT B-scan images to evaluate the light penetration depth inside plasma-sprayed yttria-stabilized zirconia (YSZ) coatings and determined the refractive index of the material [52]. Sinescu et al. [53] evaluated the potential of en-face OCT for assessing the ceramic material defects of dental prostheses and micro-leakage at prosthetic interfaces, as well as the quality of bracket bonding on dental hard tissue. Gaps between the dental interfaces and ceramic material defects are clearly exposed in the B-scan and volumetric OCT images. Ellingson et al. [54] have used OCT for measuring the thicknesses of thermal barrier coatings (TBCs) that are usually consisting of yttria-stabilized zirconia (YSZ) and used in gas turbine engines for preventing damages to the substrate material. Moreover, in our research paper 1-4 we have shown the feasibility of OCT for detecting and measuring the embedded microchannels in alumina ceramic. In paper 5 and 6 the performances of near to mid-infrared OCT are simulated for detecting the embedded features and defects in alumina and zirconia ceramic materials. In summary, articles about applications of OCT in ceramic materials investigations are still quite few.

Dimensional metrology using low-coherence interferometry or white light interferometry, the latter mainly focused on surface profilometry, and distance ranging have been reported in several papers. However, dimensional metrology by OCT of embedded features through measurement beneath the surface of a scattering media has been scarcely reported in the literature so far. Only a few papers have

touched the field of metrology and discussing the measurement uncertainty in axial depth direction, e.g. in [55] and our paper 7. The improved accuracy of the measurement in the lateral directions has been reported in paper 8.

The major problem regarding dimensional metrology and defects detection using OCT in ceramics is the limited penetration of light due to strong scattering. The central operating wavelengths of modern commercial OCT setups are aimed for optical transparency window in biomedical tissues, whereas for industrial applications different wavelengths may be more suitable. The OCT setups working at relatively longer wavelengths, e.g. at 1.7μm [56] and 2μm [57,58] can be found only in the laboratory. Recently supercontinuum light sources, emitting from 1.75μm to 4.4μm, and high quality cooled super-lattice photon detectors, suitable for mid-IR OCT have been developed by NKT photonics [59] and IRnova [60]. The potential of a mid-IR OCT for ceramics inspection has therefore been thoroughly simulated for alumina and zirconia and the promising results are published in paper 6.

Another challenge is how to perform highly accurate quantitative measurements using OCT. The background noise caused by speckles degrades the quality of OCT images significantly [61]. Moreover, the group velocity dispersion (GVD) caused by different speeds of light at different wavelengths in a dispersive medium may degrade the axial resolution and the detection sensitivity [62,63]. The corresponding compensation methods can be found in [64,65]. Some physical [61,66-69] and digital [61,70] approaches for suppressing the speckle deterioration effects may improve the image quality, but it is usually at the expense of a loss of the axial resolution. Published methods of OCT image analysis have dealt with segmentation of intra-retinal layers, tissue structures, and nerve head [71-76], but none has so far been presented for industrial applications except for our papers 7 and 8.

Calibration of OCT system is of utmost importance for metrology applications and quantitative inspections. However, we are lacking a high quality standard artefact with calibrated dimensions dedicated for OCT and we are also lacking a standard image processing method dedicated for the dimensional metrology of embedded features in industrial samples.

The signal acquisition rate of OCT is excellent and the speed has grown from 2 A-scans per second in the original version in 1991 [43] to today's 100 Mega A-scans/s [77]. An interesting review on this issue can be found in [78]. Because of this speed advantage OCT has a great potential in the future in the roll-to-roll

manufacturing of, e.g. ceramic micro devices, printable electronics [79], and polymer solar cells [80].

Besides performing dimensional measurements various functional OCTs have been developed, including Doppler OCT [81] that measures the displacement of object or flow, polarization-sensitive OCT [82,83] that enables quantitative imaging of the birefringence properties of materials, full-field OCT [84] that produces tomographic images in the en-face orientation (perpendicular to the optical axis) using a charge-coupled device (CCD) or complementary metal-oxide-semiconductor (CMOS) camera. A 1μm resolution has been achieved for both axial and lateral directions which is comparable to that of ultrahigh resolution OCT [85]. A dedicated endoscopic OCT, [86] which uses a small-diameter (in millimeter scale) catheter that fits into the channel of standard endoscopes has been built to perform radial scanning, and a second harmonic generation (SHG) microscope combined with OCT [87] has been applied for the investigation of subsurface regions of corrosion sites formed on metals below organic coatings.

2.4.2 Other techniques

There are some other non-destructive imaging technologies available for detecting micro features and defects in ceramic materials. An obvious choice is ultrasonic testing and acoustical microscopy [88,89]. However, the need of a liquid couplant between the transducer and the ceramic is a contamination risk and may not be suitable in a roll-to-roll production process where hot sintering is performed just before the inspection is done.

X-ray transmission is another well-established technique that might work well for embedded heavy metal structures giving good contrast by X-ray absorption [90] but might be troublesome for small open cavities inside the material.

X-ray computed micro tomography (X-ray μCT) [91,92] is a very promising technique with possible resolution in the micrometer range, but at present the data acquisition time, typically hours, is by far too long to be realistic for in-process metrology. Similar to OCT, the evaluation of the accuracy of this technology is very difficult due to the complex error sources and the lack of standardization. Very few reports can be found on this topic. Kruth et al. [93] gave a survey of X-ray CT for dimensional quality control, and Carmignato [94] studied industrial X-ray CT

metrology with focus on accuracy and traceability through an international intercomparison of 15 CT systems. Papers about traceable dimensional standards for X-ray µCT can be found in [95,96]. Another problem with X-ray CT is the long exposure time needed to obtain high-quality images. The high X-ray dose may cause lattice defects in the surface and bulk of ceramic materials, which leads to colorations of the materials [97,98]. In paper 2 we compared imaging of embedded micro features in ceramic material using OCT and X-ray µCT.

Recent development of mid-IR transmission imaging techniques exploits the transparency window of zirconia from 3µm to 7µm, and allows for non-destructive optical inspection of zirconia components up to 3.5mm thick with an imaging resolution of approximately 30µm [99]. This technique is a potential screening candidate as a part of the 3D monitoring system for the roll-to-roll manufacturing technology shown in Fig. 2. It would then be used for large area coarse inspection of possible embedded defects, cracks, and delaminations in ceramic materials.

Another relatively new imaging technology that can be used for the coarse inspection in the monitoring system, and act as a good complementary tool of IR imaging is terahertz imaging. The term terahertz (THz) is related to the frequency of an electromagnetic wave usually between 0.1 and 10 THz, i.e. between microwaves and far-infrared radiation. The corresponding wavelengths range from 30µm to 3mm. Pulsed-terahertz time-domain reflectometry is an interferometric (coherent) measurement technology using the broadband nature of THz radiation [100]. The pulsed-terahertz tomography modality can be performed by scanning the sample laterally. Another option is the terahertz computed tomography (CT) technique which is inspired by X-ray CT but it has much lower radiation energy [101]. Several researchers have demonstrated the applications of terahertz imaging techniques on various ceramic materials [102-104]. The most attractive advantages are its large penetration depth and good depth resolution (10 µm may be achieved). However, the major drawback is the low lateral resolution which is limited by diffraction and is usually a few hundred micrometers or in millimeter range. Moreover, the imaging speed is relatively low, around a few hundred pixels per second [100-102].

3 Theory of optical coherence tomography

In this chapter the fundamental theory of optical coherence tomography (OCT) is described for both time- and Fourier-domain OCT. The former has not been applied in this study but it is included for pedagogical reasons, as it is more straightforward to understand. The other crucial characteristics that are mentioned here are resolution and probing depth. The aim of this chapter is to provide a basic understanding of the OCT technology and how it is possible to detect embedded features with high resolution and at high speed. More detailed descriptions of the mathematics, system configurations, and signal processing can be found in book chapters [45,47] and several review papers [44,46]. More strict derivations regarding the interference of partially coherent electromagnetic waves can be found in [105].

3.1 Theory of time-domain OCT

Time-domain OCT (TD-OCT) is the originally developed technique based on time-domain low coherence interferometry. One way to generate low coherence is to illuminate the object with an ultrashort femtosecond laser pulse, and then the backscattered light pulse from the object mixes with a fraction of the same pulse that have been split to a reference mirror in an interferometer setup. The reference pulse can be delayed a time ΔT by moving the reference mirror and thereby the position of the illuminated object can spatially sectioned by the ultrashort optical gating of the

interference envelope. This technology can provide both high resolution and a high image acquisition rate. However, it is not commonly applied today in OCT systems because of the drawbacks of the femtosecond lasers in terms of complexity, size, environmental stability, and relatively high cost [106].

The alternative method is to use a light source suitable for low coherence interferometry, e.g. a superluminescent diode (SLD) light source which is smaller, easier to use and much cheaper. Further development of SLDs may allow a higher power and larger bandwidth at different wavelength regions. A resolution comparable to that achieved using femtosecond laser can be obtained [107].

The standard OCT layout is shown in Fig. 9. The light emitted from a broadband light sources sent into the Michelson interferometer and divided into a reference beam E_{R0} and a sample beam E_{S0}.

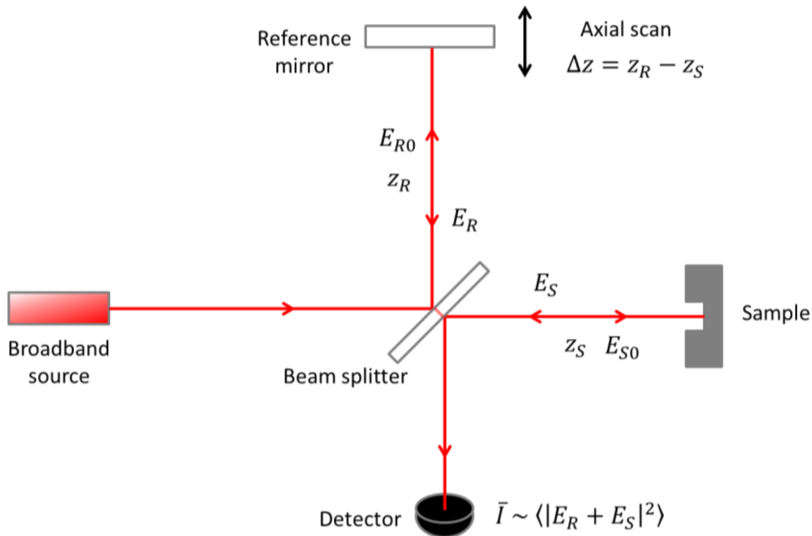

Fig. 9. Schematics of the standard time-domain OCT setup. z_R and z_S are the optical distance between the beam splitter and the reference mirror and the sample, respectively.

Assuming the beam splitter equally divides the power of the incident light, the complex electric amplitudes of the two beams after the beam splitter can be expressed respectively as

$$E_{R0} = \frac{1}{\sqrt{2}} E_0(k)\, e^{i(kz-\omega t)} \tag{3.1}$$

$$E_{S0} = \frac{1}{\sqrt{2}} E_0(k)\, e^{i(kz-\omega t)} \tag{3.2}$$

where $E_0(k)$ is the electric amplitude of the spatial frequency k of the source spectrum related to wavelength λ by $k = 2\pi/\lambda$, and the angular frequency ω is related to the frequency ν by $\omega = 2\pi\nu$. The reference beam is then reflected back from a mirror with the reflectance R_R and travels a round trip distance $2z_R$. The sample beam is backscattered from the sample with the reflectance R_S (here the sample is assumed to behave as a single reflector for simplicity) and travels a round trip distance $2z_S$. Then equation (3.1) and (3.2) become

$$E_R = \frac{1}{\sqrt{2}} E_0(k)\sqrt{R_R}\, e^{i(kz_R-\omega t)} \tag{3.3}$$

$$E_S = \frac{1}{\sqrt{2}} E_0(k)\sqrt{R_S}\, e^{i(kz_S-\omega t)} \tag{3.4}$$

The electric fields of these two beams are mixed again at the beam splitter and interference occurs. The electric power is halved again by the beam splitter and the photocurrent $\bar{I}_{TDOCT}$ generated at the detector is proportional to the total electric power

$$\bar{I}_{TDOCT} = \frac{\rho}{2}\langle |E_R + E_S|^2 \rangle = \bar{I}_{DC} + \frac{\rho}{2} \mathrm{G}(k, \Delta z) \tag{3.5}$$

where ρ is the responsivity of the detector corresponding to the efficiency of converting the photon energy to an electric current. The measured value is actually the photocurrent averaged over the response time of the detector, so the fast-varying term depending on the high frequency ω is eliminated. More details about the detectors can be found in [45,47].

The DC component of the measured current is expressed as equation (3.6) below and appears in TD-OCT as a background intensity level,

$$\bar{I}_{DC} = \frac{\rho}{2}\langle |E_R|^2 R_R \rangle + \frac{\rho}{2}\langle |E_S|^2 R_S \rangle = \frac{\rho}{4} |E_0(k)|^2 (R_R + R_S) \tag{3.6}$$

The second term on the right hand side in equation (3.5) represents the interferogram which is the desired signal. It indicates the cross-correlation between

the reference and sample beam and is a function of the optical pathlength difference $\Delta z = 2(z_R - z_S)$. When the light source is monochromatic, this term is

$$\mathrm{G}(k, \Delta z) = 2\mathrm{Re}\{\langle E_R E_S{}^{*} \rangle\} = 2\mathrm{Re}\left\{\frac{1}{2}|E_0(k)|^2\sqrt{R_R R_S}\ e^{i(k\Delta z)}\right\} \tag{3.7}$$

Now consider a broadband light source, e.g. a SLD with a Gaussian-distributed power spectral density (PSD) function $S(k) = |E_0(k)|^2$, which is centered at the spatial frequency $\mathrm{k}_0 = 2\pi/\lambda_0$, and the spectral width Δk corresponds to the half width of the spectrum at e^{-1} of its maximum. The PSD function normalized to the total spectral power S_0 is given by

$$\frac{S(k)}{S_0} = \frac{1}{\Delta k\sqrt{\pi}}\exp\left[-\left(\frac{k - \mathrm{k}_0}{\Delta k}\right)^2\right] \tag{3.8}$$

Substitute $|E_0(k)|^2$ with $S(k)$ in equation (3.7), and the interferogram G can be calculated as an integration of the interference term of each spectral component emitted by the light source,

$$\mathrm{G}(\Delta z) = S_0\sqrt{R_R R_S}\,\mathrm{Re}\left\{\int_{-\infty}^{\infty} S(k)\, e^{i(k\Delta z)}\mathrm{d}k\right\} \tag{3.9}$$

According to the Wiener-Khintchin theorem [108] the autocorrelation function is equal to the inverse Fourier transform of the power spectral density (PSD).

$$\Gamma(\Delta z) = FT^{-1}[S(k)] = \int_{-\infty}^{\infty} S(k)\, e^{i(k\Delta z)}\mathrm{d}k \tag{3.10}$$

The convenience of a Gaussian-distributed PSD function is that its inverse Fourier transform is also Gaussian. So, the autocorrelation function $\Gamma(\Delta z)$ that is also called “coherence function” is given by

$$\Gamma(\Delta z) = \exp\left[-\frac{1}{4}\Delta k^2 \Delta z^2\right]\exp(ik_0\Delta z) \tag{3.11}$$

and the real part of $\Gamma(\Delta z)$ is

$$\mathrm{Re}\{\Gamma(\Delta z)\} = \exp\left[-\frac{1}{4}\Delta k^2 \Delta z^2\right]\cos(k_0\Delta z) \tag{3.12}$$

By substituting equation (3.10) into (3.9) the interferogram G can be now calculated as

$$\mathrm{G}(\Delta z) = S_0\sqrt{R_R R_S}\ \exp\left[-\frac{1}{4}\Delta k^2 \Delta z^2\right]\cos(k_0 \Delta z) \tag{3.13}$$

The detected DC component is also re-calculated for the broadband light source by substituting $S(k) = |E_0(k)|^2$ in equation (3.6) and integrating over the whole spectrum. Considering the optical pathlength difference $\Delta z = 2(z_R - z_S)$ the detected photocurrent in equation (3.5) is now expressed as

$$\begin{aligned} \bar{I}_{TDOCT} &= \frac{\rho}{4} S_0 (R_R + R_S) \\ &+ \frac{\rho}{2} S_0 \sqrt{R_R R_S}\ e^{-\Delta k^2 (z_R - z_S)^2} \cos[2k_0 (z_R - z_S)] \end{aligned} \tag{3.14}$$

To simplify the mathematical derivation the sample is considered as a single reflector, but in reality the multilayered ceramic sample contains several reflecting surfaces and multiple backscattering sites inside the material. Consider a multi-layered sample with several reflecting interfaces where the backscattered power of the mth interface R_{Sm} is a function of its optical pathlength from the beam splitter z_{Sm}, the photocurrent is then expressed as

$$\begin{aligned} \bar{I}_{TDOCT} &= \frac{\rho}{4} S_0 \left(R_R + \sum_m R_{Sm} \right) \\ &+ \frac{\rho}{2} S_0 \sum_m \sqrt{R_R R_{Sm}}\, e^{-\Delta k^2 (z_R - z_{Sm})^2} \cos[2k_0 (z_R - z_{Sm})] \end{aligned} \tag{3.15}$$

The interference that may occur between the backscattered fields from multiple reflecting interfaces is neglected here because it is not the desired signal and can be suppressed by selecting a proper reflectance of the reference mirror [47].

So far, we now have the mathematical background of the detected signal of a TD-OCT described. In Fig. 10 a schematic setup of a fiber-optic based TD-OCT system is shown, where the beam splitter in a free-space Michelson interferometer (as shown in Fig. 9) is replaced by a 2×2 fiber coupler. The A-scan of the TD-OCT can be performed by scanning the reference mirror axially, i.e. z_R in equation (3.15) is scanned as a function of time.

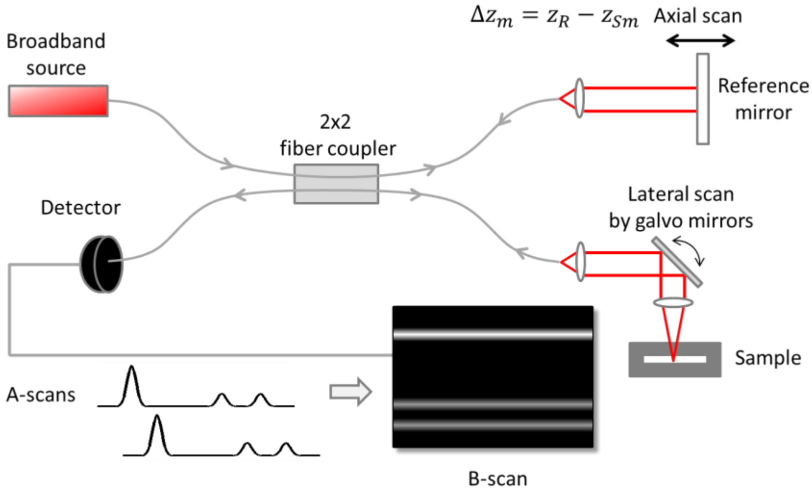

Fig. 10. Schematic setup of a fiber-optic based TD-OCT system.

The detected photocurrent is a function of the optical pathlength difference $(z_R - z_{Sm})$, which includes an envelope term $\exp[-\Delta k^2 (z_R - z_{Sm})^2]$ and a modulation carrier $\cos[2k_0(z_R - z_{Sm})]$. The effect of these is visualized in Fig. 11 which shows the photocurrent output when performing an OCT A-scan of a sample containing two reflecting interfaces. The peak powers of the envelopes depend on the backscattered power of the sample interfaces and the reference reflector, $\sqrt{R_R R_{S1}}$ and $\sqrt{R_R R_{S2}}$ located at the axial positions z_{S1} and z_{S2} respectively.

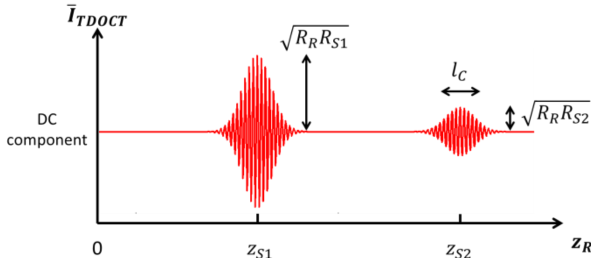

Fig. 11. A raw TD-OCT A-scan of a sample containing two reflecting interfaces, e.g the front and back surfaces of a transparent glass object with an AR-coating on the rear side. After signal processing only the envelopes of the A-scan is recorded. l_c corresponds to the width of the axial point spread function. Note that the distance between z_{S1} and z_{S2} is the optical distance involving the refractive index as a factor.

In this thesis the OCT axial resolution is determined by the axial point spread function (PSF) which depends mainly on the width of the envelope of the coherence function $\Gamma(\Delta z)$. In the OCT literature this width is characterized by the full width at half the maximum (FWHM), also called round-trip coherence length l_c which is expressed as [47]

$$l_c = \frac{2\ln(2)}{\pi}\frac{\lambda_0^2}{\Delta\lambda} \tag{3.16}$$

where λ_0 is the center wavelength of the light source and $\Delta\lambda$ is the FWHM of the wavelength spectrum.

The A-scan represented in Fig. 11 yields depth (z) information at a single x,y point. To obtain a cross-sectional B-scan the sample beam is typically scanned laterally over the sample in the x-direction direction using a galvo mirror as shown in Fig. 10. By using two galvo mirrors with rotational axes in x- and y-direction adjacent B-scans at different y-settings create a volumetric scan. Thus, the volumetric data stores a full 3D point cloud of the reflection properties inside the sample, and this can later be processed by our new 3D image processing technique presented in paper 8, and visually perceived at an outstanding image quality.

3.2 Theory of Fourier-domain OCT

In the past decade Fourier-domain OCT (FD-OCT) technology has been developed rapidly [109-115]. The most important advantage over traditional TD-OCT is that FD-OCT offers a possibility of much faster imaging speed and higher detection sensitivity. Instead of mechanically scanning a reference mirror an A-scan is obtained by a Fourier transform of the spectrally resolved interference fringes. This can be done by using a spectrometer as detector, e.g. a line array charge-coupled device (CCD). Such a system is called spectral-domain OCT (SD-OCT). It can also be done by employing a swept laser source (wavelength-tuning) with a single photodetector to record the spectrally resolved interferogram sequentially while tuning the wavelength. This is called swept-source OCT (SS-OCT). The same underlying principle is used in both methods, i.e. to reconstruct the coherence function $\Gamma(\Delta z)$ by calculating the Fourier transform of the measured power spectrum. This can be achieved by making use of the Fourier transform pair,

$$\cos(kz_0) \xleftrightarrow{FT} \frac{1}{2}[\delta(z+z_0)+\delta(z-z_0)] \tag{3.17}$$

where $\delta(z)$ is the delta function and the convolution property of Fourier transform ($\otimes$ represents convolution),

$$X(k)Y(k) \xleftrightarrow{FT} x(z) \otimes y(z) \tag{3.18}$$

Similar to equation (3.15), the detected photocurrent for FD-OCT can be expressed as [47]

$$\begin{aligned} \bar{I}_{FDOCT}(k) &= \frac{\rho}{4} S(k) \left(R_R + \sum_m R_{Sm} \right) \\ &+ \frac{\rho}{2} S(k) \sum_m \sqrt{R_R R_{Sm}} \cos[2k_0(z_R - z_{Sm})] \end{aligned} \tag{3.19}$$

where we again consider a multi-layered sample with several reflecting interfaces located at z_{Sm} $(m = 1,2,...)$ and the corresponding reflectance is the mth reflecting interface is R_{Sm}. The PSD function of the light source $S(k)$ is Gaussian-distributed, and k_0 is the mean wavenumber. Different from TD-OCT which detects the interferometric signals of all spectral components simultaneously, the detected photocurrent $\bar{I}_{FDOCT}(k)$ is recorded over the spatial frequency k of each spectral component sequentially or by a spectrometer. In order to obtain the desired spatial distribution of the multiple reflecting interfaces, the inverse Fourier transform of $\bar{I}_{FDOCT}$ is taken, and $i_d = FT^{-1}(\bar{I}_{FDOCT})$ is expressed as

$$\begin{aligned} i_d &= \frac{\rho}{4} FT^{-1}[S(k)] \left(R_R + \sum_m R_{Sm} \right) \\ &+ \frac{\rho}{2} FT^{-1} \left\{ S(k) \sum_m \sqrt{R_R R_{Sm}} \cos[2k_0(z_R - z_{Sm})] \right\} \end{aligned} \tag{3.20}$$

From equation (3.10) we know that the coherence function is equal to the inverse Fourier transform of the PSD function, $\Gamma(\Delta z) = FT^{-1}[S(k)]$. By using the properties of Fourier transform in (3.17) and (3.18), equation (3.20) can be written as

$$i_d = \frac{\rho}{4}\Gamma(\Delta z)\left(R_R + \sum_m R_{Sm}\right)$$
$$+\frac{\rho}{2}\Gamma(\Delta z) \otimes \sum_m \sqrt{R_R R_{Sm}}\{\delta[\Delta z + 2(z_R - z_{Sm})] + \delta[\Delta z - 2(z_R - z_{Sm})]\} \tag{3.21}$$

where Δz is the variable which means the round-trip optical pathlength difference between the reference and sample beam. According to the so-called sifting property of a delta function [116], the convolution between a function $f(z)$ and a delta function $\delta(z \pm z_0)$ is equal to $f(z + z_0)$. Hence, equation (3.21) can be calculated as

$$i_d = \frac{\rho}{4}\Gamma(\Delta z)\left(R_R + \sum_m R_{Sm}\right)$$
$$+\frac{\rho}{4}\sum_m \sqrt{R_R R_{Sm}}\{\Gamma[\Delta z + \Delta z_m] + \Gamma[\Delta z - \Delta z_m]\} \tag{3.22}$$

where the first term in the equation is the DC component centered at the optical pathlength z_R, i.e. at $\Delta z = 0$ as shown in Fig. 12. This differs from TD-OCT where the DC component is a constant offset signal for the whole axial scanning range (as shown in Fig. 11). Moreover, $\Delta z_m = 2(z_R - z_{Sm})$ is the optical pathlength difference between the reference beam and the sample beam that is reflected back from the mth reflecting interface. With a fixed reference arm this term is determined by z_{Sm}.

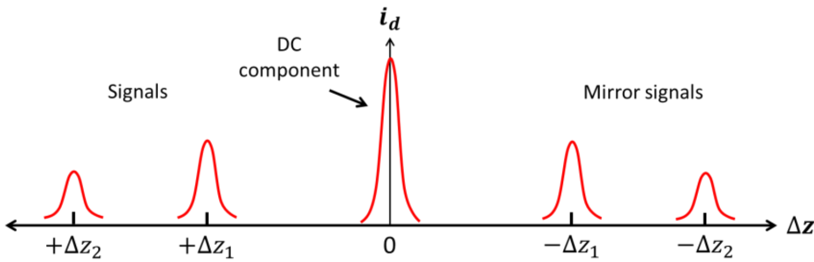

Fig. 12. An example of FD-OCT A-scan of a sample containing two reflecting interfaces. The strong DC component is centered at $\Delta z = 0$, and the signals of the sample interfaces and the mirror signals are symmetric about the DC component.

From equation (3.22) we see that two Γ functions exist with $\Delta z + \Delta z_m$ and $\Delta z - \Delta z_m$. This means that two signals located at $\pm\Delta z_m$ and mirrored about the center position $\Delta z = 0$ will appear. With two interfaces in the measured sample, located at z_{S1} and z_{S2} and having reflectances R_{S1} and R_{S2}, we get the A-scan response as demonstrated in Fig. 12, i.e. "false" mirror images will show up. To have the mirror images separated from the real images the optical pathlength to the first surface of the sample has to be larger than the optical pathlength to the reference mirror, i.e. $z_{S1} > z_R$. Otherwise, if $z_{S1} < z_R < z_{S2}$ the mirrored images will overlap around the DC component at z_R.

Therefore, only the images on one side of the DC component can be used and displayed. Moreover, the distance between the two reflecting interfaces in the image field is $\Delta z_1 - \Delta z_2 = 2(z_{S2} - z_{S1})$, i.e. double of the optical distance in reality.

The DC component and the signals of the sample interfaces in Fig. 12 are blurred by an axial point spread function (PSF), which in turn is dependent on the coherence function $\Gamma(\Delta z)$ determined by the power spectrum $\mathrm{S}(k)$ of the incident radiation. For an FD-OCT system with a small NA objective lens, the the axial resolution is determined by the axial PSF, i.e. the same as that of TD-OCT in (3.16).

To sum up the advantages of FD-OCT we see that it offers a much higher imaging speed compared to TD-OCT due to the fixed reference arm and the fact that the entire depth of the sample is recorded simultaneously. Another pronounced advantage is the improvement of detection sensitivity that is defined as the ratio of the signal powers in dB generated by a perfectly reflecting mirror and the minimum detectable reflected power. The major reason is simply the increased power of the incident radiation because theoretically the maximum allowable power of each spectral component in FD-OCT is equal to the total spectral power in TD-OCT. Even though half of the spectral power is wasted because of the mirror signals as shown in Fig. 12, an improvement of sensitivity up to 20dB may be expected for FD-OCT [109-111].

So far the fundamental theory of FD-OCT has been introduced. In the following subsections two types of FD-OCT, the spectral domain OCT and the swept-source OCT, will be described, particularly regarding their differences.

3.2.1 Spectral domain OCT

A schematic illustration of a spectral domain OCT (SD-OCT) is shown in Fig. 13. A broadband radiation source similar to that of TD-OCT is typically used. What is different is that the reference path remains fixed without scanning in the SD-OCT. At the exit of the interferometer a diffraction grating can be used for dispersing the different spectral components over a line array CCD camera by which the interferometric power is then obtained [46]. The pixel resolution of the camera determines the digitization of the continuous spectrum of the dispersed radiation, i.e. the spectral sampling interval. The detection sensitivity in SD-OCT is also correlated to the number of pixels [47].

The detected signal $\bar{I}_{FDOCT}$ has already been expressed in equation (3.19). By taking the inverse Fourier transform of the measured spectrally resolved interferometric signal, the depth information is obtained as an axial distribution function of the local reflectivities from features and interfaces of the sample.

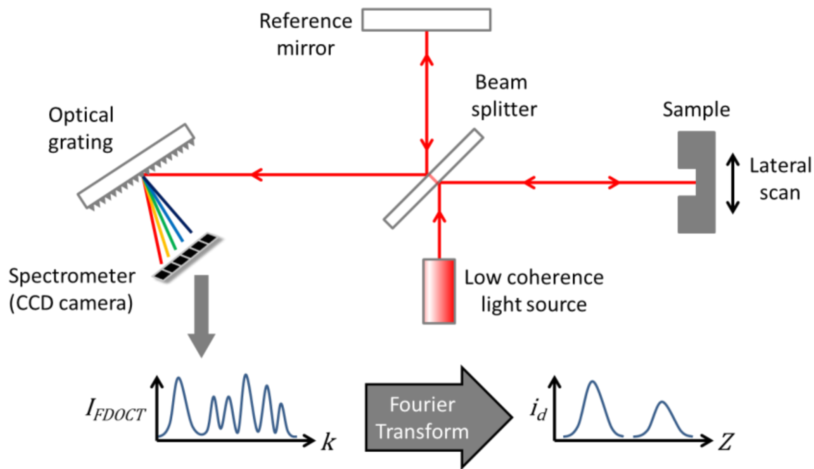

Fig. 13. Schematic setup of a spectral domain OCT (SD-OCT).

The lateral scanning over the sample is carried out in the same way as that in TD-OCT, for instance by using two galvo mirrors with rotational axes in x- and y-direction. Multiple A-scans recorded at adjacent lateral positions are assembled into a B-scan, and in the same way volumetric data are obtained by recording multiple adjacent B-scans.

3.2.2 Swept-source OCT

The other Fourier domain approach is the swept-source OCT (SS-OCT), also called optical frequency-domain imaging/reflectometry [112,113]. The schematic setup of a SS-OCT is shown in Fig. 14, where the reference path and sample path remain constant.

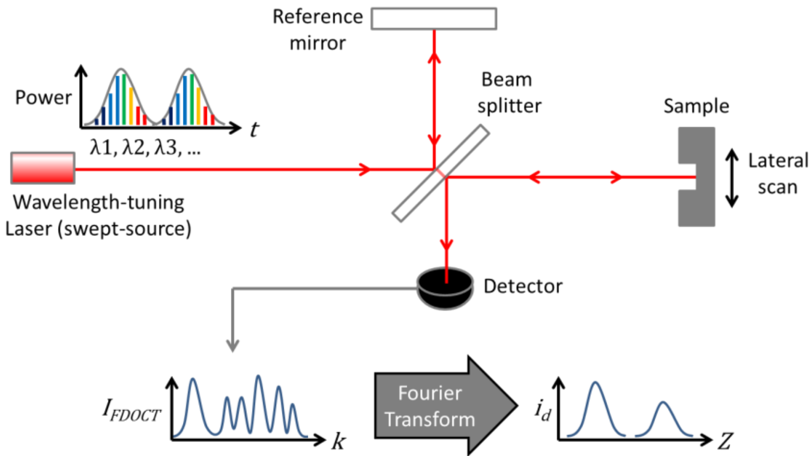

Fig. 14. Schematic setup of a swept-source OCT (SS-OCT).

The major differences between SS-OCT and SD-OCT are the radiation sources and detectors. Instead of using a spectrometer and line array CCD camera to detect the spectrally resolved interferogram, the SS-OCT uses a wavelength-swept (wavelength-tuning) laser as source. This source irradiates the sample with a single wavelength at a time, and a single photodetector is used to record the interferogram. When the wavelength of the laser source is swept rapidly the detected photocurrent $\bar{I}_{FDOCT}$ in Eq. (3.19) is recorded sequentially for each wavenumber k. Again, by taking the inverse Fourier transform of $\bar{I}_{FDOCT}$ the depth information of the sample is obtained, and by scanning the sample beam laterally the OCT B-scan is captured. A typical radiation source spectrum of SS-OCT is illustrated in Fig. 15. The sampling wavelength interval that works similarly to the pixel resolution in SD-OCT should be smaller than the instantaneous laser linewidth [47,114]. The latter is inversely proportional to the detection sensitivity and the coherence length which will be discussed in the next section. Assuming the overall tuning spectrum in Fig. 15 is

Gaussian then the axial resolution of SS-OCT has the same expression as that of TD-OCT stated in equation (3.16).

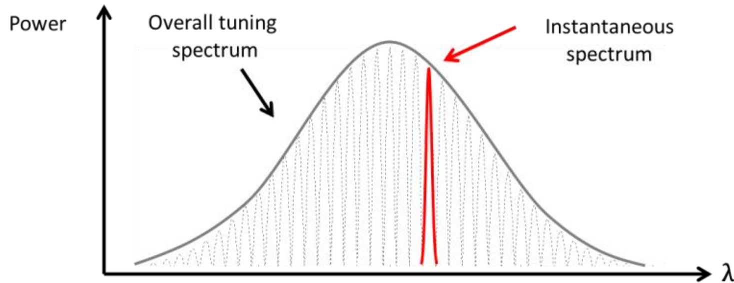

Fig. 15. Schematic illustration of the swept-source spectrum of SS-OCT.

3.3 Probing depth

Probing depth is one of the most important metrics in the evaluation of OCT systems for inspecting industrial ceramic samples with embedded features. It determines how deep a feature within a sample can be and still be detected by the OCT technique. However, there is a lack of strict definition here, since the probing depth can be limited due to different reasons. The first effect influencing the probing depth is related to geometrical optics and is usually referred to as the depth of view (DOV) and it depends on NA of the objective lens as [47]

$$DOV \approx \frac{0.565\,\lambda}{\sin^2\left[\frac{\sin^{-1}(\mathrm{NA})}{2}\right]} \tag{3.23}$$

By choosing an objective lens with smaller NA the DOV can be increased at the expense of lateral resolution.

In SD-OCT the sensitivity decreases with the imaging depth due to the finite spectrometer spectral resolution. This may limit the probing depth to a few millimeters [111,115].

In SS-OCT, the probing depth is limited by the finite laser coherence length, which is determined by the instantaneous laser linewidth. This can be improved by employing a MEMS tunable vertical cavity surface emitting laser (MEMS-VCSELs) [55]. A probing depth in the centimeters range can be achieved while still maintaining a reasonable lateral resolution.

The sensitivity falloff and the finite laser coherence length may be the limiting factor for DOV in transparent or semitransparent samples but not for highly-scattering ceramic materials.

3.3.1 Scatter-limited probing depth

In this thesis the probing depth is mainly limited by scattering of the incident and back-reflected beam. Thus, the weakest signal backscattered from an embedded feature can be detected at depths of around a few hundred micrometers only. For an FD-OCT the probing depth may be improved by increasing the photon flux, e.g. by increasing the power of the incident radiation. It is currently restricted in the OCT-systems because of their adaption to biomedical samples. The signal acquisition time can be extended at the expense of a reduced imaging speed, and by increasing the finite spectrometer spectral resolution in an SD-OCT or the laser instantaneous linewidth in SS-OCT, deeper probing depths can be achieved.

Another option for improving the probing depth is to make the ceramic samples more transparent. The materials cannot be changed so much because they are optimized for or limited by the applications and the manufacturing processes. However, it may be possible to find an optimal wavelength region for reducing the scattering while keeping the light absorption low as well. The potential wavelength regions may be predicted by evaluating the transparency of the material using spectrophotometry. If sufficient optical power can reach the embedded features and be reflected to the detector the probing depth is likely to be improved.

3.3.2 Potential of mid-IR OCT

Since OCT was originally developed for biomedical applications, and still is the main driving force of the technique, the operating wavelengths are fitted for that purpose. For example, most light sources including SLDs and broadband lasers are developed for the wavelength regions centered at 800 nm, 1300 nm and 1550 nm, where well-established and inexpensive methods can be picked up from optical communication technologies. Bio-tissues contain a large content of water by which the light absorption increases for wavelengths longer than 900 nm and becomes dominant for wavelengths approaching 1900 nm [117]. For balancing the

detrimental effects of light scattering and absorption operation of OCT at $\lambda = 1300$ nm has become a standard for most OCT applications, particularly in the biomedical field.

However, these wavelength regions are not optimal for the industrial ceramic samples. For example, a transparency window exists for the alumina and zirconia ceramic materials at $\lambda = 4\sim6$ µm (which will be shown in section 7.1), and the absorption of light can be neglected in the wavelength region of $\lambda = 0.5\sim4$ µm [paper 3]. Therefore, an optimal OCT system for such materials can be expected to be operating at wavelengths around $\lambda = 4$ µm, for balancing scattering and absorption.

OCT systems working at center wavelengths of $\lambda = 1.7$ µm and 2 µm are already used in laboratories [56-58]. For longer wavelengths, the mid-IR supercontinuum source based on mode-locked picosecond fiber lasers, may be a good candidate. It can generate a spectrum over a range from $\lambda = 1.75\sim4.4$ µm. [59]. Correspondingly, a suitable cooled IR detector can be made by the so-called type II super lattice technology [60], which offers a cut-off wavelength ranging from 2 µm to 30 µm. In paper 6 we elaborate a bit more about these ideas and predict the performance by simulations.

4 Monte Carlo simulation of OCT images

4.1 Introduction

The Monte Carlo method differs from other numerical methods using random sampling to solve a physical or mathematical problem. In the method a stochastic model is established in which the desired physical quantity is equivalent to the expected value of a random variable. This value is estimated by sampling the probability distribution of the random variable. The Monte Carlo method has become a useful computational tool in many scientific areas, including the simulation of photon and neutron transport [118,119], modeling of laser tissue interactions [120] and light propagation in multi-layered tissue [121,122]. The method also supports complex geometrical models and boundary conditions and has therefore been successfully applied to simulate OCT signals and images of multi-layered tissue and paper [123-127], as well as ceramic structures (see papers 3, 5, and 6).

4.2 Basic principle of the Monte Carlo method

In this section the basic principle of the Monte Carlo method will be described in the context of photon transport in a scattering medium (absorption is neglected). One of the random variables to be sampled is the free pathlength which is the distance a photon travels between two successive scattering events. Another is the angle through which the photon is scattered, i.e. the angular deviation from its original

direction. We know that when a photon travels in the medium the probability density function of the photon free pathlength is exponentially distributed [118], and the probability that the photon is scattered through some angle is given by another probability density function, called the phase function. The problem is how to make the random sampling of the variables from probability distributions that are non-uniform.

4.2.1 Sampling of the photon free pathlength

Consider a random number ξ which is uniformly distributed in the interval [0,1). Then, the cumulative distribution function can be expressed as $F_{\Xi}(\xi) = \xi$ and it is plotted in Fig. 16(A). This distribution shows that the probability of hitting a random number less than or equal to a value ξ is equal to ξ itself. Let $p_L(x)$ be the probability density function of the photon free pathlength on the interval $[0,\infty)$, and let the cumulative distribution function be $P_L(l)$ where l is a random variable and the function has a value range [0,1). As shown in Fig. 16, by equating the random number ξ with the cumulative distribution function $P_L(l)$ which has the same range [0,1), we can state the fundamental principle of the Monte Carlo method as [118]

$$\xi = P_L(l) = \int_0^l p_L(x)\mathrm{d}x \tag{4.1}$$

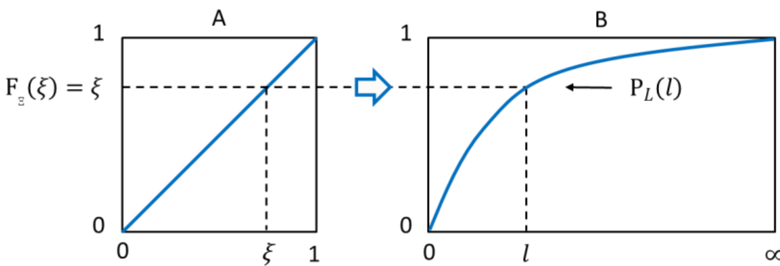

Fig. 16. Schematic illustration of the principle of the Monte Carlo method. The cumulative distribution functions of the random number ξ and the random variable l are plotted in (A) and (B), respectively.

Let us now consider the photon transport in a scattering medium, where the probability density function of the photon free pathlength follows the Beer-Lambert law [118]

$$\mathrm{p}_L(l) = \mu_s \exp(-\mu_s l) \quad (4.2)$$

where the scattering coefficient μ_s implies the mean probability per unit length of a scattering, and is equivalent to the reciprocal of the mean free pathlength $1/\langle l \rangle$. From equation (4.1) we have

$$\xi = \int_0^l \mu_s \exp(-\mu_s x) \mathrm{d}x = 1 - \exp(-\mu_s l) \quad (4.3)$$

Therefore, the photon free pathlength can be stated as a function of the random number

$$l = -\frac{1}{\mu_s} \ln(1 - \xi) \quad (4.4)$$

Since $(1 - \xi)$ has the same distribution as ξ and may be replaced by ξ, the expression of the photon free pathlength is obtained as

$$l = -\frac{1}{\mu_s} \ln \xi \quad (4.5)$$

4.2.2 Sampling of the scattering angles

The other random variables to be sampled are the scattering angles which can be described by the azimuthal angle ϕ and the polar angle θ as shown in Fig. 17.

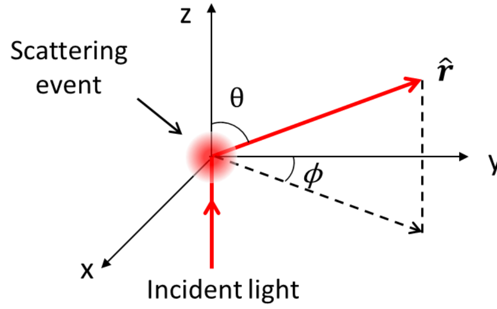

Fig. 17. Scattered light in the direction $\hat{r}$ with the azimuthal angle ϕ and the polar angle θ.

The azimuthal angle ϕ is uniformly distributed in [0, 2π), and can be sampled by generating the random numbers ξ_1 that are uniformly distributed in [0, 1)

$$\phi = 2\pi \cdot \xi_1 \tag{4.6}$$

The probability density of the polar angle θ is governed by the phase function, and in this thesis the Henyey-Greenstein phase function [128] is used to approximate the angular dependence of the scattering in ceramic materials. It is expressed as

$$\mathrm{p}_{HG}(\theta) = \frac{1}{4\pi}\frac{1-g^2}{[1+g^2-2g\cdot\cos\theta]^{3/2}} \tag{4.7}$$

where the anisotropy factor g equals the average cosine of the polar angle $\langle\cos\theta\rangle$ and varies in the interval [−1,+1]. Recall equation (2.3) and state it as

$$\int_0^{2\pi}\left\{\int_0^{\pi}\mathrm{p}(\theta)\mathrm{d}\sin\theta\,\mathrm{d}\theta\right\}\mathrm{d}\phi = 1 \tag{4.8}$$

and we know $\int_0^{2\pi}\mathrm{d}\phi = 2\pi$, then $2\pi\cdot\mathrm{p}_{HG}(\cos\theta)$ is the probability density function of $\cos\theta$. Hence (4.7) can be written as

$$\mathrm{p}_{HG}(\cos\theta) = \frac{1}{2}\frac{1-g^2}{[1+g^2-2g\cos\theta]^{3/2}} \tag{4.9}$$

As shown in Fig. 18 the g value is positive if forward scattering dominates and $g = 0$ represents symmetric scattering.

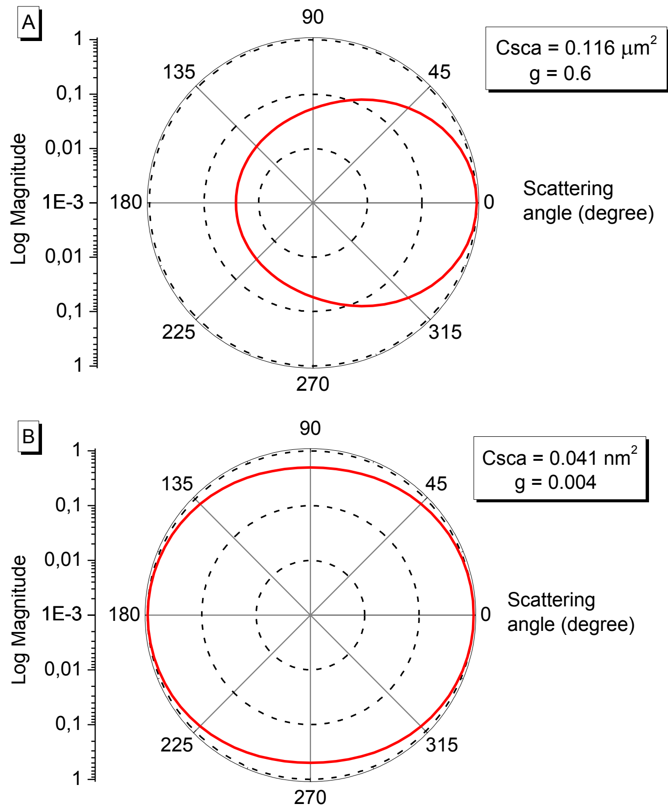

Fig. 18. Logarithm-scale polar graph of the simulated scattering pattern. Unpolarized light is incident from the left side on a single scattering point located in the origo of the graphs. A) particle diameter is 0.4μm, $g = 0.6$, forward scattering dominates; B) particle diameter is 0.01μm, $g \approx 0$, symmetric scattering. Note that the magnitude is normalized so that the peak value is unity in both graphs, but the scattering cross section C_{sca} is much larger in (A).

Recall the fundamental principle of the Monte Carlo method in eq. (4.1), and we have

$$\xi_2 = \mathrm{P}_{HG}(\cos\theta) = \int_0^{\cos\theta} \mathrm{p}_{HG}(\eta)\mathrm{d}\eta \tag{4.10}$$

where ξ_2 is uniformly distributed in [0, 1), and then

$$\cos\theta = \frac{1}{2g}\left[1 + g^2 - \left(\frac{1-g^2}{[1-g+2g\cdot\xi_2]}\right)^2\right] \tag{4.11}$$

If $g = 0$, i.e. isotropic scattering

$$\cos\theta = 2\xi_2 - 1 \tag{4.12}$$

4.2.3 Geometrical treatment of photon transport

After the free pathlength and the scattering angles are obtained the photon travelling path can be described in fixed global Cartesian coordinates. As demonstrated in Fig. 19 the current photon direction, $\hat{r}$ (^ denotes a vector), can be specified by the direction cosines (u, v, w) with respect to the x, y, and z axes, respectively.

$$[u \quad v \quad w] = \frac{\hat{r}}{|\hat{r}|}\cdot\begin{bmatrix}\hat{e}_x\\ \hat{e}_y\\ \hat{e}_z\end{bmatrix} \tag{4.13}$$

where $\hat{e}_x$, $\hat{e}_y$, $\hat{e}_z$ are unit vectors for each axis. The current position of the photon after travelling a pathlength l is

$$\begin{aligned} x &= x_0 + u\cdot l\\ y &= y_0 + v\cdot l\\ z &= z_0 + w\cdot l \end{aligned} \tag{4.14}$$

where (x_0, y_0, z_0) was the old position.

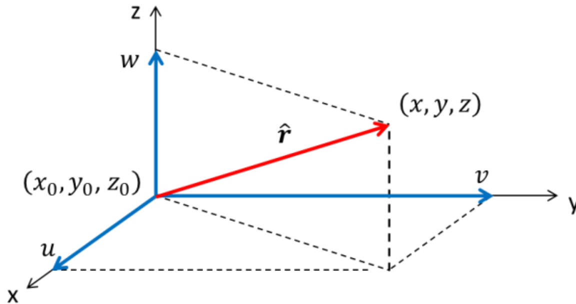

Fig. 19. The current photon direction $\hat{r}$ and its direction cosines (u, v, w) with respect to the x, y, and z axes, respectively.

Let us consider a scattering event in a local Cartesian coordinate system as shown in Fig. 20. The scattering occurs at the current position (x, y, z) and the photon is scattered at a polar angle θ and an azimuthal angle ϕ relative to the incident direction $\hat{r}$. The z-axis of the local coordinate system which is denoted as $\hat{n}_z$ is in the same direction as $\hat{r}$. Its x-axis denoted as $\hat{n}_x$ is perpendicular to $\hat{n}_z$ and is included in the incident plane, i.e. the plane given by the global z-axis and $\hat{n}_z$. The y-axis is then perpendicular to $\hat{n}_z$ and $\hat{n}_x$ and denoted as $\hat{n}_y$.

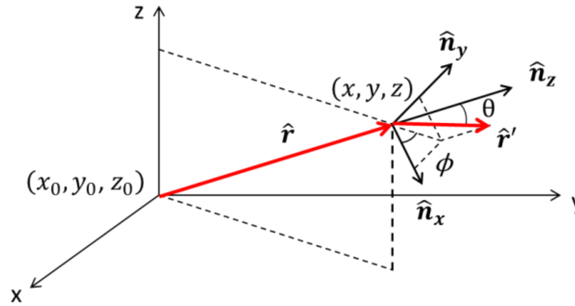

Fig. 20. The new photon direction $\hat{r}'$ and the local coordinate system $\hat{n}_x$, $\hat{n}_y$, and $\hat{n}_z$ with the origin at position (x, y, z). The photon is scattered at a polar angle θ and an azimuthal angle ϕ.

The new photon direction, $\hat{r}'$, can be specified by the direction cosines (u', v', w') with respect to local coordinate system $\hat{n}_x$, $\hat{n}_y$, and $\hat{n}_z$ as

$$[u' \quad v' \quad w'] = \frac{\hat{r}'}{|\hat{r}'|} \cdot \begin{bmatrix} \hat{n}_x \\ \hat{n}_y \\ \hat{n}_z \end{bmatrix} \tag{4.15}$$

which can be then expressed as

$$[u' \quad v' \quad w'] = [\sin\theta\cos\phi \quad \sin\theta\sin\phi \quad \cos\theta] \cdot \begin{bmatrix} \hat{n}_x \\ \hat{n}_y \\ \hat{n}_z \end{bmatrix} \tag{4.16}$$

In order to calculate the new position of the photon in the fixed global coordinate system, we need to express $\hat{n}_x$, $\hat{n}_y$, and $\hat{n}_z$ with the unit vector $\hat{e}_x$, $\hat{e}_y$, $\hat{e}_z$ as

$$\begin{bmatrix} \hat{n}_x \\ \hat{n}_y \\ \hat{n}_z \end{bmatrix} = \begin{bmatrix} \frac{uw}{\sqrt{1-w^2}}\hat{e}_x & \frac{vw}{\sqrt{1-w^2}}\hat{e}_y & -\sqrt{1-w^2}\,\hat{e}_z \\ \frac{-v}{\sqrt{1-w^2}}\hat{e}_x & \frac{u}{\sqrt{1-w^2}}\hat{e}_y & 0 \\ u\cdot\hat{e}_x & v\cdot\hat{e}_y & w\cdot\hat{e}_z \end{bmatrix} \tag{4.17}$$

By substituting (4.17) into (4.16), the new direction cosines (u', v', w') are obtained as

$$\begin{aligned} u' =&\quad \frac{\sin\theta}{\sqrt{1-w^2}}(uw\cos\phi - v\sin\phi) + u\cos\theta \\ v' =&\quad \frac{\sin\theta}{\sqrt{1-w^2}}(vw\cos\phi + u\sin\phi) + v\cos\theta \\ w' =&\quad -\sin\theta\cos\phi\sqrt{1-w^2} + w\cos\theta \end{aligned} \tag{4.18}$$

If the incident direction $\hat{r}$ is very close to the normal (e.g. when $|w| > 0.99999$ [120]), the new direction (u', v', w') is calculated as

$$\begin{aligned} u' =&\quad \sin\theta\cos\phi \\ v' =&\quad \sin\theta\sin\phi \\ w' =&\quad \frac{w}{|w|}\cos\theta \end{aligned} \tag{4.19}$$

With the updated photon direction, the new photon position is then calculated as

$$\begin{aligned} x' &= x + u'\cdot l \\ y' &= y + v'\cdot l \\ z' &= z + w'\cdot l \end{aligned} \tag{4.20}$$

4.3 Monte Carlo simulation of OCT images

The Monte Carlo ray-tracing program used our simulations has been developed and tested in previous studies [126,127]. In our case it simulates the transport of numerous random trajectories of photons propagating in alumina and zirconia samples where severe light scattering happens. The photon packet is launched and incident onto the surface and interior of the sample which is described by a complex geometric model with certain boundary conditions. Then, the trajectory of a photon is calculated by the Monte Carlo method as described in the previous section and will be recorded if it fits the OCT detection conditions, otherwise it will be

terminated, as shown in Fig. 21. The statistical distribution of the detected photons over their traversed optical pathlengths is obtained as an OCT A-scan. By repeating this process in a consecutive step-wise fashion and compiling all the A-scans side by side, an OCT B-scan is obtained, and we get an OCT "image".

The detector size and the detection angle mimic the NA of the imaging optics of an experimental OCT setup. For small numerical apertures (NA<0.1) of the detector, several millions photons needs to be launched for each A-scan to provide a good SNR and yield a good "image" quality.

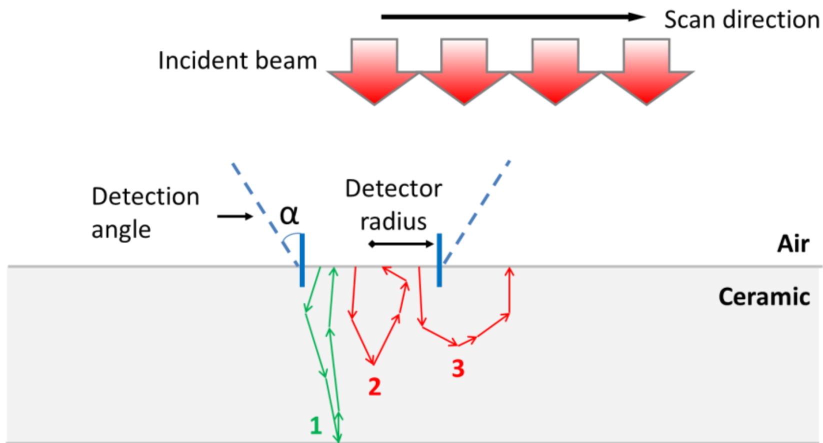

Fig. 21. Schematic illustration of the Monte Carlo simulation of OCT image. The photon trajectories are simulated and only photon 1 is recorded, whereas the photon 2 and 3 are terminated because the former exits the material with a polar angle larger than the detection angle and the latter exits the material outside of the detector area.

5 Processing of OCT images

As already presented, the depth data captured by OCT can be presented as A, B, and volumetric scans, just as in ultrasonic imaging. Another resemblance with ultrasonic cross sectional images is the often lousy quality of the images, with SNR levels approaching 1 caused by speckle formation. Our goal of developing in-material-metrology based on OCT therefore requires an improved data handling technique. In this chapter we present the background to our greatest achievements in this area by introducing a fast and accurate 3D image processing method for volumetric OCT data. The technical details can be found in paper 7 and 8 but many of the pictures are shown here to explain the principle. The purpose of processing OCT images is to develop a fast, automated and accurate method dedicated for the dimensional metrology of the embedded features in ceramic materials. These features, faintly appearing in the raw OCT images, are usually presented to the human perceptual system as 3D images in a certain color format as devised by standard rendering and display methods in medical image processing [129]. The desired information we are aiming for, like the boundaries of ceramic layers and structures, may be extracted from OCT images manually by experienced operators. However, this is an extremely time-consuming process when handling a large amount of volumetric data. Also, the measurement accuracy can vary considerably from one operator to another. Moreover, due to the very low local signal-to-noise ratio (SNR) present in OCT images of high scattering ceramic samples, it is almost impossible to use standard image processing methods to extract and segment the boundaries. We have therefore developed two dedicated image processing algorithms. One “Ridge

detection" package for 2D cross-sectional OCT B-scans and one "3D correlation detection" package for 3D volumetric OCT image.

5.1 Ridge detection algorithm

5.1.1 Concept

A typical OCT B-scan of a ceramic sample with embedded interfaces is shown in Fig. 22. Basically the image processing is a segmentation problem, but the standard methods [130] fail because of the strong scattering, appearing as a grainy structure, degrading the SNR severely. It is caused by speckles resulting from the parly coherent radiation and chops the desired boundaries into pixelated images with high intensity variations, as shown in the enlarged picture of Fig. 22. The speckles can hardly be removed or suppressed, since they are both noise and information carriers [61].

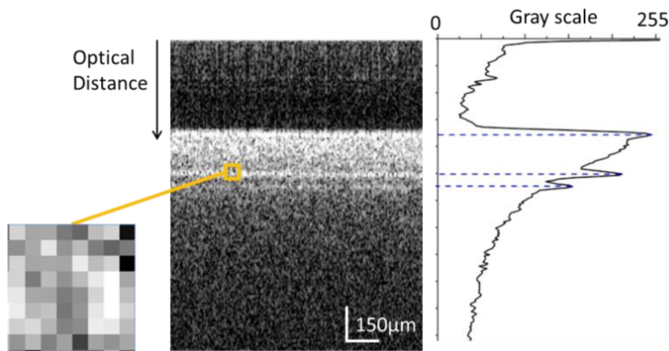

Fig. 22. Example of a cross-sectional OCT B-scan of a multi-layered ceramic sample containing embedded interfaces. The enlarged pixel image of the boundary is shown on the left side and the corresponding average A-scan signal is shown on the right hand side. (This figure is extracted from paper 7)

The peaks appearing in the A-scan profile in Fig. 22 represent the geometric boundaries of the layered ceramic stack, which is of utmost interest for dimensional metrology and we will use the word "ridge" to represent these brighter bands in the images of these boundaries in this thesis. The signals generated by local small scattering sites in the ceramic materials will be treated as noise.

The concept of the ridge detection has its root in measuring the so-called Mura in images of display masks, which is caused by extremely small systematic placement errors of pixels on the mask [131]. In a visual inspection of the mask these artifacts are seen as weak contrast changes in lines or bands across the mask. In an image of the mask it is almost impossible to measure these placement errors due to the fact that the error is of the same magnitude or smaller than the random noise.

In an OCT image it is easy for an experienced observer to see features in the image owing to the human brain preferences for filling in lacking information. However, to teach a computer to recognize and measure these interrupted or noisy features is a real challenge. Based on the material characteristics and geometry of the features, we made a major assumption that the images of physical boundaries are longer than the "drop outs" caused by speckles and discrete small scatter centers.

The Ridge detection algorithm is summarized in three steps in Fig. 23, where the labels A-C correspond to the images in Fig. 24. First we extract local intensity maxima from the original OCT image, followed by extracting the longer segments using the assumption of a continuous surface. A template of the extracted image is built where the ridges are marked as ones (bright pixels) in a logical image. In the final step a sub-pixel resolution refinement is applied to the original OCT image based on the locations of the ridges.

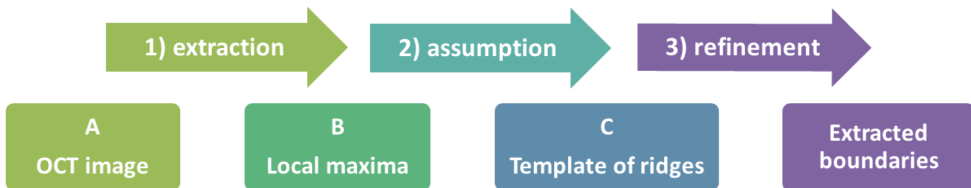

Fig. 23. Steps of the new OCT boundary detection algorithm.

5.1.2 Candidate ridge detection

As a demonstration of the method, Fig. 24 shows the images that represent the steps for generating a logical template of the ridges. The input is a gray-scale OCT B-scan of the ceramic layer, in this case with laser-milled microchannels, and captured as the imaging cross section schematically illustrated in the top left picture. The first step is then to extract the long ridges in any direction from the image. To obtain that,

we first estimate the local maximum and store it as a candidate ridge pixel if certain conditions are fulfilled (see paper 7).

The logical connection map in Fig. 24B is formed as a linear combination of the candidate ridge pixels found in all directions. By using the connection map we can now merge horizontal and vertical ridges using some simple logic. A horizontal and vertical ridge can only be merged together in a connection point. The final logical template of ridges in Fig. 24C is generated after a merging and cleaning process by the assumption of a continuous surface. The details of the above processes can be found in paper 7.

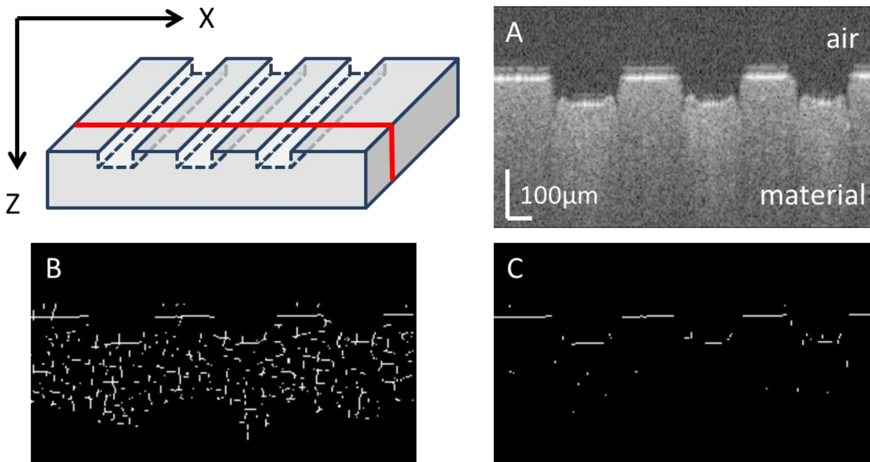

Fig. 24. Images describing the different steps in the ridge detection algorithm. (A) Input OCT image, (B) The logical connection map which contains the results after extracting longest ridges in all directions, (C) Final logical template of ridges after a merging and cleaning process. The vertical bar in (A) represents a 100 µm optical distance.

5.1.3 Sub-pixel refinement algorithm

The template presented in Fig. 24C provides the locations of the candidate ridge pixels. We now use a closer neighborhood around each candidate pixel in order to find where the ridge is located at sub-pixel resolution. The smallest neighborhood that can be used is the eight pixels that surround the candidate pixel at location. As shown in Fig. 25, the gradients of these pixels are calculated as eight vectors

pointing towards the locations of the local maxima. The neighbor pixels' "opinions" of the locations of the maxima are marked with red dots which must be inside the white circle to be accepted. The red cross hair that is calculated by averaging the red dots is the sub-pixel location of the maximum at the location marked with the white square. The detailed mathematical descriptions can be found in paper 7.

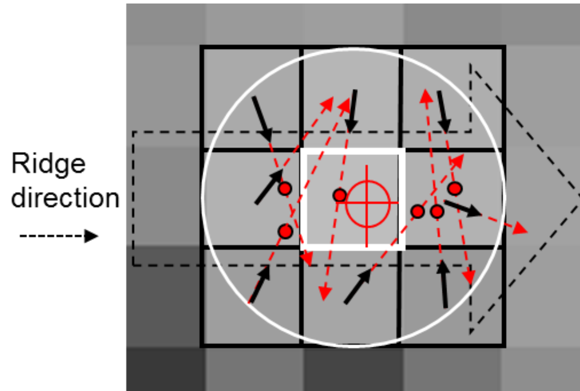

Fig. 25. The eight pixel neighborhoods of a ridge pixel (marked with a white square) belonging to a ridge in X-direction. The black arrows are the gradients vectors originating at the centers of these eight pixels and pointing towards the locations of the local maxima which are marked with red dots. The red cross hair that is calculated as the center of gravity of the red dots is the final sub-pixel location of the ridge pixel at this location.

In this way we build a chain of pixels describing the ridge with sub-pixel precision as shown in Fig. 26, where the logical template in Fig. 24C is used.

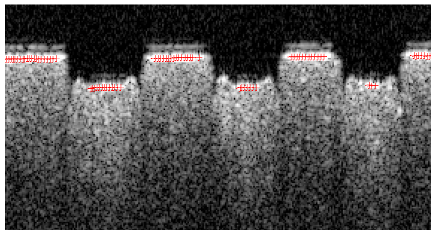

Fig. 26. The result of the sub-pixel refinement of each pixel in the template in Fig. 24C. A few false ridges left in the template will not be accepted in the refinement. The contrast of the image is enhanced for display, where the gray scale corresponds to a dynamic range of 45 dB. However, the image processing is done on the original OCT data which has a dynamic range of 110 dB.

An important feature of this algorithm is its ability to find the true boundary of reflection maxima with sub-pixel precision. Furthermore it can remove pixels that are not real local maxima in the eight pixel neighborhood but have been found in a larger area about the pixel location by the candidate ridge detection. The final result is generated from the original OCT image without loss of information.

5.2 3D correlation detection algorithm

One of the significant features of OCT is its capability of rapid three-dimensional (3D) imaging of embedded structures of the investigated samples. In the industry of ceramic micromanufacturing this means a possibility of 3D monitoring of the manufacturing processes and the product quality. In order to fully make use of the information embedded in the volumetric OCT data, the image processing must be extended to 3D.

5.2.1 Concept

As previously explained, a volumetric OCT image is generated from a large number of adjacent A-scans by scanning the probing beam across the sample laterally in the X- and Y-directions. The original A-scans contain the dimensional information in axial Z-direction, based on the principle of low-coherence interferometry. The ridge detection makes use of the correlation between neighboring A-scans in a cross-sectional B-scan, and retrieves the ridge pixels corresponding to the physical boundaries of the sample from the noisy images. The result is then provided as the input for the 3D correlation detection algorithm which is based on the following logical assumptions:

1) A physical interface is a continuous object in a Cartesian coordinate system, and its image is also continuous in volumetric OCT image.

2) Noise, speckles, and small scattering sites are discrete and random in OCT image domain.

The consequences of the assumptions are:

1) The continuity of a physical surface in the image domain provides the correlation between two perpendicular cross-sectional views of the volumetric OCT image, e.g. X-Z and Y-Z cross sections, in which the OCT images of the surface are

independent and therefore the boundaries are extracted from these two cross sections based on different and independent sets of information. The two set of solutions, i.e. extracted boundary pixels from two perpendicular views should have a large probability to overlap with each other because of the continuity of a physical interface. The probability of the overlapping is very high if the image of the interface has good SNR, otherwise the probability is considerably smaller.

2) On the contrary the extracted pixels that correspond to noise, speckles, and small scattering particles or pores in an X-Z cross section have very small probability to overlap with the pixels extracted in the Y-Z cross section. This is because the phase of speckle is random [61] and speckles which are generated axially have no correlation in lateral direction. The images of the small scattering sites usually contain only a few pixels, and that is not enough to form good image in both the X-Z and the Y-Z view.

5.2.2 Method

To demonstrate the principle of this new 3D correlation detection algorithm we make use of the volumetric model of the ceramic sample with laser-milled microchannels. By applying the ridge detection algorithm described in 5.1 we can effectively extract the boundaries from each cross-sectional B-scan, and get a large set of images similar to that shown in Fig. 26. This is illustrated in Fig. 27 where the B-scans are located in the X-Z planes at adjacent Y-positions.

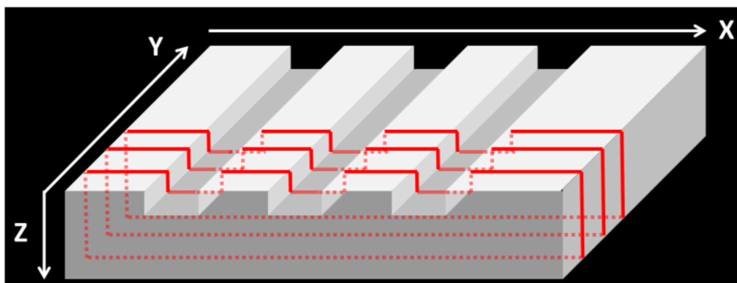

Fig. 27. Processing X-Z cross-sectional OCT images in the volumetric data using the ridge detection algorithm.

Fig. 28 shows an OCT image similar to that in Fig. 26 but corresponds to a different cross section in the volumetric OCT data, i.e. obtained at a different Y-

position. As can be seen the sub-pixel locations of the two images (Fig. 26 and Fig. 28) differ somewhat and the faulty pixels caused by speckles and found in one image will most probably not appear in the same place in another B-scan image. If the image quality is good the noise pixels will be rarely extracted. However, if the SNR in an OCT image is very low it is a very time-consuming process to find the optimal image processing parameters for each B-scan. The remaining noise pixels may also disrupt the image segmentation and degrade the uncertainty of the dimensional measurement in the OCT data.

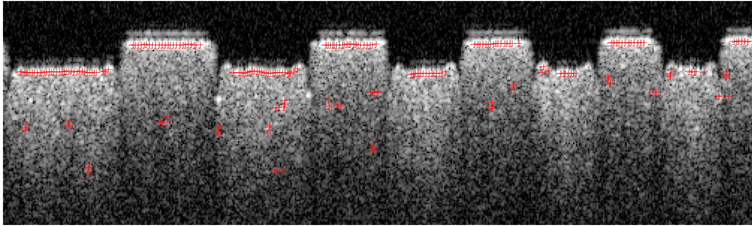

Fig. 28. Extracted ridge pixels of the boundaries of the microchannels. Some noise pixels are also extracted due to the non-optimized image processing parameters. The gray scale corresponds to a dynamic range of 45 dB.

To circumvent this problem we invented the new 3D correlation detection algorithm by realizing that the ridge detection can just as well be made on B-scans extracted as Y-Z planes. This is illustrated in Fig. 29. Here, the ridge pixels are extracted from Y-Z cross sections which are perpendicular to the X-Z cross sections. These results are independent of the X-Z cross-section images and provide new information. Similarly, some noise pixels that are not true ridge pixels corresponding to a physical interface may be extracted due to the speckles and low SNR.

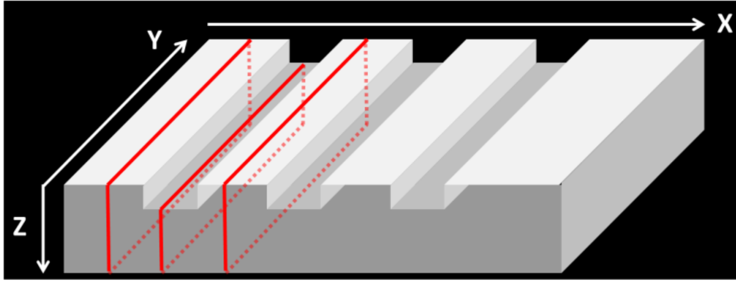

Fig. 29. Processing Y-Z cross-sectional OCT images in the volumetric data using the ridge detection algorithm.

The results of the ridge detection of the volumetric OCT data from X-Z and Y-Z views are presented in Fig. 30A and B respectively. Note that the ridge detection provides sub-pixel precision for the extracted pixels. Thus, the smallest unit to be used in the subsequent 3D correlation detection is 0.1 pixels, which is a pronounced advantage of this algorithm. The difference of these two results is obvious because each ridge pixel is obtained using different information provided by its neighborhood when comparing X-Z view and Y-Z view. The difference becomes particularly large when the channels are getting smaller. In this region the OCT image is much more noisy and blurry because the dimensions of the microchannels approach the OCT resolution limit.

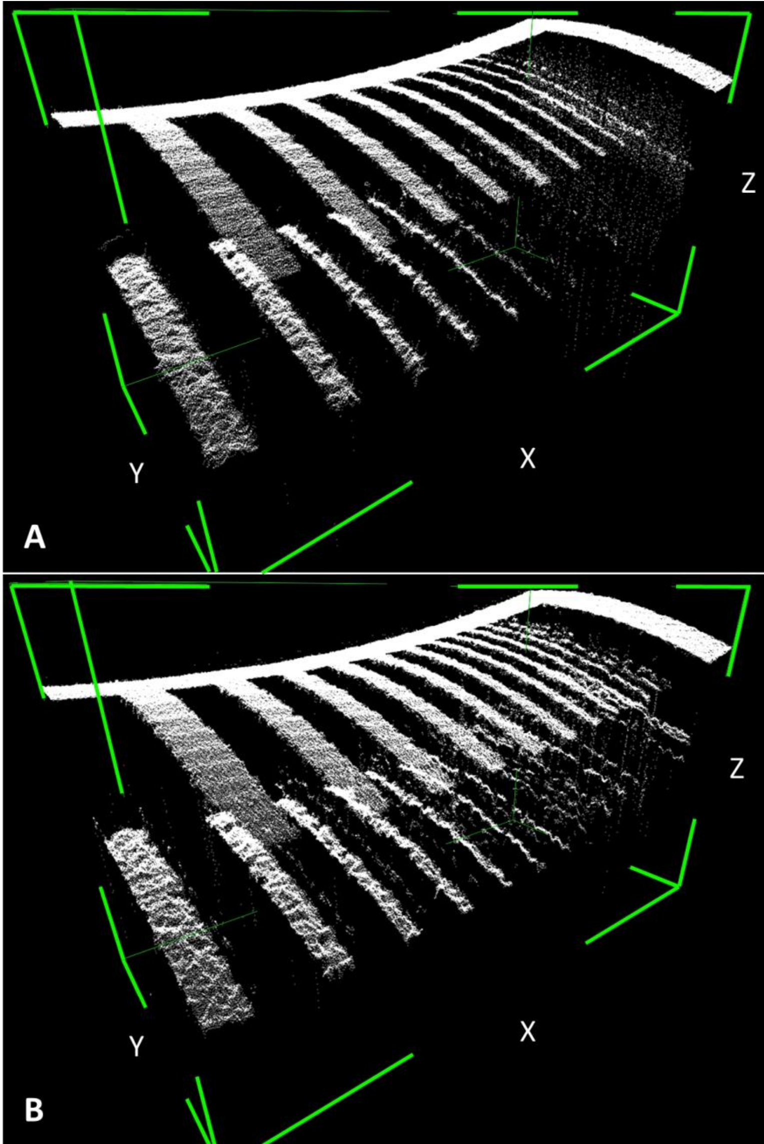

Fig. 30. Ridge detection results of the volumetric OCT data from X-Z view (A) and Y-Z view (B). Here the image processing result from X-Z view means that we process data in X-Z cross section and along Y direction. The same definition applies to Y-Z view.

Next step is carried out based on the assumptions that a physical interface is a continuous object in the Cartesian coordinate system and its image is also continuous in the volumetric OCT image, whereas the noise, speckles, and small scatter sites are discrete and randomly appearing in the OCT image domain.

If we combine the ridge detection results of the X-Z and Y-Z views it is very likely that ridge pixels from the real interface will match, but it is very unlikely that uncorrelated noise pixels from speckles and small scattering sites match. The condition of the matching is overlapping of two pixels with zero tolerance at sub-pixel resolution (0.1 pixels). This is a very strict condition and it offers a high accuracy segmentation of the physical interfaces present in the OCT data. This is particularly true when the surfaces are closely located. In many applications it is accurate enough to have the matching with zero tolerance at a one pixel (1 pixel). The detailed mathematical description of this process can be found in paper 8.

The effect of combining the ridge detection results of X-Z and Y-Z views (as shown in Fig. 30) is demonstrated in Fig. 31. Almost all remaining ridge pixels are corresponding to the desired surfaces, and the noise pixels are removed effectively. These pixels can be now used for further processing for the dimensional metrology of the microchannels.

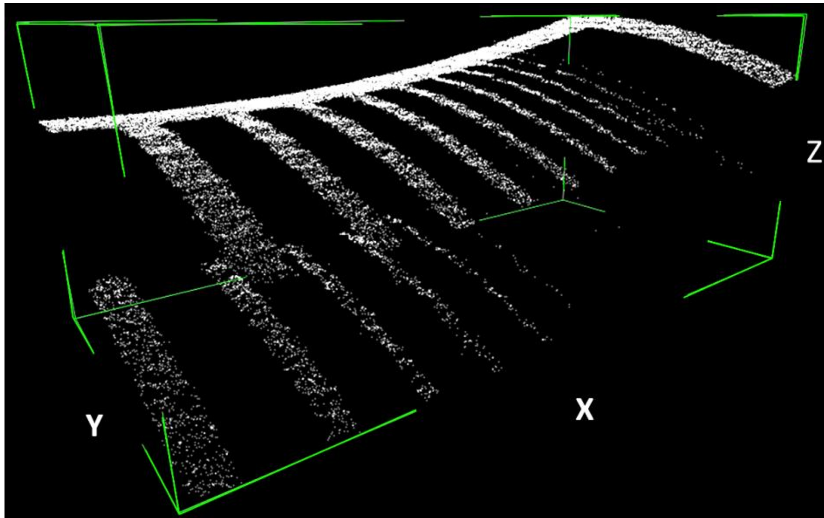

Fig. 31. Effect of combining the ridge detection results of X-Z and Y-Z views with a cross correlation acceptance window of 0.1 pixel in the Z-direction.

It is not difficult to segment the top and bottom surfaces of the microchannels. This can be done by separating two peaks in the histogram of the Z-positions of the ridge pixels as described in detail in paper 8. The segmented pixels are stored in two 3D arrays respectively, and least squares fitted to proper polynomial functions. In Fig. 32A a 4th order polynomial function has been fitted to the top surface data of the ceramic layer. The average depth of the channels can then be calculated as the average distance between the extracted pixels of the bottom in Fig. 32B and the fitted top surface. The surface curvature caused by a wavefront aberration of the OCT scanning optics and the tilting angles can be easily compensated for, and thus enhances the measurement accuracy, which will be discussed in section 9.2.2.

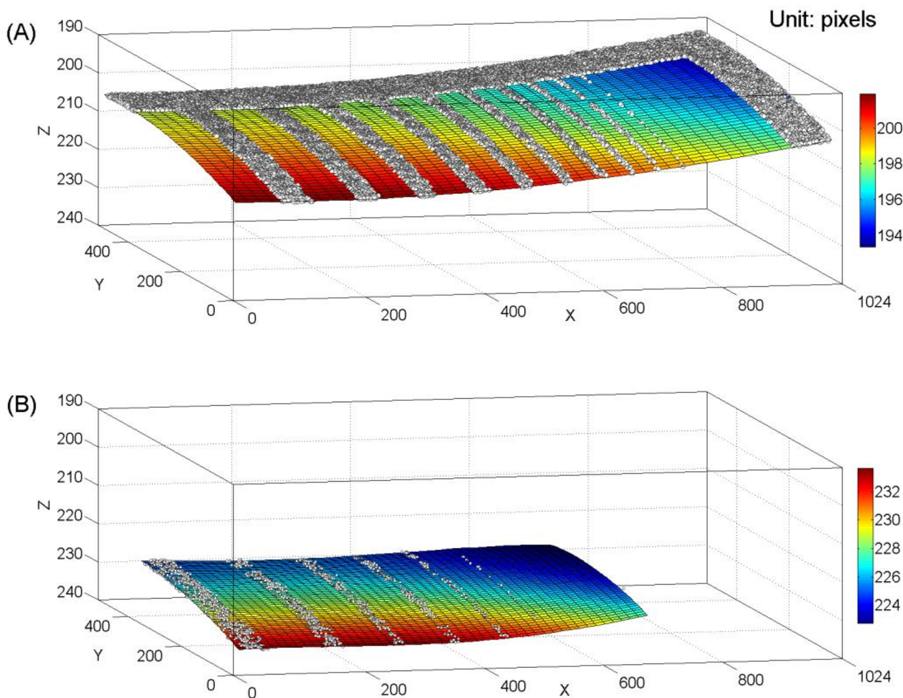

Fig. 32. Segmentation of the top (A) and channel bottom (B) surfaces of the ceramic layer based on the result shown in Fig. 31. The polynomial fitting of the surface are plotted by false colors and the extracted ridge pixels are presented as small gray dots. The unit of the axes is in pixels.

The best-fit functions also provide the Z-positions of the segmented surfaces as functions of X and Y coordinates, and they are used for retrieving the pixels from

the original volumetric OCT data which have the exact (X, Y, Z) positions. Hence, we obtain accurate positions of the surfaces, as well as the original interferometric signal levels on each pixel of the surfaces. The generated surfaces images are shown in Fig. 33.

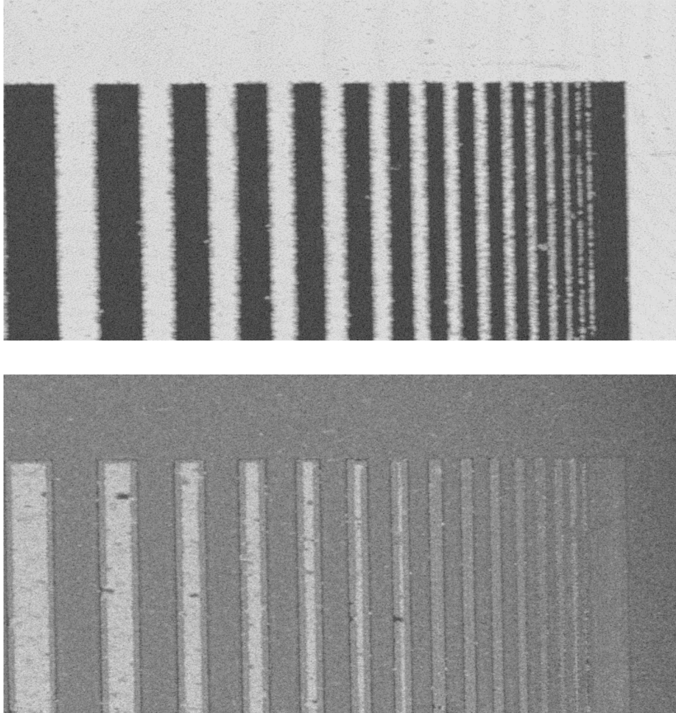

Fig. 33. Top-view gray-scale images corresponding to the top (upper) and channel bottom (lower) surfaces of the ceramic layer. The gray levels cover a 110 dB dynamic range. The brighter pixels in both images correspond to the surfaces, whereas the dark pixels in the upper image correspond to air and the dark gray pixels in the lower image originate from the backscattering signal within the ceramic material. The image size is 1024×512 pixels for $4\times4mm^2$ (the obtained image is twice as wide as the sample actually is).

From these enhanced images the channel widths can be measured using a standard Canny detection method combined with our sub-pixel refinement algorithm as demonstrated in Fig. 34.

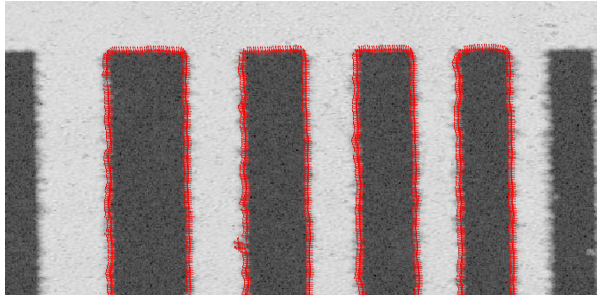

Fig. 34. Canny detection for edge detection and subsequent measurement of the widths of the channels using the upper image of Fig. 33. The small red crosses present the result of the edge detection. (This figure is extracted from paper 8)

Up till now we have demonstrated the 3D correlation detection method for measuring the depth and width of the microchannels in the volumetric OCT data. In the example we used a simple volumetric OCT image for the demonstration. However, the method is capable to handle much more complicated OCT images as will be shown in section 7.2, and the entire image processing procedure including the ridge detection and 3D correlation detection algorithms can be fully automated. The performance of the method is evaluated and presented in section 9.1.

6 Experimental

In this chapter the technical details of the ceramic samples, the optical measurement instruments, and the numerical calculation methods used in this thesis are described.

6.1 The alumina and zirconia ceramic samples

6.1.1 Manufacturing of the ceramic tapes

The sintered highly-dense polycrystalline alumina and zirconia ceramic materials that are shown in Fig. 35 are provided by Swerea IVF [132]. In the tape casting process a slurry of water, dispersant, binder and the ceramic powder are casted under a blade and creates a so called green tape on top of a plastic carrier. Details about the chemical contents of the alumina material are given in paper 3. The zirconia materials in this thesis were partially stabilized by an addition of 3 mole percent of yttria (Y_2O_3). This is the high temperature stable phase with good mechanical strength. After sintering at 1500ºC the binder is burnt away, and the final, shrunk ceramic sample is obtained. Its appearance is then white, with somewhat glossy surfaces.

The white appearance comes from the remaining porosity and depends on the tape casting and the sintering processes. More homogenous powders would lead to less defects and porosity. Less binder would also decrease the porosity, but the binder must be added in order to get a flexible green tape that can be handled. In the

sintering process a higher temperature and a longer heating time would lead to less porosity, but the grain growth will also be raised with higher temperature, which decreases the strength of the final material.

The porosity of the alumina and zirconia samples we have been measuring on is around 1%. Less porosity would generate less scattering and therefore improve the transparency of the materials. However, as we mentioned above this is a very complicated process in which many variables have to be traded against each other. From experience we know that small pores do not usually affect the strength, at least when the pores size is about 10 μm or smaller.

Fig. 35. Pictures of the sintered alumina (left) and zirconia (right) single layer samples, with a thickness of 186 μm and 212 μm, respectively. Note the fuzziness of the KTH logo when the light is transmitted through the samples.

6.1.2 Microstructures

The microstructure of a typical alumina sample is shown in the SEM image of Fig. 8, where both the pores and the grain boundaries are visualized by thermal etching of the cross section of the sample. The microstructure of our zirconia samples is similar to the alumina samples. In order to demonstrate the pores present in the two materials, two pieces of the sintered alumina and zirconia samples were polished by 1μm sized diamond powder and subsequently coated with a carbon film to reduce charging effects in the SEM. The images are shown in Fig. 36, where the grain boundaries are not well observed but the contrast of the pores is enhanced. As can be seen the pores in the zirconia material are generally smaller and more sparsely distributed. Their shapes also tend to be more spherical compared to those in the alumina material.

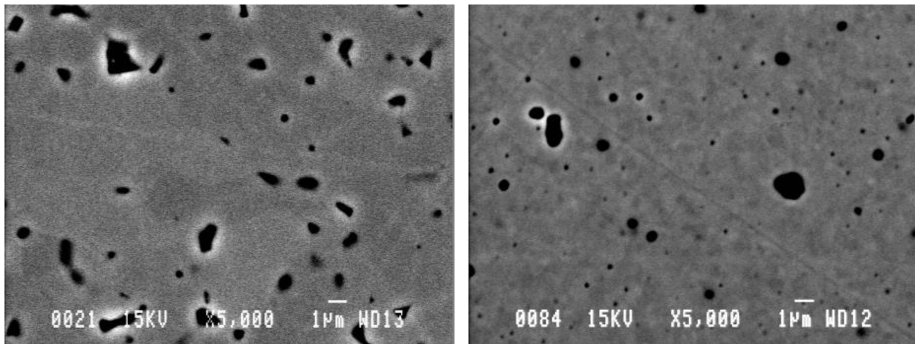

Fig. 36. SEM images of the prepared cross-section of the alumina (left) and zirconia (right) samples. The pores appear as the black areas. Image courtesy of Lars Eklund at Swerea IVF.

Using a proper threshold in the gray-scale images the areal porosity can be obtained, which can be related to the volumetric porosity by assuming that the pores are randomly-distributed. It is also possible to extract the pore size distribution by using some dedicated image processing algorithms. However, as we mentioned in section 2.3 the porosity and pore sizes obtained in this way are not very accurate and can only be used as an approximate reference value. The porosity estimated from the SEM images is thus around 1.8% for the alumina samples and 1% for the zirconia samples. These results deviate from the standard Archimedes method where the porosity is calculated as $1-(\rho_s/\rho_t)$, where ρ_s is the measured density of the sample, and ρ_t is the theoretical density of ceramic material. The porosity estimated from this method is around 1% for the alumina samples and 0.4% for the zirconia samples. The average pore diameters estimated from the SEM images are 0.6 μm and 0.3 μm for the alumina and zirconia samples, respectively. In section 7.1 these results will be compared to that obtained from the light scattering measurements

6.1.3 Laser milling of the ceramic samples

Laser milling is a promising technology for ceramic micromanufacturing by rapid prototyping. It is a very flexible and non-contact machining technique, which permits fine tuning of material removal at reasonable processing speed [133,134]. In this thesis pulsed lasers with repetition rates up to 500 kHz and nanosecond and picosecond pulse durations were used to manufacture dedicated artifacts. The laser

milling of the artifacts to establish the microchannels in the green and sintered alumina ceramic samples were done at Wrocław University of Technology and at MEC, Cardiff University, respectively. As shown in Fig. 37, the designed artifact has geometric features that may be typical for ceramic microcomponents developed for terahertz components in microwave applications, coolers for automotive lighting systems, and microfluidic devices and sensors.

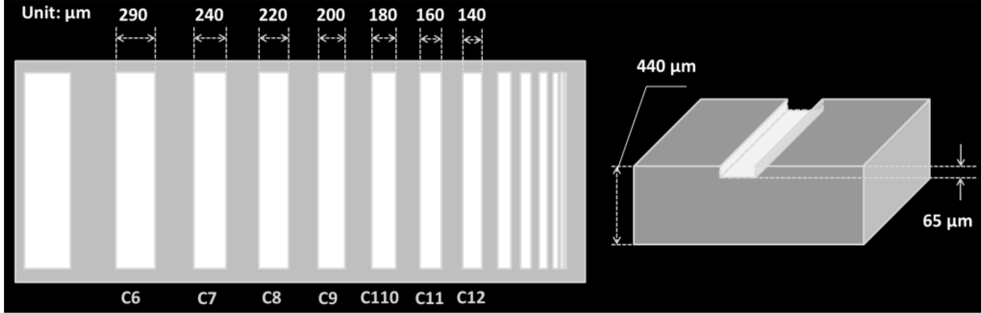

Fig. 37. Design of the microchannels machined into the sintered alumina layer by laser micromilling technology. The microchannel depth is designed to be 65 µm and the widths vary for each channel. In this thesis we focus on the channels C6, C8, C10, and C12.

6.1.4 Optical constants

The values of the optical constants of alumina can be found from data published in [135] for a wide wavelength region. As shown in Fig. 38, for the wavelength region of our interest ($\lambda = 0.5 \sim 6$ µm) the data of the real part of the refractive index, n, agrees very well with the calculated result from the equation [25]

$$n = \left(1 + \frac{1.023798 \times \lambda^2}{\lambda^2 - 0.0037759} + \frac{1.058264 \times \lambda^2}{\lambda^2 - 0.0122544} + \frac{5.280792 \times \lambda^2}{\lambda^2 - 321.3616}\right)^{\frac{1}{2}} \tag{6.1}$$

The imaginary part of the refractive index, i.e. the extinction coefficient k, representing absorption, is very close to zero in the range $\lambda = 0.5 \sim 4$ µm.

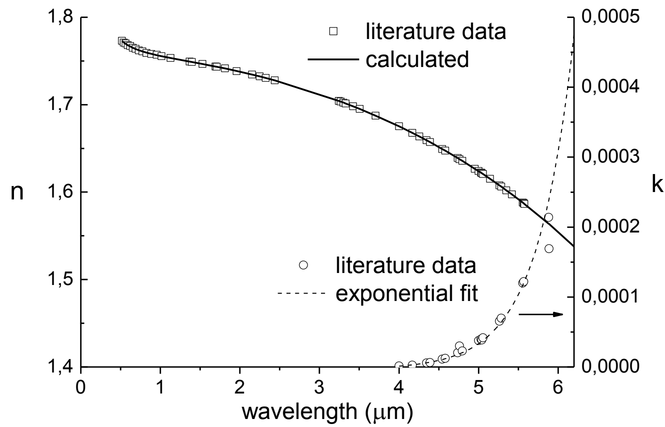

Fig. 38. Real (n) and imaginary (k) part of the refractive index of alumina. (This figure is extracted from paper 3)

As shown in Fig. 39 the real part of the refractive index, n, of the zirconia ceramic material can be calculated from the following equation that is derived from [136]

$$n = \left(1 + \frac{2.4255525 \times \lambda^2}{\lambda^2 - 0.0291903} + \frac{1.431390 \times \lambda^2}{\lambda^2 - 0.0031494} + \frac{12.27123 \times \lambda^2}{\lambda^2 - 686.8924}\right)^{\frac{1}{2}} \qquad (6.2)$$

The extinction coefficient k of the zirconia sample is very close to zero as well in the range $\lambda = 0.5{\sim}4$ μm and therefore neglected.

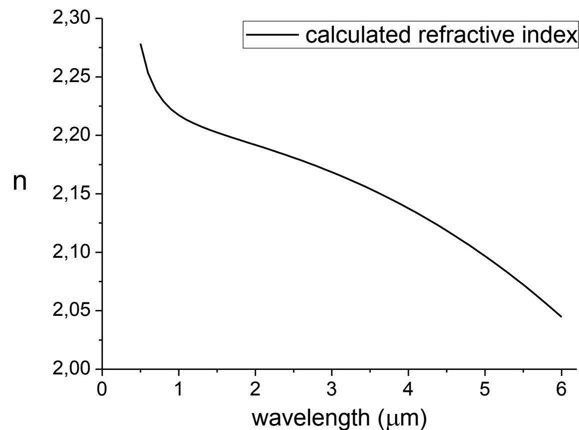

Fig. 39. Calculated refractive index of 3% mole yttria-stabilized zirconia.

6.2 Optical measurement

In this section the optical measurement instruments that are used in this study are listed and described, as well as the critical specifications of these systems.

6.2.1 Spectrophotometry

By spectrophotometric measurements of spectral transmittance and reflectance of our samples we get an opportunity to calculate the light scattering parameters (see section 2.2). By these measurements we can also find a suitable wavelength window where the alumina and zirconia are more transparent. A Perkin Elmer Lamda900 spectrophotometer with double beam and double monochromator was used for the wavelength range $\lambda = 0.5\sim2.5$ µm. The spectrophotometer was equipped with a 150 mm spectralon coated integrating sphere, allowing total and diffuse spectra to be recorded both for reflectance and transmittance. The recorded spectra were corrected for the sphere wall reflectance when necessary. The details about the correction method can be found in [137]. For the wavelength region $\lambda = 2.5\sim10$ µm a Perkin Elmer 983 spectrophotometer was used to measure the in-line (specular) transmittance.

6.2.2 OCT imaging systems

At an early stage in the Multilayer project we found that a perfect OCT-system for ceramic materials investigations did not exist. Thus, rather than buying a non-optimal system we decided to work together with OCT manufacturers and scientists in the forefront of developing new systems, and make use of these instruments to increase the understanding of their possibilities and limitations. The OCT systems that are evaluated in this thesis include Thorlabs [138] swept-source OCT (OCS1300SS) and spectral domain OCT (TELESTO, of which the system setup is shown in Fig. 40), and the Wellman laboratory swept-source OCT systems operating at 1.3 µm and 1.7 µm center wavelengths [56]. The specifications of the systems are given in Table 1.

Table 1 Specifications of the OCT systems

OCT systems	Thorlabs OCT		Wellman laboratory OCT	
	SS-OCT OCS1300SS	SD-OCT TELESTO	SS-OCT 1.3 µm	SS-OCT 1.7 µm
Center wavelength	1325 nm	1325 nm	1300 nm	1650 nm
Spectral bandwidth (FWHM)	>100 nm	150 nm	>80 nm	>60 nm
Maximum A-scan rate	16 kHz	91 kHz	10 kHz	10 kHz
Maximum sensitivity	100 dB	106 dB	105 dB	100 dB
Maximum scan width	10 mm	10 mm	4 mm	4 mm
Lateral resolution	25 µm	15 µm	< 20 µm	< 20 µm
Axial resolution	12 µm (in air)	< 8 µm (in air)	< 20 µm (in air)	< 20 µm (in air)

Fig. 40. Setup of Thorlabs spectral domain OCT system (TELESTO) [138].

6.2.3 Scanning white light interferometry

A well-calibrated Zygo NewView7300 [139] scanning white light interferometer (SWLI) at our department is used for measuring the depths and widths of the micro structures and the surface roughnesses of the ceramic samples. The environment temperature is controlled at 20±1 ºC for high-accuracy measurement also in the lateral directions over larger areas. The X,Y table movement is verified to be accurate to better than 5 μm. The interferometer works at the center wavelength $\lambda = 570$ nm and offers a sub-nanometer vertical resolution. The objective used in this thesis has a 3.8 μm lateral optical resolution and a 4.35×4.35 mm^2 lateral FOV. This system has been calibrated with surface roughness standards, with ceramic gauge blocks [140] for height measurement, and a traceable X,Y chromium on glass artifact.

6.3 Numerical Methods

6.3.1 Mie calculation

The background of the light scattering in ceramics has been discussed earlier in section 2.2 and 2.3. The scattering parameters to be calculated for the ceramic samples are the scattering coefficient μ_s and the anisotropy factor g, the latter equivalent to the average cosine of the scattering angle. These parameters were calculated using the open access FORTRAN code developed by Mishchenko et al. [23] for the Mie calculations. The scattering characteristics were computed for an ensemble of polydisperse, homogeneous spherical particles based on the Mie theory. This code allows calculation of scattering by a monodisperse particle and also by particles with different size distributions.

6.3.2 The Monte Carlo simulation

The Monte Carlo code used in this thesis has been developed and tested in previous studies for bio-tissues and paper samples [126,127]. The simulations of OCT images

are carried out by a consecutive step-wise calculation of individual A-scans that are further combined into a 2D matrix and displayed as an image in a logarithmic scale. Several millions of random photon trajectories were used in the simulations of the OCT response of the geometric features of our artifacts. Also surface roughness was included as a parameter, see further in paper 1, 3, and 6.

7 Experimental results

7.1 Optical properties of the ceramic samples

The spectra of the in-line transmittance of the sintered ceramic samples are shown in Fig. 41. The thicknesses of the two measured alumina samples are 101±4.5 μm and 346±3.5 μm, and the thicknesses of the two zirconia samples are 111±5.0 μm and 375±3.2 μm. The thickness represents an average point-to-point value as measured with an inductive spherical probe towards a spherical ball, in order to minimize any waviness contributions to the thickness measurement. As seen in Fig. 43, a high-transparency window can be found centered at the wavelengths $\lambda = 5{\sim}6$ μm. The transmittances are higher for the thinner samples compared to the thicker ones, and higher for zirconia compared to alumina because the former contains less and smaller pores as shown in Fig. 36. The in-line transmittance, which corresponds to radiation that has not been absorbed or scattered, is very weak for the thicker alumina and zirconia samples in the wavelength region $\lambda < 1$ μm. For $\lambda > 6$ μm the absorption increases rapidly and causes a significant drop in the in-line transmittance for both materials. The interference pattern caused by multiple internal reflections, becomes pronounced when the transmittance is higher than 60%.

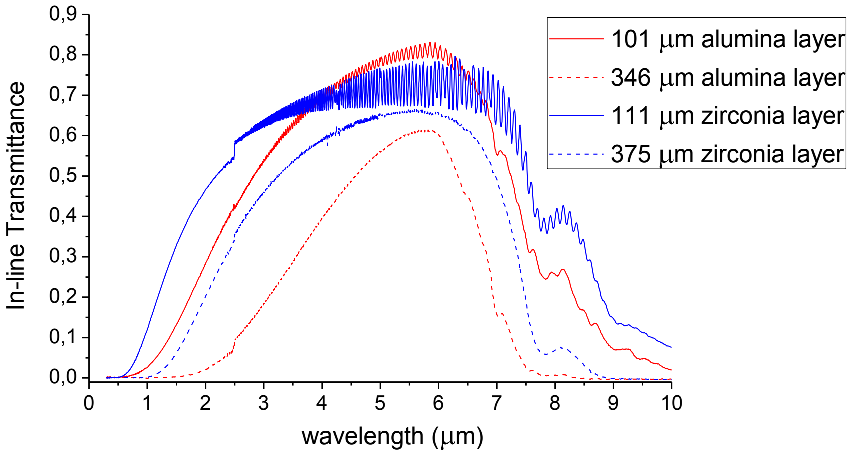

Fig. 41. Spectral in-line transmittance obtained as the ratio with and without the sample in the beam, of the sintered alumina and zirconia tapes having different thicknesses.

Since the available radiation sources for OCT emit up to a wavelength of 4.4 μm, we will focus our evaluation to the wavelength region $\lambda = 0.5 \sim 4$ μm. The scattering coefficients at these wavelength are calculated using equation (2.20), where the rms roughnesses, δ_{rms}, of the thinner alumina and zirconia samples are measured by the SWLI to be 60 nm (filtered with a cutoff spatial wavelength of 250 μm). The results are shown in Fig. 42 as curves, where the circles are the best-fit scattering coefficients obtained from Mie calculations with lognormal pore size distributions. Discrepancies at $\lambda = 0.5$ μm are mainly caused by the extremely low signal-to-noise ratio in transmittance measurements as can be seen in Fig. 41. This results in large uncertainty in calculating the scattering coefficients for both materials. Therefore, we skip values at this wavelength for the data fitting.

As a result of the fitting the microstructural information can be obtained, and it is listed in Table 2. This result is more reliable compared to the value we obtained from the SEM images in Fig. 36, as we make use of the full volume but not only a single cross-section.

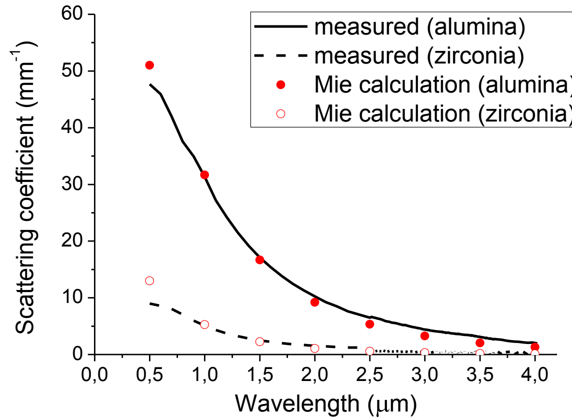

Fig. 42. Graphical presentation of the scattering coefficients vs. wavelength as derived from the in-line transmittance of the alumina and zirconia ceramic samples. The circles represent the results obtained from Mie calculations. (This figure is extracted from paper 6)

As can be seen in Fig. 42, the scattering is very strong in the visible region where the wavelength is comparable to the pore diameters, corresponding to the so-called Mie scattering regime. For the alumina sample the scattering coefficient decreases with increasing wavelength and approaches a very small value at 4 μm where absorption will start playing a role on the total light extinction. For the zirconia sample, having smaller pore sizes and less porosity, the scattering coefficient is lower than that of the alumina sample. From $\lambda = 2$ μm the scattering coefficient becomes very small and remains at this level for the longer wavelengths.

Table 2 Pore size distributions and porosity of the alumina and zirconia samples

	Mean pore diameter	Standard deviation of pore size distribution	Porosity
Alumina	0.4 μm	0.35 μm	≈ 1%
Zirconia	0.2 μm	0.32 μm	≈ 0.2%

The anisotropy factors of the alumina and zirconia samples obtained from the Mie calculations also show a descending trend with wavelengths (Fig. 43). The smaller the g factor is, the more isotropic is the scattering by a single small pore, and the smaller is the ratio of the pore size to the wavelength. The g factor of the

alumina sample containing larger pores is therefore higher compared to that of the zirconia sample in this wavelength region.

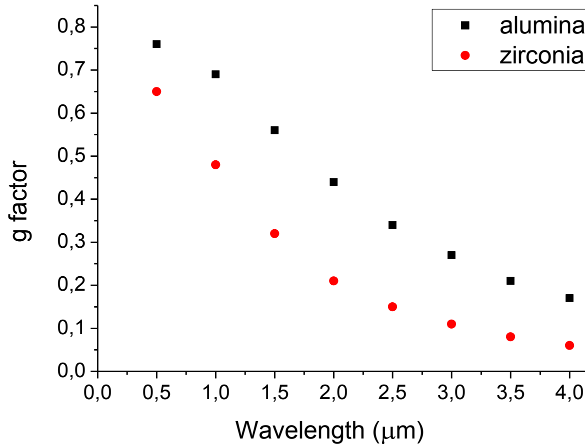

Fig. 43. Derived anisotropy factors from Mie calculations of the alumina and zirconia ceramic samples. (This figure is extracted from paper 6)

7.2 Dimensional measurements with OCT

The results of the dimensional measurements using the experimental OCT images of the alumina and zirconia layers and the ceramic stacks with embedded microchannels will be presented in this section. The layer structure of the ceramic samples to be measured is shown in Fig. 44. The basic geometric model is a two-layer ceramic stack where the thicknesses of the top layers are varying from 100~450 μm and the laser-milled microchannels have a designed depth of 65 μm and various widths as shown in Fig. 37. The model mimics ceramic micro devices with embedded features inside the material. The two layers are not really bonded together as we need to maintain traceability of the layer thicknesses, surface roughness, and dimensions of the microchannels. This is highly important as OCT metrology is the main topic of this thesis. Consequently, an air gap will exist between the two layers.

This non-bonded geometry also allows for making the OCT images of the channels with and without the top layer for direct comparison of the effects of scattering on the dimensional measurement. So far there is neither such non-

destructive technology providing accurate measurement of embedded features in ceramics with well-known measurement uncertainty and repeatability, nor standard calibration samples with accurately made embedded features.

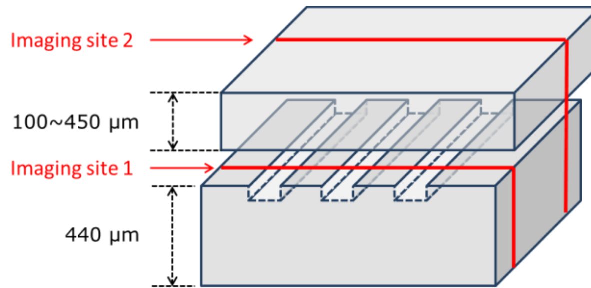

Fig. 44. Geometric model of the two-layer ceramic sample stack for OCT imaging. The designed dimensions of the microchannels can be found in Fig. 37. The imaging sites are marked with the red frame.

7.2.1 Microchannels in the free surface

The measurement of the open channels is done at the imaging site 1 as shown in Fig. 44. Here, the function of the OCT is very similar to a standard SWLI if we are only interested in the surface features. An example of the 3D OCT image at this site is shown in Fig. 45, with subsequent image processing results already shown in Fig. 32 and Fig. 33. The average depth of the channels is calculated as the average height deviation between the extracted pixels of the channel bottom (Fig. 32B) and the fitted reference surface (Fig. 32A). The channel widths are measured using a standard Canny detection method as shown in Fig. 34. The results, compensated for the curvature and tilting of the surface and are listed in Table 3 with a confidence level of 99.7%. The uncertainty of the result is calculated based on the central limit theorem [141] of a large number of measurements along the channels. However, it must be emphasized here that any systematic error introduced by the probe beam interaction with the sample structure has not been taken into account. This uncertainty of absolute edge definition may thus be considerably larger than the statistical variation reflected in the uncertainty given in Table 3.

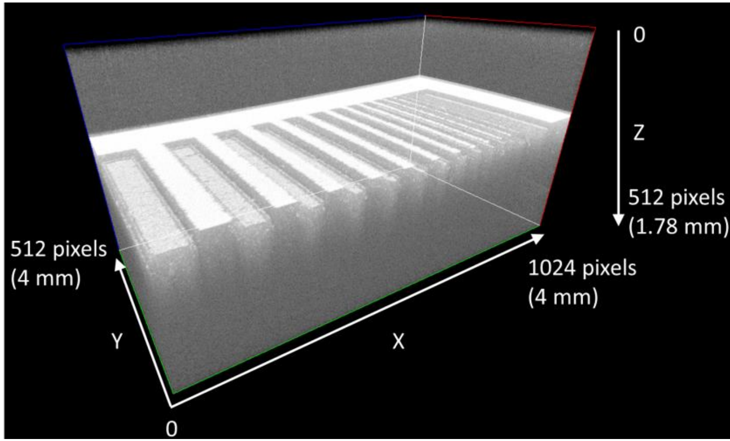

Fig. 45. The 3D perspective OCT image of the ceramic layer with laser-milled microchannels. The total depth of the image is 1.78 mm (optical distance). The image is rendered using MIP method [129]. (Thorlabs TELESTO SD-OCT, center wavelength 1.325 μm).

Table 3 Measured depth and widths of the microchannels in free surface.

Average depth (μm)	Widths (μm)			
	Channel 6	Channel 8	Channel 10	Channel 12
66.2±0.1	255.1±2.8	185.0±2.7	148.3±2.6	106.9±2.7

The given uncertainty refers to the statistical 3σ variation in the measurements.

7.2.2 Embedded microchannels in alumina

Measurements of embedded channels were made on the two-layer ceramic stack, corresponding to the imaging site 2 in Fig. 44, where the microchannels are covered by a 188 μm thick alumina top layer. Except for a small air gap between the layers, this mimics the situation of measuring embedded channels in fully bonded ceramic devices. In Fig. 46 the 3D perspective image provides an overview of the volumetric OCT data. From the image the top surface of the microchannels can be clearly detected at this embedded depth, whereas the signals from bottom parts are very weak because of its higher surface roughness, caused by the laser-milling process, and the scattering that also occurs in the alumina top layer.

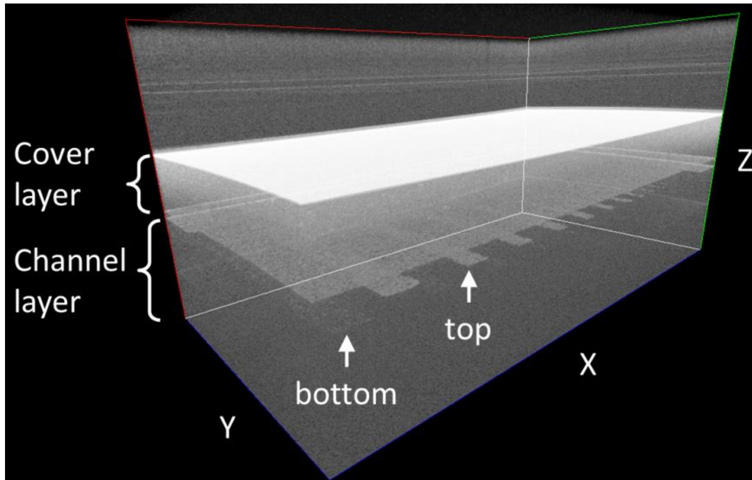

Fig. 46. The 3D perspective OCT image of the two-layer ceramic stack (render mode is MIP). The channel layer is embedded beneath a 188 μm thick alumina layer. The image contains 1024×512×512 pixels which correspond to 4mm×4mm×1.78mm in X, Y and Z directions, respectively, where Z axis presents optical distance. (Thorlabs TELESTO SD-OCT, center wavelength 1.325 μm)

The image processing procedure is the same as that is demonstrated in chapter 5. The segmented surfaces using the 3D correlation detection are shown in Fig. 47, where the surfaces are fitted using 4th order polynomial functions. Note that the bottom surfaces of the channels cannot be extracted because the corresponding OCT signal is too weak.

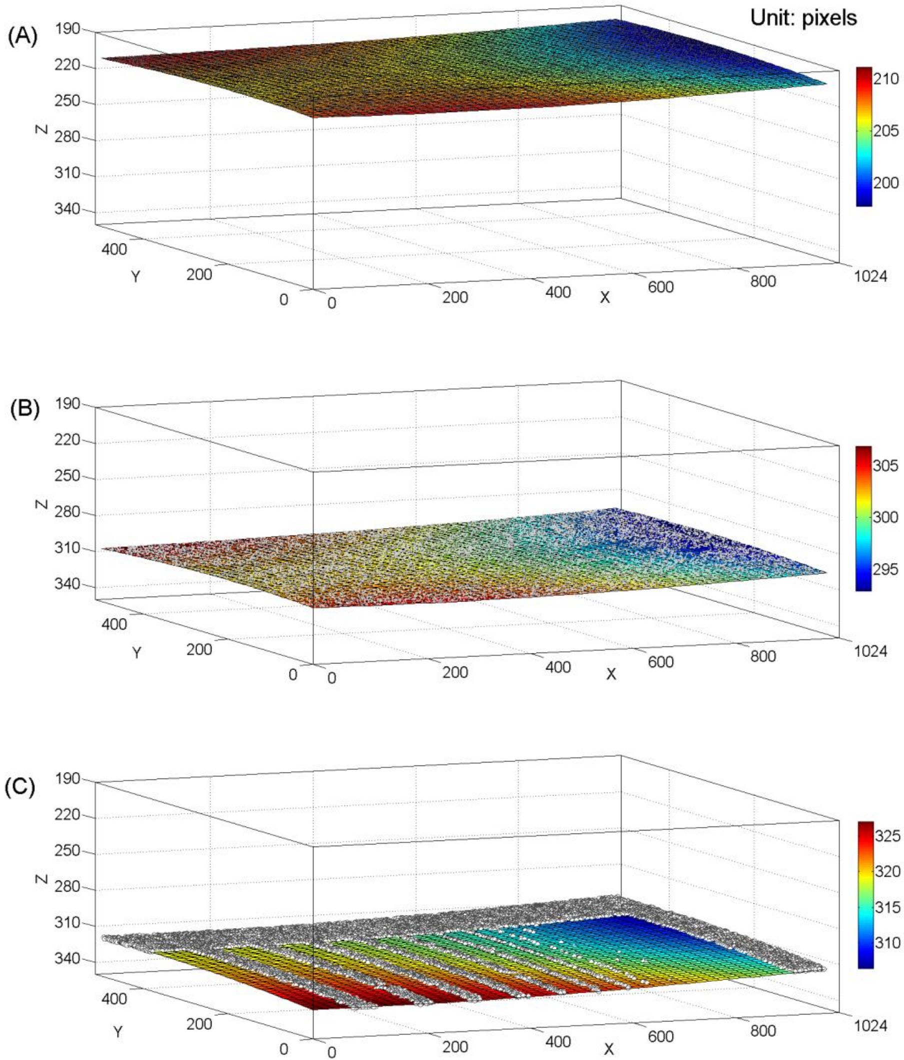

Fig. 47. Segmentation of the surfaces of the alumina ceramic stack from the OCT data in Fig. 46. Three surfaces are extracted: the front (A) and rear (B) surface of the top layer, and the front surface of the channel layer (C). The polynomial fittings of the surfaces are plotted by false colors and the extracted ridge pixels are presented as small gray dots. The unit of the axes is in pixels.

The top-view OCT image of the top surface of the embedded channel layer is retrieved using the fitting functions and the result is shown in Fig. 48. Here we

measure the widths of the microchannels and the results are shown in Table 4 with a confidence level of 99.7%. As discussed in relation to Table 3 above, these uncertainty values are also based on the statistical variation in the measurements, without considering possible systematic effects caused by edge definition problems.

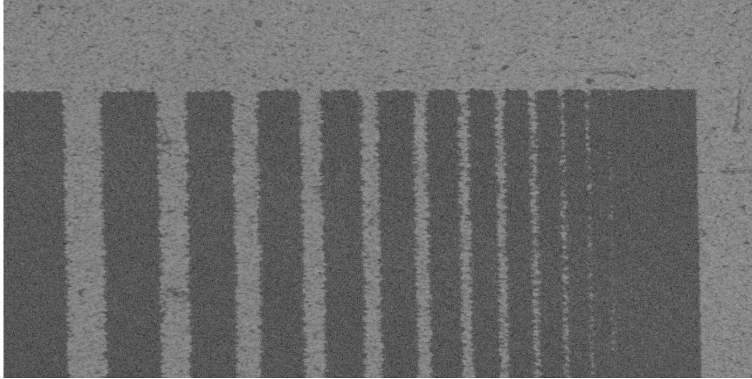

Fig. 48. Top-view gray-scale images corresponding to the top surfaces of the alumina ceramic channel layer in the X-Y plane. The gray levels correspond to 110 dB dynamic range. The light-gray pixels correspond to the surfaces, whereas the dark pixels correspond to air. The image size is 1024×512 pixels for 4×4mm^2 (the obtained image is twice as wide as the sample actually is).

Table 4 Measured widths of the embedded microchannels in alumina.

Widths (μm)			
Channel 6	Channel 8	Channel 10	Channel 12
301.3±3.1	235.3±3.0	195.5±2.8	152.1±2.8

The given uncertainty refers to the statistical 3σ variation in the measurements.

7.2.3 Embedded microchannels in zirconia

The zirconia measurements are made on a similar two-layer ceramic stack, where the microchannels are covered by a 375 μm thick zirconia top layer. In Fig. 49 the 3D perspective image provides an overview of the volumetric OCT data obtained at $\lambda = 1.3$ μm. It can be seen that the bottom surfaces of the channels can be detected much more clearly in this case compared to Fig. 46, even though the embedded

depth is almost doubled. This is mainly because the scattering coefficient of the zirconia sample is much smaller than that of the alumina sample in this wavelength region as can be seen in Fig. 42.

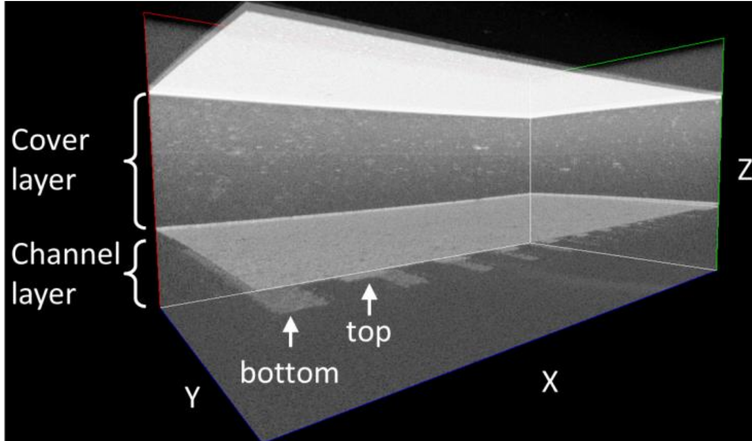

Fig. 49. The 3D perspective OCT image of the two-layer ceramic stack (render mode is MIP). The channel layer is embedded beneath a 375 μm thick zirconia layer. The image contains 1024×512×512 pixels which correspond to 4mm×4mm×1.78mm in X, Y and Z directions, respectively, where Z axis presents optical distance. (Thorlabs TELESTO SD-OCT, center wavelength 1.325 μm)

After image processing the segmented surfaces are revealed as shown in Fig. 50, where the surfaces are fitted using 4th order polynomial functions. Fig. 50A and Fig. 50B present the extracted pixels from the rear surface of the top layer and the front surface of the channel layer, respectively. In some regions we can observe a loss of pixels. This happens when the two surfaces are so close to each other so the OCT system cannot resolve them in the axial direction. However, there are still a large number of pixels being extracted, and they provide sufficient information for extracting the surfaces. This OCT image (Fig. 49) is a good demonstrator of the capability of our image processing algorithm being able to handle extremely difficult segmentation tasks in a noisy background. More details can be found in paper 8.

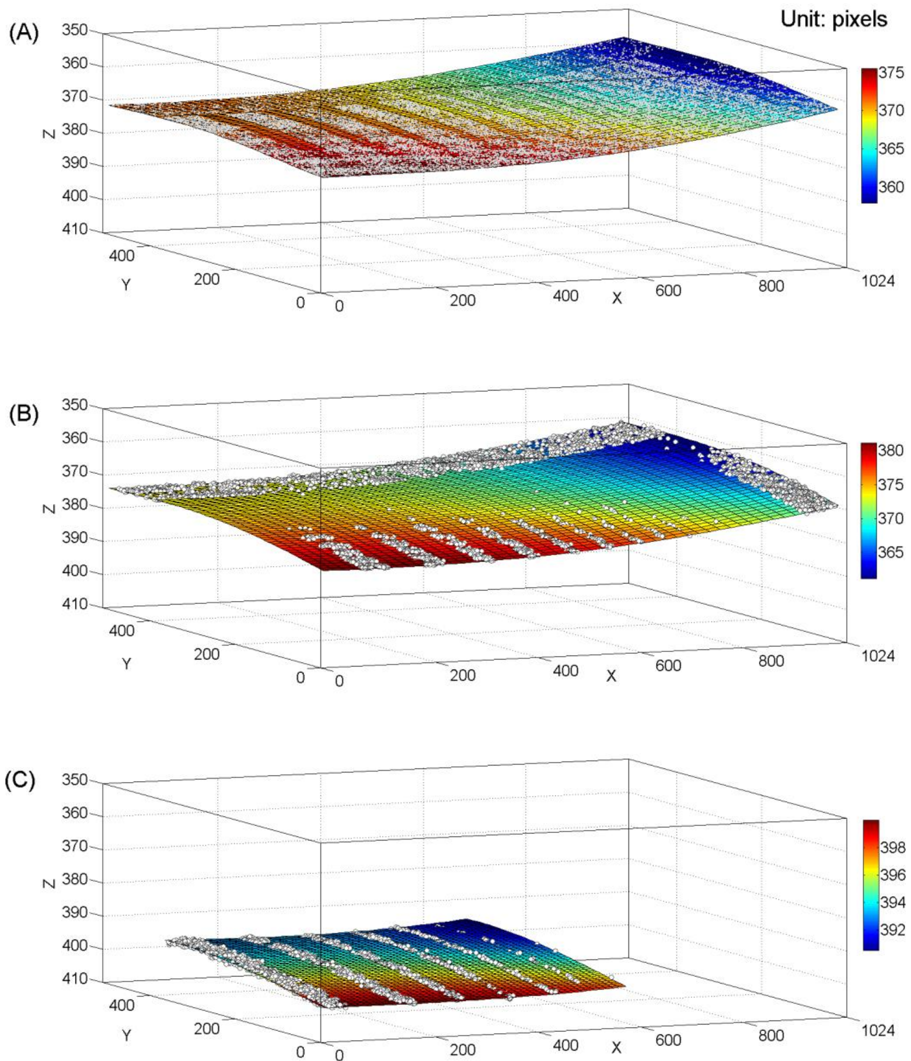

Fig. 50. Segmentation of the surfaces of the zirconia ceramic stack from the OCT data in Fig. 49. Three extracted surfaces are shown: the bottom surface of the top layer (A), and the top (B) and bottom (C) surfaces of the channel layer. The polynomial fittings of the surfaces are plotted by false colors and the extracted ridge pixels are presented as small gray dots. The unit of the axes is in pixels. The surface curvature caused by a wavefront aberration will be discussed in section 9.2.2.

Fig. 51 shows the top-view OCT image of the top and bottom surfaces of the channel layer that are retrieved using the fitting functions, from which we measure the widths of the micro channels and the result is shown in Table 5.

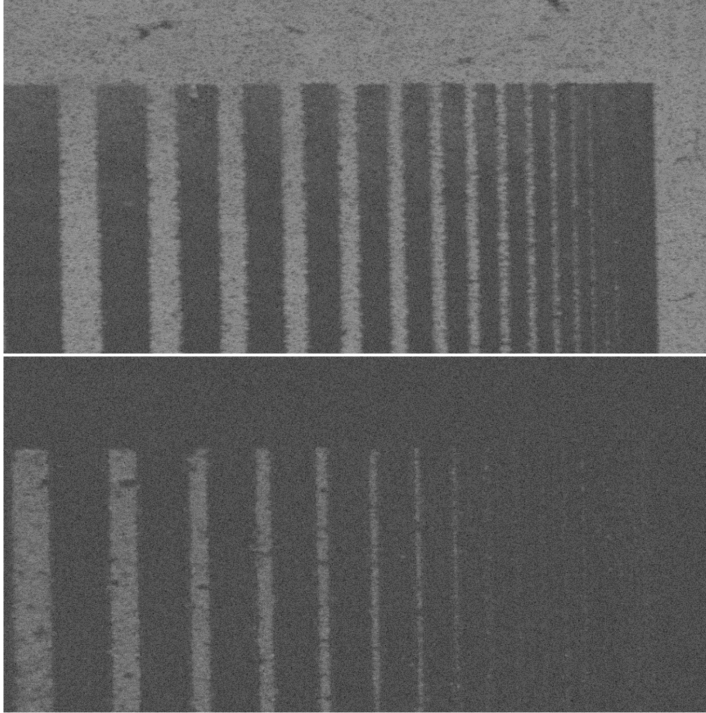

Fig. 51. Top-view gray-scale images corresponding to the top (upper) and bottom (lower) surfaces of the zirconia ceramic layer. The gray levels correspond to 110 dB dynamic range. The light gray pixels in both images correspond to the surfaces, whereas the dark pixels in the upper image correspond to air and the dark gray pixels in the lower image are resulted from the backscattering signal in the ceramic material. The image size is 1024×512 pixels for $4 \times 4 mm^2$ (the obtained image is twice as wide as the sample actually is).

Table 5 Measured depth and widths of the embedded microchannels in zirconia

Average depth (µm)	Widths (µm)			
	Channel 6	Channel 8	Channel 10	Channel 12
66.6±0.1	282.4±3.1	220.5±3.4	180.4±3.4	137.5±3.5

7.3 Defects detection

Defects in ceramic samples may be present in the form of large pores, delamination at interfaces, and deformations. Fig. 52 shows two cross-sectional OCT images of sintered zirconia layers. The top and bottom surfaces can be clearly observed in both images. Several extraordinary bright spots are found in the images, of which some are pointed out by the arrows. This is indicative of strong backscattering by relatively large pores with diameters larger than 10 µm. These defects may become the starting points of potential cracks in the material. As can be seen, these pores cause strong backscattering and act as blockers of the information below their position in the material. The reason for this is twofold. A large portion of the radiation will be back-reflected or scattered away by the pore when the photons are travelling down in the material and the limited number of non-scattered photons passing through the pore will be scattered away when returning up after reflection at deeper levels. This effect appears as "shadows" in the OCT images and can be observed in the alumina material as well. It may cause problem for the image processing and boundary detection.

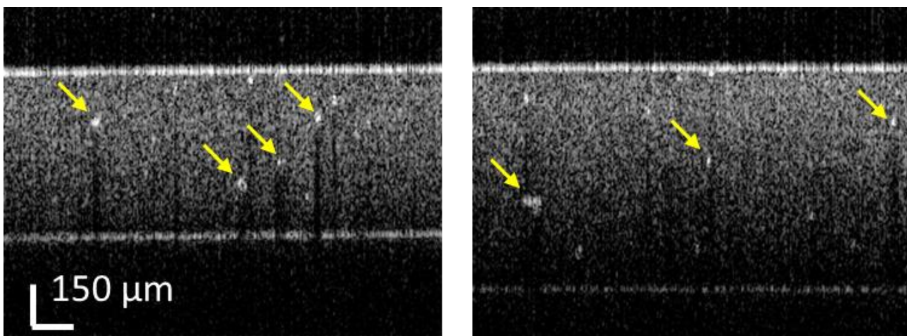

Fig. 52. Cross-sectional OCT images of two sintered zirconia layers with the thickness of 279 µm (left) and 375 µm (right). The vertical scale bar represents optical distance, and the gray scale represents a dynamic range of 45dB. (Thorlabs SS-OCT, center wavelength 1.325 µm)

Deformation and delamination between two stacked ceramic layers are not uncommon in the sintering process. In Fig. 53 we show the cross-sectional OCT image of a non-bonded two-layer alumina stack that mimics a delamination in multi-

layered ceramic materials. In the left part of the image the delamination is detected as the presence of a back-reflected signal. To the right a thin wedge-shaped air gap between two layers is created due to the surface deformation caused by the sintering process or by external strain. This air gap exceeds the axial resolution of the OCT system, and therefore two boundaries are detected. The smallest detectable separation between the two layers shown in the enlarged image is found to be 3.5 pixels corresponding to 14.4 µm.

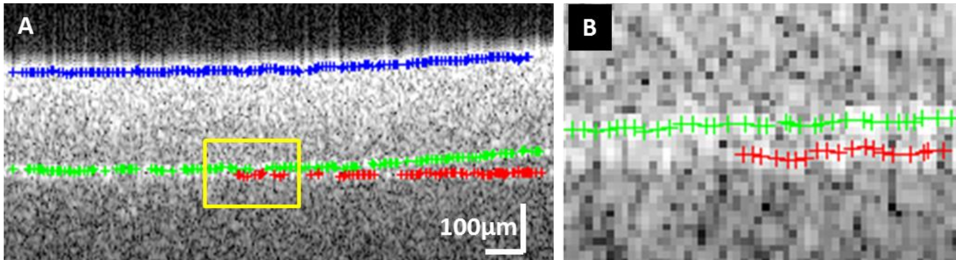

Fig. 53. Cross-sectional OCT image of a non-bonded two-layer alumina stack with a warped upper layer. The ridge detection result is plotted with small crosses (A), and the enlarged graph of the marked area (B). The vertical scale bar represents optical distance. (Wellman laboratory 1.3 µm SS-OCT)

The cross-sectional OCT image of an embedded laser-milled microchannel is shown in Fig. 54. It demonstrates that the geometric dimensions of a laser machined channel may be distorted and non-rectangular. The shape of the microchannel is dependent on the quality of the laser milling process and the shrinkage of the ceramic material during sintering process. Without providing our ridge detection algorithm with a priori model information, the boundaries of the layers and the embedded feature are well extracted. Fig. 54B clearly shows that despite the high noise content in the image the extracted channel boundary is well described.

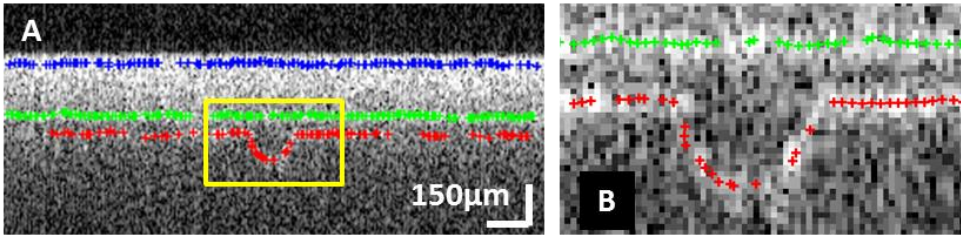

Fig. 54. Cross-sectional OCT image of a two-layer alumina stack that corresponds to the imaging site 2 marked in Fig. 44. The original image and the ridge detection result are shown in (A), and the enlarged graph of the marked area (B). The vertical scale bar represents optical distance. (Thorlabs SS-OCT)

7.4 Enhanced probing depth by 1.7μm OCT

As shown in Fig. 42 a longer wavelength may reduce the scattering in the ceramic materials. However, most OCT systems are operating at wavelengths shorter than 1.3 μm, as these wavelengths are more suitable for biomedical samples. In this section we present for the first time OCT measurements performed on ceramic materials at 1.7 μm wavelength. These results are compared with OCT measurements made at 1.3 μm with similar optical configurations, resolutions and detection sensitivities.

A two-layer alumina stack with the embedded microchannels (similar to that in Fig. 46) is used for evaluating the probing depth of the two OCT systems, where the top layer has a thickness of 293±3.5 μm. The volumetric OCT image obtained using the two systems are shown in Fig. 55, where a pronounced difference of the scatter-limited probing depth can be observed. In the left hand image the microchannels can be hardly detected and accurate dimensional measurements should not be made from an image of that quality. On the contrary, the right hand image obtained at 1.7 μm, shows much higher quality and proves that our expectation that longer wavelengths will improve the possibility of accurate measurements of embedded structures is correct.

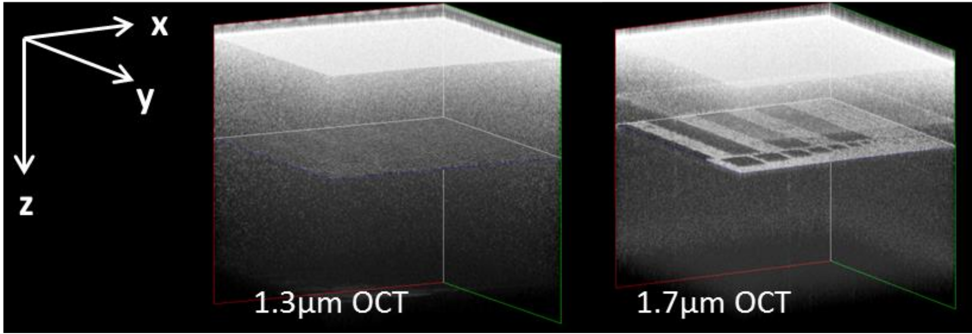

Fig. 55. Volumetric OCT image obtained using Wellman laboratory 1.3 µm (left) and 1.7 µm (right) OCT systems for the microchannels embedded beneath a 293 µm alumina layer. The image field of view corresponds to a volume of 4mm×4mm×2mm (X, Y and Z directions), where Z axis represents optical distance. The image is rendered using MIP method and the gray scale represents a dynamic range of 45dB.

The improvement of probing depth is obvious even though the scattering coefficient is only reduced from 22.4 mm^{-1} for $\lambda = 1.3$ µm to 14.4 mm^{-1} for $\lambda = 1.7$ µm. Further improvement may be expected if even longer wavelengths are used.

However, the decrease of scattering can also be problematic in some cases if the industrial ceramic samples contain multiple layers with highly reflecting surfaces acting as mirrors. Hence, mirrored images of ceramic boundaries may be observed due to double or even multiple reflections. In Fig. 56 a false interface is observed (mirrored image) because of internal reflections present at 1.7 µm OCT but not by 1.3 µm.

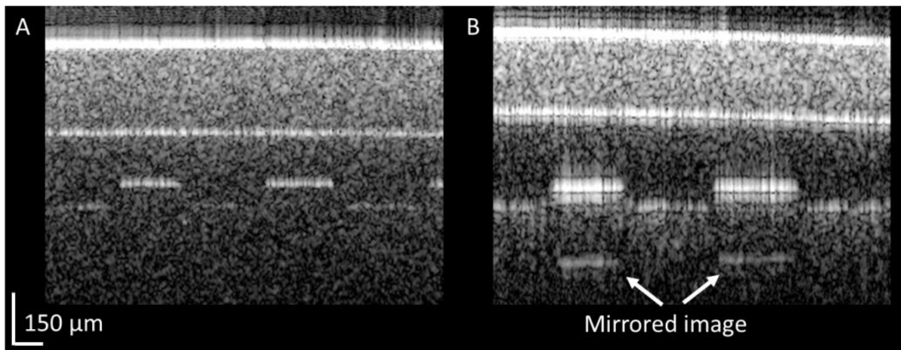

Fig. 56. Cross-sectional OCT image obtained using Wellman laboratory 1.3 µm (A) and 1.7µm (B) OCT systems for the microchannels embedded beneath a 150 µm alumina layer. The mirrored image artefacts are shown by the arrows. The vertical scale bar represents optical distance, and the gray scale represents a dynamic range of 45dB.

We have also found that the detection possibility for embedded features in the ceramic materials is not only limited by the bulk scattering but also depends on the surface roughness. In Fig. 58 the λ = 1.3 and 1.7 µm cross-sectional OCT images of the alumina sample stack with 450 µm-thick polished and un-polished top layers are shown. The bottom boundary of the polished 450 µm-thick alumina layer can be detected at 1.7 µm (B) but not at 1.3 µm (A) because of less scattering at the longer wavelength in the alumina material. The laser-milled channels are not detected at all because of the large thickness of the top layer which generates strong scattering and the surface roughness of the channels.

Fig. 57C and Fig. 57D present the OCT measurements of the alumina stack with the 450 µm un-polished alumina flat layer on top. In this case the 1.7 µm OCT measurement (D) cannot detect the rear boundary due to the additional scattering by the rougher surface.

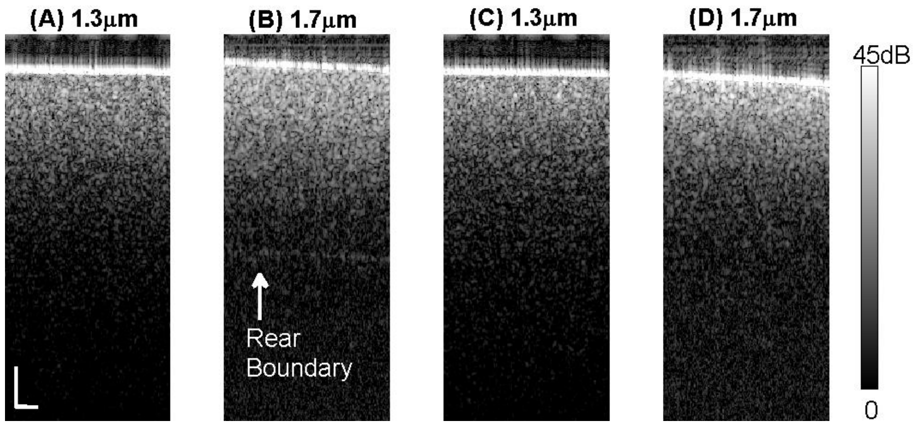

Fig. 57. Cross-sectional B-scan OCT images of the alumina sample stack. A) $\lambda = 1.3$ μm, polished top layer; B) $\lambda = 1.7$ μm, polished top layer; C) $\lambda = 1.3$ μm, un-polished top layer; D) $\lambda = 1.7$ μm, un-polished top layer. The vertical (optical distance) and horizontal bars are 150 μm. The background noise is slightly higher for the 1.7μm OCT system. (Wellman laboratory OCT systems are used. This figure is extracted from paper 6)

The OCT images shown in Fig. 57 are used as references for the comparison with the Monte Carlo simulations that are made on the physical bases and use the experimental optical parameters both for OCT systems and samples.

8 Simulation results

As shown by the optical transmittance measurements of alumina and zirconia in section 7.1 there is a “window” in the mid-infrared that might be useful for detecting embedded features at deeper levels by the OCT technique. However, no such OCT instruments have been designed yet. In this chapter we therefore perform Monte Carlo simulations to predict the expected OCT response in the near to mid-IR wavelength regions. The effect of rough surfaces on the detection of the embedded boundaries is also discussed. As mentioned before, surface roughness and porosity are the main causes of the scattering in highly-dense alumina and zirconia ceramics for the near IR wavelength region. Through the simulations we will find out if OCT imaging may benefit from the reduced surface and bulk scattering by increasing the wavelength. The technical details about the simulations can be found in paper 6.

8.1 Geometric models and input parameters

The geometric model of the simulation is based on the experimental two-layer stack shown in Fig. 44, where a flat layer is placed atop the bottom layer with a rectangular channel in its upper surface. Fig. 58 shows the geometry of the imaging cross section input to the Monte Carlo simulation program. The only difference between model I and II is that the rms roughness δ_{rms} of the surfaces of the top layer are higher in model II, 90 nm for the un-polished, compared to 30 nm for the polished model I case. The surfaces of the bottom layer have $\delta_{rms} = 90$ nm, and a

higher roughness, $\delta_{rms} = 140$ nm, is used for the laser-milled surface in the channel.

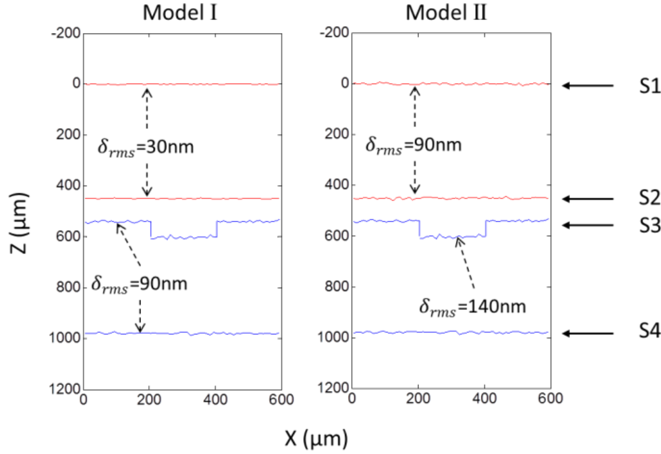

Fig. 58. Schematic cross-sectional geometric models input to the Monte Carlo simulation program for simulating OCT images. The axes correspond to physical lengths in micrometers. The models are applied to both alumina and zirconia samples for direct comparison of the simulation results. S1, S2, S3, and S4 correspond to the four surfaces in the model.

Table 6 lists the calculated refractive index n, the scattering coefficient μ_s, and the anisotropy factor g of the alumina and zirconia materials for the five wavelengths to be used in the simulation.

Table 6 Optical properties input to the Monte Carlo simulation program

	Alumina			Zirconia		
λ (μm)	n	μ_s (mm^{-1})	g	n	μ_s (mm^{-1})	g
1.3	1.751	22.4	0.61	2.207	3.2	0.38
1.7	1.744	14.4	0.54	2.198	2.0	0.27
2	1.738	10.6	0.44	2.192	1	0.21
3	1.712	4.6	0.27	2.169	0.9	0.11
4	1.675	2.1	0.17	2.138	0.7	0.06

The input OCT parameters are set to fit the experimental setup and are listed in Table 7. The effective detector radius and detection angle corresponds to the aperture stop and the numerical aperture (NA). More details about these parameters can be found in [123,126].

Table 7 OCT parameters input to the Monte Carlo simulation program

Pixel size	Lateral resolution	Axial resolution	Effective detector radius	Effective detection angle
10×10μm	20 μm	12 μm	12 μm	2 degrees

The numbers of the photons launched for each simulated A-scan are 50 millions in order to provide enough statistics comparable to a sensitivity of 100dB in a real measurement.

8.2 Comparisons of A-scans

The average A-scans of the measured OCT image (at $\lambda = 1.7$ μm) of the polished and un-polished alumina samples (shown in Fig. 57B and Fig. 57D) are used as verification references to the average A-scans of the simulated images at $\lambda = 1.7$ μm, alumina, model I and II. As shown in Fig. 59, the simulations of the polished and un-polished model both agree very well with the experimental results. It is important to note the small peak located at 785 μm, which corresponds to the rear boundary of the polished top layer (S2), can only be observed in Fig. 59A.

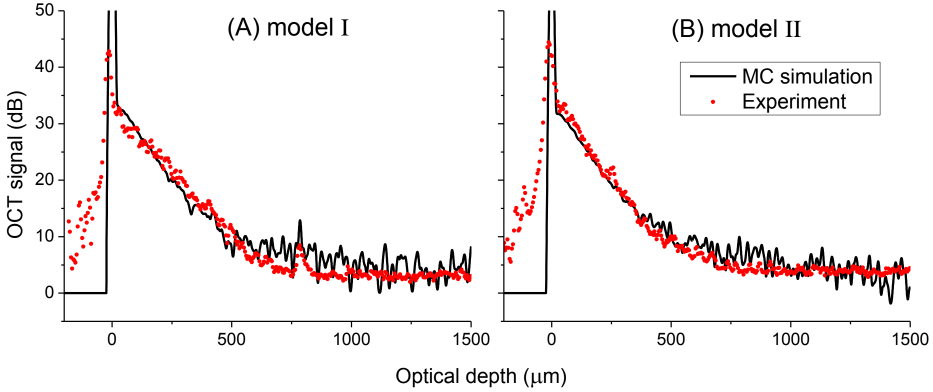

Fig. 59. Quantitative comparisons between the experimental (red) and simulated OCT (black) A-scans of model I (smooth surfaces of top layer) and model II (rougher surfaces) of alumina. The experimental data is obtained at λ = 1.7 μm from the average of 50 A-scans extracted from Fig. 57B and Fig. 57D. The simulated A-scans are truncated at a dynamic range of 50dB in this figure.

In Fig. 60 we see that there is an excellent quantitative agreement also for the zirconia sample with 375 μm geometrical thickness of the top layer.

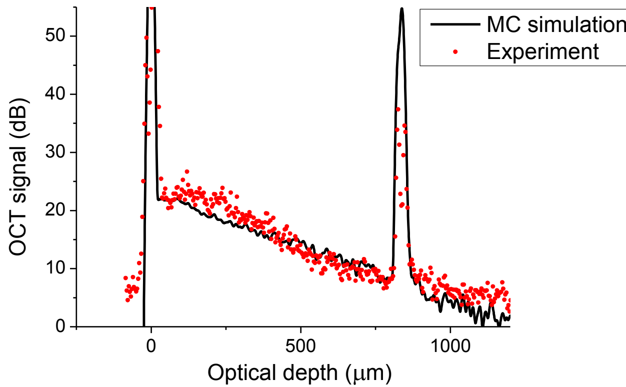

Fig. 60. Quantitative comparison between the measured (red) and simulated (black) OCT A-scans for zirconia at λ = 1.7 μm. The averaged A-scan was extracted from the OCT data in Fig. 49.

We have thus demonstrated that a good quantitative agreement is achieved between the experimental measurements and the Monte Carlo simulation of OCT images of the ceramic

materials. It is important to point out that this agreement is obtained without any fitting of the optical parameters to the experimental data. Thus, the simulation is accurate enough for providing further analysis and predictions in this study.

8.3 Simulated near- to mid-IR OCT images for alumina

Fig. 61 shows the simulated images of model I ($\delta_{rms} = 30$ nm) for alumina at five different wavelengths. It is obvious that the trend is an improved probing depth with increasing wavelength originating from the wavelength dependence of the optical properties of alumina, namely, μ_s and g. The intensity gradient of the 450μm-thick top layer attenuates more quickly at $\lambda = 1.3$ μm than at 4 μm. i.e. the scattering is weaker and the g value is smaller, giving a more evenly distributed scattering. The imaging contrast of the embedded boundaries is also considerably enhanced.

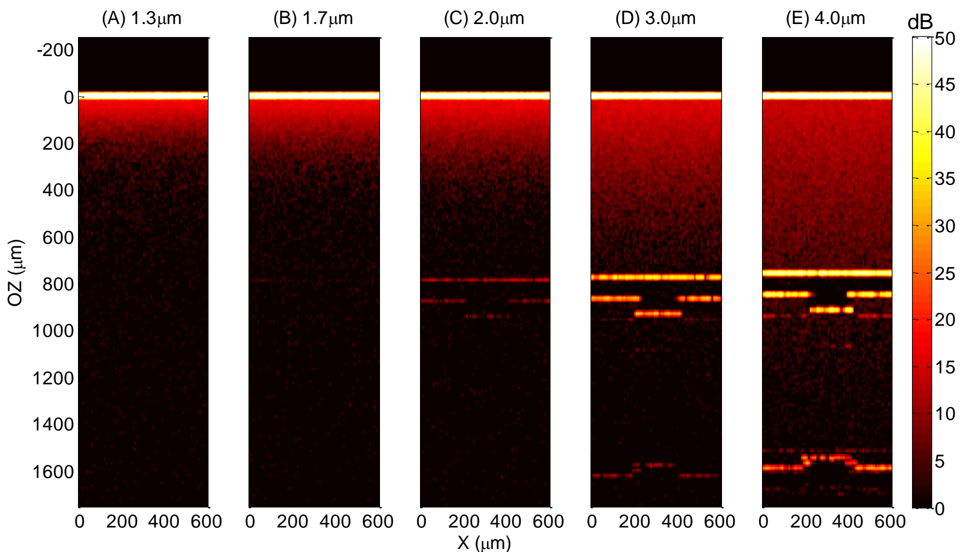

Fig. 61. Simulated OCT images of alumina obtained by model I (30 nm rms surface roughness of the upper 450μm-thick layer) for the five indicated wavelengths. The vertical axis represents the optical distance (OZ) as shown to the far left and the color-coded calculated intensity is given to the far right. The inverted channel signature appearing at the bottom boundary at 3 and 4 μm is caused by the shorter optical path through the air filled channel (black).

Fig. 61A and Fig. 61B should be compared with the measured OCT images Fig. 57A and Fig. 57B. The simulations and measurements show that 1.3 μm OCT cannot detect any embedded boundary at the bottom of the uppermost layer. At $\lambda = 1.7$ μm the rear boundary of the top layer (S2), located at the optical depth $OZ \approx 785$ μm, can be traced but it appears very weak and it has poor contrast, similar to the experimentally measured image in Fig. 57B.

In addition to the improved probing depth we also note a mirrored image of S3 just 90 μm (optical distance) beneath that surface. This is caused by a double reflection between S2 and S3, and a similar result is observed in the measured image shown in Fig. 56. At $\lambda = 4$ μm the transparency of alumina is large. Therefore, we observe image artefacts of S2 and S3 that are mirrored by the top surface S1 and they appear at $OZ = 1500$ μm and $OZ = 1680$ μm.

Another phenomenon is the distorted image of the flat surface S4 as observed in Fig. 61D and Fig. 61E. An inverted channel is shown in the image instead of a straight line because the photons passing through the air-filled channel have travelled a shorter optical pathlength to reach and return from this boundary at the channel region. The image distortion can easily be calculated as the optical path difference, but it also shows how easily OCT images can be misinterpreted by the human visual perception.

As our major concern is inspection of industrial ceramic materials, the surfaces of multiple layers in a ceramic device are of major interest to measure. Fig. 62 demonstrates the simulated OCT images of model II for alumina at the five different wavelengths. In this case the two surfaces of the top layer have an rms roughness $\delta_{rms} = 90$ nm, corresponding to the un-polished alumina sample. We find that the embedded surfaces cannot be detected at all at $\lambda = 1.3$ μm and 1.7 μm. This agrees well with the measured results obtained as the images Fig. 57C and Fig. 57D. Although the probing depth can be seen to be gradually improved with increasing wavelength, the influence of the roughness of the top layer is obvious. The OCT signals of all embedded boundaries drop and the discontinuity of each boundary is more pronounced due to large-angle scattering at the surfaces.

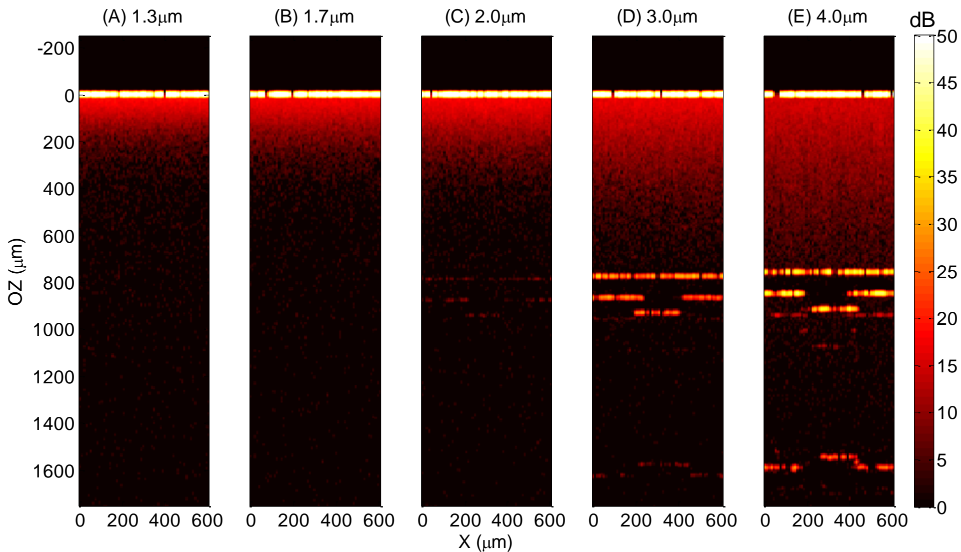

Fig. 62. The same simulation as in Fig. 61 but now using model II, with a roughness of 90 nm rms of the surfaces of the upper layer appearing at optical distances $OZ = 0$ and around 780 μm.

8.4 Simulated near- to mid-IR OCT images for zirconia

As a final demonstration of the predicted performance of OCT imaging at mid-IR wavelengths we present in Fig. 63 and Fig. 64 the simulated results for zirconia. The same geometric models I and II in Fig. 58 are applied for the zirconia ceramic material in order to have a direct comparison with the alumina material. It is therefore not directly comparable with the experimental data which is obtained from a 375 μm layer. In Fig. 63 we demonstrate the simulated OCT images of model I for zirconia at the four wavelengths, 1.3 μm, 1.7 μm, 2 μm and 3 μm. Similar to the alumina case the improvement of the probing depth is obvious with increasing wavelength up to $\lambda = 2$ μm. But then, it comes to a limit as the difference is quite small between Fig. 63C and Fig. 63D. From the optical properties (Table 6) we can predict that the simulation at 4 μm would not improve the probing depth further for this type of zirconia.

Again, we observe the mirrored images of S3 just 90 μm beneath itself due to double or even triple reflections, as well as the mirrored images of S2 and S3 at

$OZ = 1950$ µm and $OZ = 2130$ µm. We also observe the distorted image (inverted channel profile) of S4 caused by the shorter optical path through the air filled embedded channel. Moreover, the scattering in zirconia at $\lambda = 2$ and 3 µm is much weaker compared to that in alumina. Thus, the mirrored image artefacts around $OZ = 2000$ µm become more pronounced, and interfere with the already distorted image of S4, which makes the image recognition and therefore the boundary detection very difficult.

By comparing Fig. 61 and Fig. 63 it is obvious that the embedded boundaries are more easily found in the zirconia material. The differences are particularly large at $\lambda = 1.3$ µm, 1.7 µm and 2 µm, where the scattering coefficients of the alumina sample are much larger than for the zirconia sample. Also, it is obvious that the OCT signal slope for the zirconia material is smaller, particularly for longer wavelengths due to smaller corresponding scattering coefficient values.

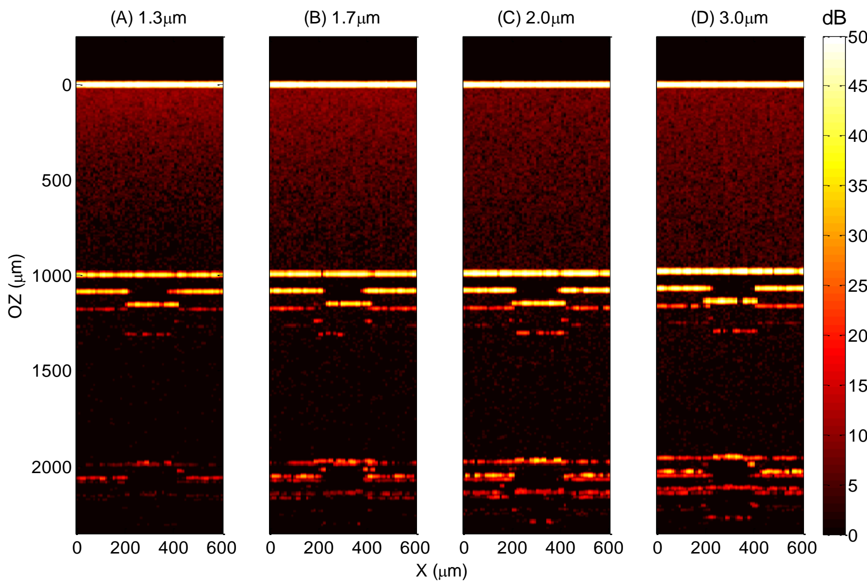

Fig. 63. Simulated OCT images of the smoother surface model I for zirconia at four different wavelengths. The vertical axis represents the optical distance as shown to the far left and the color-coded calculated intensity is given to the far right. The complex structure at OZ ~2000 µm is caused by multiple reflections and variations in the optical path lengths because of the air-filled channel.

The simulated OCT images of model II for zirconia at the same four wavelengths are shown in Fig. 64. The influence of surface roughness is apparent as the images of the embedded boundaries become fuzzy and fragmented. The mirrored image artefacts due to multiple reflections are attenuated very much in this case. By comparing Fig. 62D and E with Fig. 64B, which have very similar μ_s and g values, we can see that the influence of surface roughness is larger when the refractive index is considerably higher, as it is in zirconia. In addition, it is more difficult to detect the channel with surface roughness $\delta_{rms} = 140$ nm in the zirconia case as shown in Fig. 64. This means that the detection of embedded boundaries does not only depend on the probing depth, limited by the bulk scattering, but also depend on the roughnesses of the surfaces through which the radiation is transmitted and the surfaces from which it is reflected.

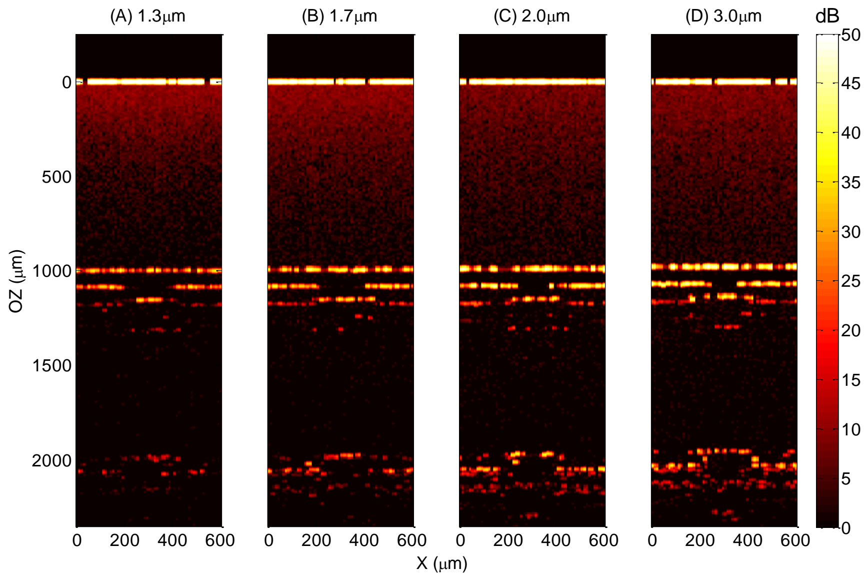

Fig. 64. The same simulation as in Fig. 63 but now using model II, with a roughness of 90nm rms of the surfaces of the upper layer appearing at optical distances $OZ = 0$ and around 1000 μm.

9 Discussions

> "An expert is someone who knows some of the worst mistakes that can be made in his subject, and how to avoid them."
>
> Werner Heisenberg

A significant aim of this thesis is to study the measurement uncertainty in OCT caused by various optical phenomena, such as light scattering, diffraction, refraction, and reflection. Therefore, in this chapter we discuss the measurement uncertainty in OCT qualitatively and quantitatively on the basis of our experimental measurements and simulation results. The accuracy of our image processing method is evaluated first in section 9.1. The analyses and discussions of the measurement results on the ceramic samples are followed up in section 9.2, as are typical artefacts and ambiguities appearing in OCT imaging.

9.1 Evaluation of the developed image processing algorithm

In metrology, the science of measurement, we usually avoid speaking of accuracy in a measurement as we do not know the true answer, and cannot tell how close we are to the correct value. Rather we calculate a total uncertainty based on a number of uncertainty contributions to a real measurement. For traceable artefacts we can have a very good reference or nominal value to compare with. The overall "accuracy" is

then quantitatively indicated by comparing the nominal value with the measured value. In the case of OCT measurements the discrepancy between these values is caused by: a) the uncertainty of the OCT system due to optical and mechanical imperfections and environmental influence; and b) the uncertainty due to the image processing algorithm, and c) the uncertainty introduced by unknown non-uniformities in refractive indices of the investigated sample. These three sources are not easy to evaluate separately. Therefore, the image processing is also qualitatively evaluated by human visual observations. For quantitative evaluation of image processing algorithms we are lacking standard guidelines, particularly for OCT images. Thus, we will start the evaluation with discussion of the terminology.

9.1.1 Discussion of the terminology

There is a lack of standard terminology for describing goodness of algorithms quantitatively. That relates to the difficulty in finding suitable metrics which provide an objective measure of performance. We define the following indicators with reference to Wirth et al. [142] for evaluating our algorithm. Note that these indicators are not defined and used in exactly the same way as the metrology terminology [33].

1) Accuracy: States how well the algorithm has performed with respect to some reference images or human visual observations;

2) Reliability: The degree to which an algorithm, yields the same result when operated several times on images of a reference sample; the reliability is expressed as the standard deviation of the measured and analyzed results from these images;

3) Sensitivity: How responsive an algorithm is to small changes in features;

4) Robustness: An algorithm's capacity for tolerating various image qualities;

5) Adaptability: How the algorithm deals with variability in images;

6) Efficiency: The practical viability of an algorithm (computational time and memory space).

It is important to mention that when the measured boundaries, e.g. surfaces of the measured object, are well separated in depth, the sub-pixel accuracy of the positions of these boundaries can be derived far better than the nominal A-scan OCT axial resolution (see Table 8). This is due to the fact that the locations of the boundaries are obtained as the peak positions of the low-coherence interferometric signals.

However, the OCT axial resolution is determined by the point spread function (PSF) of the source, which does not directly determine the peak position of the PSF of the boundary. A common mistake that can be found in OCT literature is the use of axial resolution as an indicator for the accuracy and precision of an OCT system.

9.1.2 Evaluations based on OCT B-scans

The technical details of this evaluation can be found in paper 7. In this work we have implemented traceable gauge blocks to test the performance of the algorithm. Two pieces of ceramic gauge blocks [140] (height standard) make up an accurate step height of 1.005mm. The maximum permissible error (MPE) is 0.4µm in height. The layout of the gauge blocks arrangement is shown in Fig. 65 and the OCT imaging profile is marked with the red line.

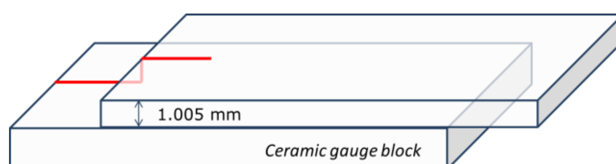

Fig. 65. Layout of the gauge blocks.

In Fig. 66 the OCT image of the 1.005 mm step and the segmented result obtained from our ridge algorithm are shown. The measurement is repeated with the gauge blocks slightly moved in order to test the reliability of our algorithm. The tilt compensated result is reported in Table 8, as the average value of the measured step heights (with 99.7% confidence level) from several different OCT images. The reliability is obtained as the standard deviation of the measured values. This value, ±0.9 µm, should be compared with the theoretical axial resolution of < 20 µm, as given in Table 1. Thus it is obvious that with a high performance algorithm, as the one we have developed, the possibility of accurately finding surface boundaries are strongly enhanced and performs well beyond the nominal OCT resolution.

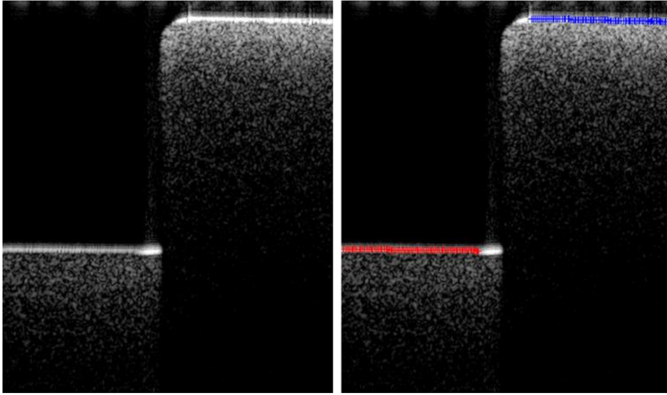

Fig. 66. Cross-sectional OCT image of the step height of the ceramic gauge blocks (left), and the small crosses represent the extracted boundaries with sub-pixel precision (right). (Wellman laboratory 1.3 μm SS-OCT is used. This figure is extracted from paper 7)

Table 8 the step height of the ceramic gauge blocks

Nominal height	1.005 mm ± 0.2 μm
Average Measured height	1.0048 mm ± 1.4 μm
Reliability	±0.9 μm

The sensitivity of our algorithm can also be found in Fig. 53 in section 7.3, where a small delamination of 14.4 μm is detected.

The robustness of our algorithm is tested by using the cross-section OCT image of a single alumina ceramic layer (Fig. 67). Due to the strong scattering of the material the rear surface of the alumina layer can hardly be seen. The local image contrast is extremely low (< 6%) for the rear surface and the SNR is approaching 1 due to speckles. However, our ridge detection algorithm succeeds to extract the two boundaries precisely. The sensitivity of the algorithm is also proved.

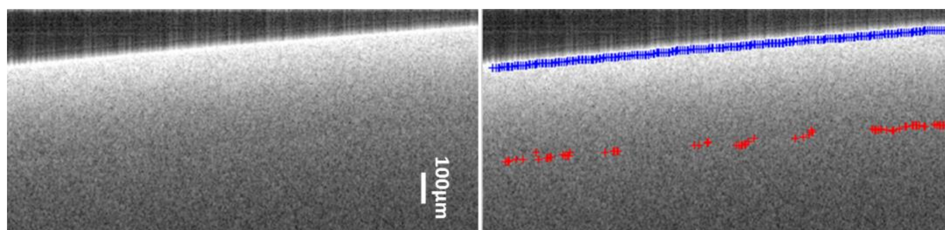

Fig. 67. Cross-sectional OCT image of a single alumina ceramic layer (left) and the image processing result (right). The vertical scale bar represents the optical distance. (Wellman laboratory 1.3 µm SS-OCT)

The algorithm also provides a very good adaptability. This is tested by dealing with arbitrary geometric shapes of the boundaries in OCT images as shown in Fig. 54. Without providing the algorithm with any pre-set model and a priori information, the boundaries of the layers and the embedded feature are extracted. From Fig. 54C it can be clearly seen that the sub-pixel extracted crosses follow the channel boundary with very high precision so that the shape and dimensions of the embedded feature can be easily recognized and calculated.

9.1.3 Evaluations based on volumetric OCT data

An extraordinary feature of our newly developed 3D image processing algorithm is its capability of extracting surfaces from volumetric OCT image, and therefore provide the opportunity for high-accuracy measurement of the features in lateral directions. The accuracy, sensitivity, robustness and adaptability of the algorithm may be evaluated using the volumetric OCT data as shown in Fig. 49. From this data we extract the cross-sectional B-scan shown in Fig. 68. The surfaces are slightly tilted and curved due to the material itself or distortions in the OCT image domain. The latter will be discussed later in section 9.2.2. Moreover, as can be seen in the enlarged image, the rear boundary of the top layer is very close to the top surface surrounding the channels. It is not so easy to resolve these two boundaries by our visual perception system, which is actually very sensitive to small changes in the image. It is even more challenging for an automated computer algorithm to resolve and segment these boundaries, particularly when the requirement of measurement uncertainty is very high.

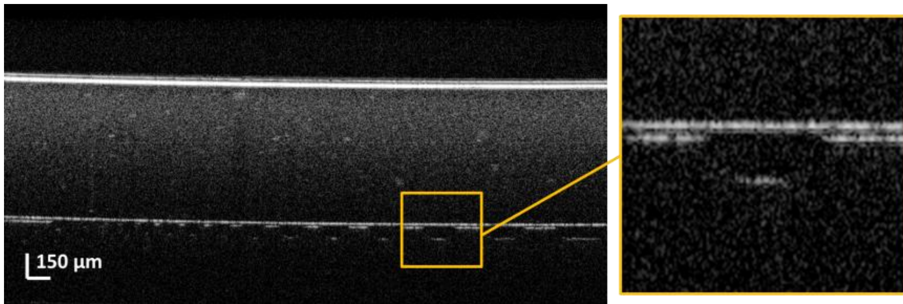

Fig. 68. Cross-sectional OCT image of the microchannels with a 375 µm thick zirconia layer on top. The gray scale represents a dynamic range of 45dB. (Thorlabs TELESTO SD-OCT)

The evaluation is made by comparing the top and bottom surfaces of the channels that are extracted by using our 3D image processing algorithm and by manually selecting and presenting the target planes using conventional image visualization software, e.g. Amira [143]. As shown in Fig. 69 the advantage of our image processing algorithm is obvious, which is much more accurate and time-saving, particularly for non-flat surfaces.

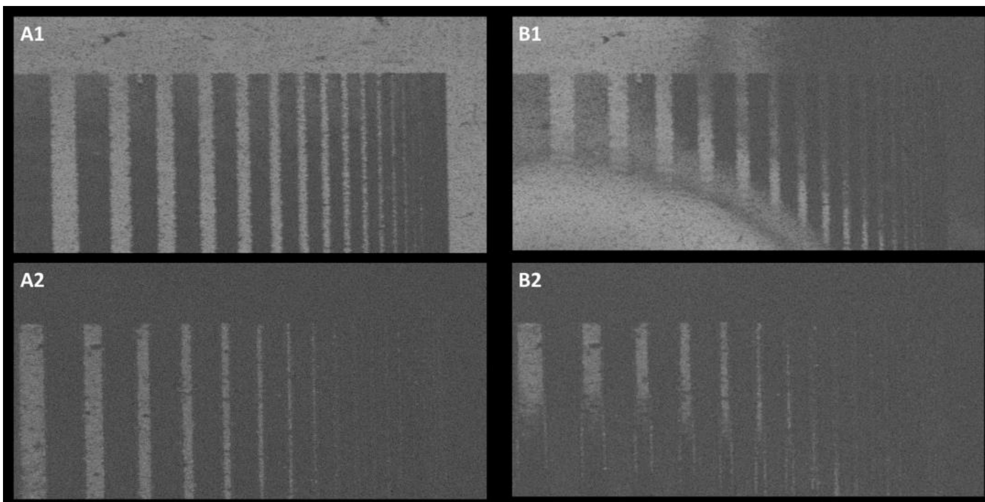

Fig. 69. Comparison of top-view OCT images of the top and bottom surfaces of the microchannels that are extracted by our 3D image processing algorithm (A) and the manual selections of the image planes using Amira (B).

9.2 Measurement uncertainty of OCT in ceramics

In this section we discuss the measurement uncertainty of OCT in both axial and lateral directions through the measurement of the depth and width of the microchannels on free and embedded surfaces. A USAF 1951 resolution test target [144] with flat surface is used for evaluating the lateral measurement uncertainty and the wavefront aberration. A discussion about typical ambiguities in OCT imaging is also included in the last section.

9.2.1 Critical dimension (CD) measurement

The OCT measurement results of depth and width of the microchannels have already been presented in section 7.2. These results are compared with that of the well-calibrated Zygo SWLI for the same channels, of which the average depth is 67.1±0.02 μm. This value agrees very well with the OCT-measured values 66.2±0.1 μm and 66.6±0.1 μm for the channels when measured as free and embedded surfaces, respectively. Thus, we conclude that the OCT measurement is accurate in axial direction and does not introduce any significant error for a measurement of embedded structures in the axial direction. The same conclusion is drawn by evaluating the simulated OCT images in paper 3.

For the measurement in the lateral X- and Y-directions the situation is more complicated. The measured surface profile by SWLI is shown in Fig. 70. In the magnified image shown as Fig. 70C it is seen that the edge of the channel is rough and appears to have cut-outs due to the laser-milling process. The measured standard deviation of the edge profile is 6 μm, where the objective provides a lateral optical resolution of 3.8 μm and 4.36×4.36 mm FOV. We take this measurement (Fig. 70B) as the reference and compare it with the OCT measurement as shown in the upper image of Fig. 33. We then find that the rough profiles of the edges are more blurry in the OCT measurement. The reasons for that may be: a) the lower lateral resolution of OCT which is around 8 μm; b) the relatively higher background noise level; and c) backscattering signal from the bulk material and sidewall of the channel contributes to the edge pixels in the top-view intensity image (Fig. 33), in particular for ceramic materials into which IR radiation can penetrate.

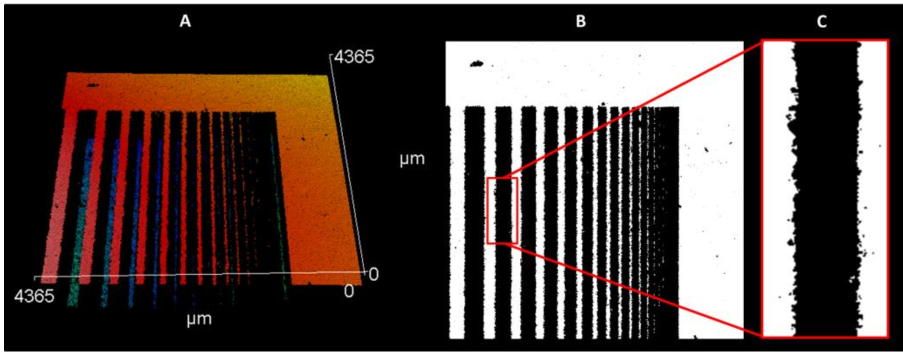

Fig. 70. 3D surface profile of the microchannel layer measured by SWLI (A), the top-view cross-sectional image of the extracted top surface (B), and the enlargement of the marked area (C). The white areas in (B) and (C) correspond to the surface.

The overall effect on the measurement of the channels widths can be found through the quantitative comparison of the measured widths by SWLI and OCT in Fig. 71, where the microchannels are measured on the free surface in both measurements. As can be seen the difference is nearly constant for the selected channels and the average difference is 31 µm.

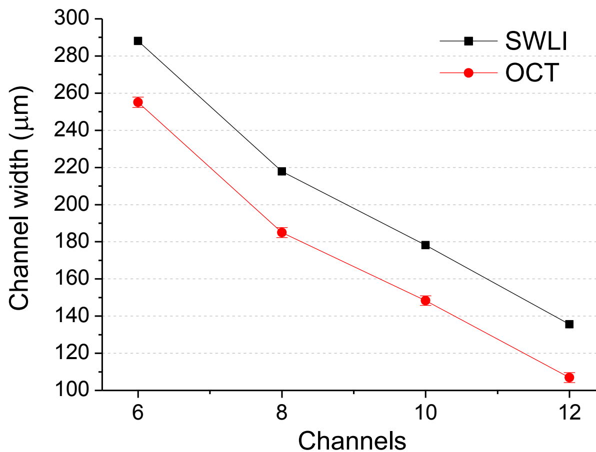

Fig. 71. Graphical comparison of the measured result of the channel widths by the SWLI and the Thorlabs TELESTO SD-OCT. The vertical axis represents the channel width in micrometers and the horizontal axis corresponds to the channels C6, C8, C10, and C12.

The disagreement between SWLI and OCT is probably due to the well-known problem of defining the edge of a microchannel. It is even more complicated when the edges of the microchannels which are rough, just as shown in the microscope image in Fig. 72. More investigations are definitely needed to get a better understanding of how edges are being recognized by different optical equipment. However, this is out of the scope of this thesis and will be a topic of future research. What we have found shows that it is likely to measure position 1 in Fig. 72 as the edges in OCT, whereas the measure of position 2 more represents the edges in the SWLI. Therefore, the former gives smaller values of the channel width.

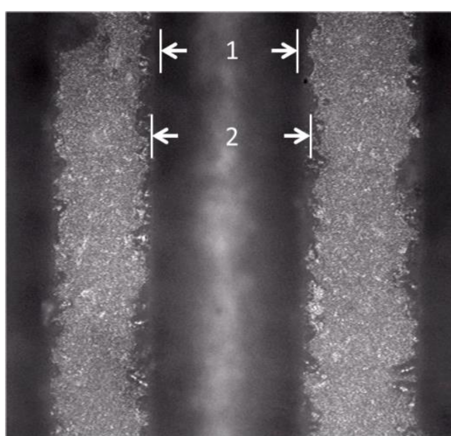

Fig. 72. Optical microscope image of the alumina ceramic microchannel. Light gray corresponds to the focused top surface of the channel. The possible edge positions are marked. The microscope has a scale error < 0.5 % measured vs a calibrated artefact.

For further verification we use the same OCT setup to measure a USAF 1951 resolution test target. The top surface of the test target is extracted using our image processing algorithm and the top-view image is shown in Fig. 73.

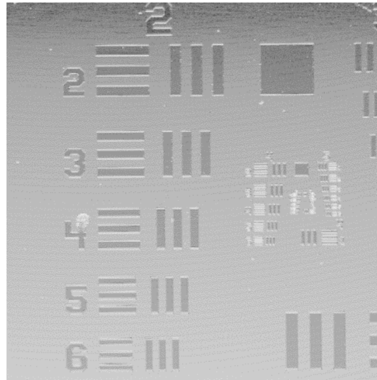

Fig. 73. Top-view gray-scale OCT image of the extracted top surface of the USAF 1951 resolution test target. Dark gray areas correspond to the glass substrate. These edges are much sharper and straighter and the scattering contribution from the chromium film and glass is negligible compared to the ceramic channels as shown in Fig. 72.

The test bars of group 2 and element 1-6 are used for evaluating the measurement uncertainty of the OCT system in lateral directions. The measured line widths, after compensation of the wavefront aberration (see next section) and the tilting angles, are compared with the nominal values in Table 9.

Table 9 Line width in the USAF 1951 resolution test target

Element (Group 2)	1	2	3	4	5	6
Nominal value (μm)	125.00	111.36	99.21	88.34	78.74	70.13
OCT measured value (μm)*	124.7±0.4	106.4±1.7	97.2±1.3	87.7±0.7	77.8±0.4	69.1±0.3

* Measurements are made for lines on glass (the dark gray areas in Fig. 73) with a confidence level of 99.7%.

The error in the measurement of element 2 is slightly larger due to the intensity drop near the upper part of Fig. 73 which is caused by a slight tilting of the sample for avoidance of strong specular reflection. The shrunk line width may also be caused by the uncertainty of edge detection in a gray-scale image. Therefore, we

measure and compare the widths of line pairs (pitches), where the uncertainty of edge detection decreases significantly. The result is shown in Table 10.

Table 10 Width of line pair in the USAF 1951 resolution test target

Element (Group 2)	1	2	3	4	5	6
Nominal value (μm)	250.00	222.72	198.4	176.7	157.5	140.3
OCT measured value (μm)*	251.3±0.4	224.8±1.8	200.0±1.7	177.3±1.0	157.6±0.6	140.6±0.2

* Measurements are made for line pairs on glass and chrome with a confidence level of 99.7%.

As seen in the tables above these lateral measurements agree much better than the ceramic channels do. This is a strong indicator that the ceramic samples themselves are the major reason for the large lateral discrepancies shown in Fig. 71.

To get an idea of the influence of scattering in the top layer on the measured width of the embedded microchannels, a series of tests were made on both alumina and zirconia. The measured results (see section 7.2) are plotted in Fig. 74. The widths of the channels in free surface are represented by black circles and are used here as the reference. The OCT measured widths of the same channels when observed through 188 μm thick alumina and 375 μm thick zirconia are shown as red and blue triangles respectively.

The embedded microchannels are measured to be constantly wider compared to those in free surface. This is probably caused by a reduced backscattering signal from the edges owing to the strong scattering that occurs in the top alumina or zirconia layer, and the presence of surface roughness may enhance this effect as we observed in paper 1. This fact can be observed as a reduced intensity in Fig. 48 and Fig. 51 when compared to Fig. 33. A similar result is obtained when using the Wellman laboratory OCT systems.

It is also interesting to see that the deviation of the channel widths is larger when viewed through the 188 μm thick alumina layer than it is for the 375 μm thick zirconia layer. The reason is that the zirconia layer has a lower scattering coefficient at $\lambda = 1.3$ μm, which corresponds to a statistical mean of 1.2 scattering events in

this layer whereas there are 4.2 scattering events happening in the relatively thinner alumina layer. The channel is therefore likely to be widened furthermore or even disappear in the noise background if the thickness or the scattering coefficient increases.

This result shows that lateral measurements made through a scattering media can be very doubtful, even with ballistic photons as in OCT. Calibration artefacts for OCT with specific thicknesses and optical properties are therefore highly needed.

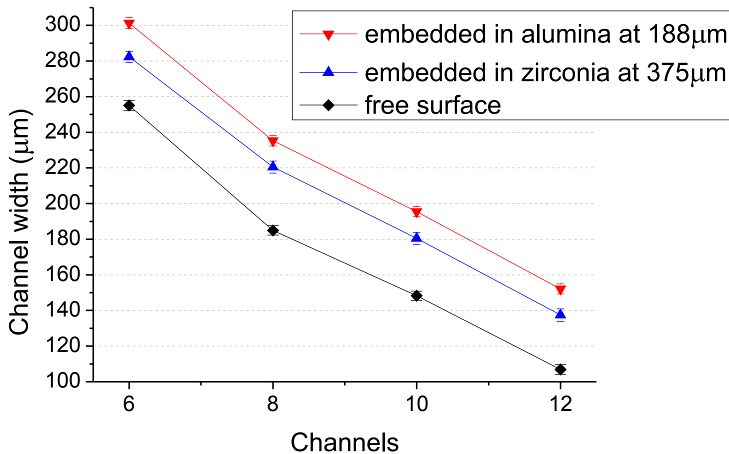

Fig. 74. Graphical comparison of the measured widths of the embedded channels by the Thorlabs TELESTO SD-OCT. The vertical axis represents the channel width in micrometers and the horizontal axis corresponds to the channels C6, C8, C10, and C12.

9.2.2 Ambiguities and errors in OCT imaging

In an OCT image displayed in gray scale the surfaces of the ceramic samples appear as bright continuous boundaries. The ceramic material itself shows an intensity gradient which decreases with the depth and ends up as black or relatively dark areas when no backscattered signal is received. Regions of the material with strong absorption will also appear dark. Shadows created by pores in the axial direction, as shown in Fig. 52, may be misunderstood as an area without any scattering media e.g. an air gap or an area with strong absorption in IR e.g. metallic materials. These

shadows project onto the rear surface of the ceramic layer and leave “holes” on this surface as can be seen in Fig. 75.

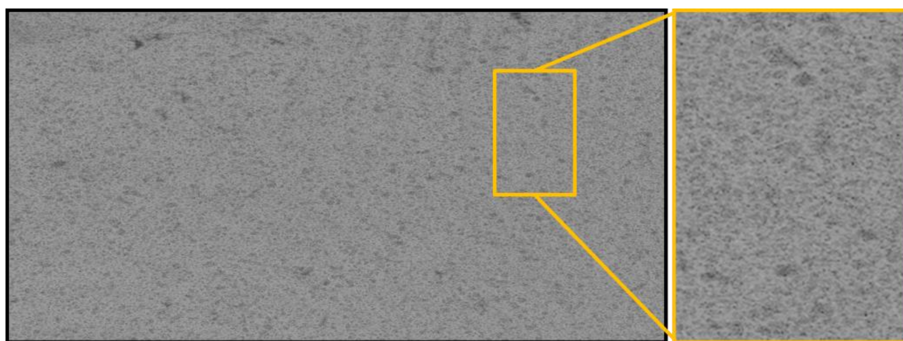

Fig. 75. Top-view gray-scale images of the extracted rear surface of the zirconia top layer corresponding to the sample in Fig. 49. The gray levels correspond to 110 dB dynamic range. The light gray pixels correspond to the surface, whereas the black or dark gray pixels correspond to the shadows created by pores. The image size is 1024×512 pixels for 4×4 mm^2.

The mirrored image artefacts as shown in the experimental OCT image Fig. 56B and in the simulated images in Fig. 61E and Fig. 63D are typical ambiguities in OCT images of industrial ceramic samples. It is caused by multiple reflections between different surfaces or interfaces representing changes in refractive index when the material is relatively transparent at the imaging wavelengths. It may also happen in other industrial samples e.g. printable electronics [79]. It can be problematic in multi-layered structures particularly when each layer is thin and the transparency is relatively high. These additional signals cannot be easily removed by physical means or image processing. Therefore, when OCT is applied for inspection of multi-layered industrial samples the operator must be aware of these phenomena and have necessary knowledge about the geometry and internal structure of the sample.

In the simulated images Fig. 61 and Fig. 63 we observe the image ambiguity as the distorted flat surface S4. In this case the target surface S4 is distorted in the image domain due to the varying refractive index profile above it, i.e. the air filled microchannel makes a shortcut for the incident radiation. This phenomenon is related to the nature of low-coherence interferometry which provides a measure of the optical pathlength of each backscattering and reflection site from a reference

position. The OCT images do not directly correspond to the physical dimensions of the real geometric structures, but they are correlated through the refractive indices of the materials which are similar to scaling factors and extend the physical distance to optical distance in the image. By developing dedicated software this distortion may be compensated for by calculating the optical distance into a physical distance provided the refractive index of the material is known. However, imagine that the refractive index of the material is not homogeneous. Then, the image distortion of the embedded features would be very difficult to be corrected.

Another common problem in OCT imaging is the wavefront aberration caused by the imaging optics, particularly when a pair of galvo mirrors is used for the lateral scanning [44]. This aberration exists in most OCT systems that use this scanning scheme, which is a 3rd-order aberration (astigmatism at zero degree and defocus) corresponding to the 4th Zernike term [145]. When two galvo mirrors are used to scan the light beam across the sample, one of them is at the focal distance of the imaging lens, the other one, however, is not. This problem is usually downsized by setting the focal point between the two mirrors. Therefore aberrations can be found in both x- and y-directions. For some scanning schemes the peak-to-valley (P-V) error can be as large as some 20 μm over a 4×4 mm^2 FOV. Of course many OCT systems have dedicated post processing algorithms for correcting this error, but the remaining error may still be larger than the typical criterion of $\lambda/4$ (corresponding to 0.33 μm for $\lambda = 1.3$ μm) if the FOV is large. In this thesis we have developed an accurate and robust way to correct the wavefront aberration by extracting the OCT image of a flat surface using our dedicated 3D image processing algorithm. The actual wavefront can then be presented by the best-fit polynomial function over the FOV as demonstrated in Fig. 76.

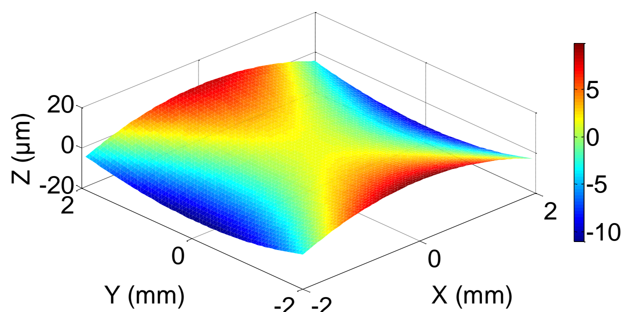

Fig. 76. Plot of the best-fit wavefront of an OCT system which uses a pair of galvo mirrors for the lateral scanning. The FOV is 4×4 mm^2 and the colorbar corresponds to height values in micrometers.

The wavefront aberration can thus be corrected with a high accuracy using our software. However, in the physical measurement the aberration is present and it may propagate in the materials and affect the accuracy of the measured embedded features. How much measurement uncertainty will be added in axial and lateral directions due to this aberration is out of scope of this thesis, but it needs to be investigated for further improvement of the technique.

We have shown that our image processing algorithm is able to retrieve the actual wavefront, based on which a smaller center area of the FOV can be selected to make the P-V deviation satisfy the $\lambda/4$ criterion. A single tip-tilt mirror with coplanar axes and fixed pivot point [146] might provide a promising physical solution by replacing the two-galvo scanning scheme. For roll-to-roll manufacturing processes this problem can be solved by using only one galvo mirror to scan the sample laterally perpendicular to the rolling direction.

9.3 Future work

As we mentioned before most of the commercial and laboratory OCT setups are aimed for biomedical applications, therefore some areas that are worth to develop further for the industrial applications include:

1) Development of proper OCT components, such as light sources and detectors working in the mid-IR region. This will make OCT much more efficient for optical inspection and metrology of ceramic materials as we have shown in chapter 8.

2) Design and development of high-quality test standards with embedded structures that possess traceable geometric dimensions and optical properties, and well-defined edges for CD measurements.

3) Propagation of the measurement uncertainty caused by wavefront aberration in scattering media and its effect on measurements of embedded structures.

4) Improvement of the efficiency of the dedicated image processing algorithms for in-process monitoring of future roll-to-roll manufacturing technology.

5) Thorough research on how different optical equipment responds to physical edges of different materials, to improve lateral measurement uncertainty.

10 Conclusion

In this thesis we investigate and develop the optical coherence tomographic methods and tools for inspection and micrometrology of embedded structures in multi-layered alumina and zirconia ceramics. The aims are to find the optimal OCT wavelengths regions in alumina and zirconia ceramic materials for the detection of embedded features and defects, evaluate the measurement uncertainty in OCT due to different optical phenomena, and develop dedicated image processing algorithms for improving the uncertainty of dimensional measurement.

That has been done by spectrally characterizing scattering by bulk material and surface roughness using spectrophotometry measurements, which reveals the scattering coefficients and g-factors in the wavelength range from visible to 4µm. Two ceramic materials have been experimentally analyzed using state-of-art commercial and laboratory OCT systems operating at 1.3 µm and 1.7 µm wavelengths regions. Based on these results, the geometries of the samples, the experimentally measured surface roughness, and the optical properties have been determined. These parameters were then used to perform Monte Carlo simulations resulting in artificial OCT images over an extended wavelength range. Given by a quantitative agreement with the measured OCT images at 1.3 µm and 1.7 µm, the optimal center wavelength for inspection is predicted to be 4 µm for the alumina samples and 2 µm for the zirconia samples. However, the presence of rough surfaces (δ_{rms}~0.1 µm) will still make the images of embedded boundaries quite fuzzy, and thus affects the accuracy of measuring embedded features.

In order to handle large amounts of volumetric OCT data we have in this thesis for the first time developed a dedicated automated 3D image processing and analysis algorithm with sub-pixel resolution, high accuracy, efficiency, and robustness. It effectively removes noise and speckles, and records only the pixels corresponding to target interfaces. Segmentation of tilted and curved closely adjacent ceramic interfaces with 10 μm distance in z-direction is demonstrated. The method also enables high-accuracy line width, i.e. CD measurements.

Some other factors also affect the accuracy of OCT detection in ceramic materials. Although the axial measurement uncertainty of OCT is verified to be around one micrometer on calibrated gauge blocks in our case, one cannot expect such a good correlation if the refractive indices of the materials are inaccurate or non-uniform. For CD measurements in lateral directions the uncertainty is relatively larger, particularly when the edges of the microchannels are rough and made up of high scatter materials. In this case the definition of edges is not clear and OCT tends to measure a narrower channel by including bulk scattering signals from the ceramic material, whereas SWLI is more likely to measure the very top of the surface only. Moreover, a lateral widening effect is also found when the microchannels are embedded in a scattering media, i.e. alumina or zirconia materials, and the degree of the widening correlates with the mean number of scattering events that occur when a radiation travels through the ceramic layer. This means that lateral measurements made through a scattering media using OCT can be quite doubtful, particularly when we are lacking of knowledge about the material.

In addition, image artefacts are found in OCT images due to multiple reflections between neighboring boundaries and inhomogeneities of refractive index. A wavefront aberration due to defocus and astigmatism caused by the OCT beam-scanning optics is detected by our 3D image processing algorithm, and therefore can be corrected. For roll-to-roll manufacturing processes this problem can be solved by using only one galvo mirror to scan the sample laterally across the rolling direction.

In summary, we have evaluated and improved the performance of OCT as a measurement method. This has been done by developing new software algorithms, methods and tools, for in-process quality inspection and 3D micrometrology. The results are expected to improve the yield in future roll-to-roll manufacturing of multi-layered ceramic structures by immediate feedback from mid-IR sensors and OCT-setups. The methodology developed here may also be adopted in other similar

3D imaging and measurement technologies, e.g. ultrasound imaging, and for various materials, where signal to noise ratios are low in volumetric data.

References

1. Rotary Printing press, Wikipedia. http://en.wikipedia.org/wiki/Rotary_printing_press.
2. S. Bredeau and L. Federzoni, “Multilayer: a large scale production of micro devices via new rolled multi material layered 3D shaping technology”, in *Proceedings of the 4M/ICOMM 2009 Conference*. V. Saile. K.Ehmann and S. Dimov. ed. (Karlsruhe. 2009). pp. 419-422.
3. C. Barry Carter and M. Grant Norton, *Ceramic Materials: Science and Engineering*, (Springer 2013).
4. R2R-CIGS, FP7 European Union project, http://r2r-cigs.com/.
5. PRODI, FP7 European Union project, http://www.project-prodi.eu/.
6. Fast2Light, FP7 European Union project, http://www.fast2light.org/.
7. ROPAS, FP7 European Union project, http://www.ropas-project.eu/.
8. ROTROT, FP7 European Union project, http://www.ropas-project.eu/.
9. MULTILAYER, FP7 European Union project, http://multilayer.4m-association.org/.
10. A. Kristoffersson and E. Carlström. “Tape casting of alumina in water with an acrylic latex binder”. Journal of the European Ceramic Society. Volume 17. Issues 2-3, pp. 289-297 (1997).
11. S. Bredeau and J. Bancillon. “Opportunities and challenges in room temperature embossing/ punching for ceramic green tapes”. *the Proceedings of the 8th International Conference on Multi-Material Micro Manufacture*. Eds. Bertrand Fillon. Chantal Khan-Malek. Stefan Dimov (2010).
12. G. Delette, S. Bredeau, M. Carriquiry and J. Brancillon, “Numerical studies on the thermo-mechanical behaviour of multilayer ceramics during co-sintering”, the proceedings of the 9th International Conference on Multi-Material Micro Manufacture. Eds. Humbert Noll. Nadja Adamovic and Stefan Dimov. (Vienna, 2012)
13. P. V. Petkov, “Development and implementation of technology for laser micro structuring of rollers”, *the Proceedings of the 8th International Conference on Multi-Material Micro Manufacture*, eds. Bertrand Fillon, Chantal Khan-Malek, Stefan Dimov (2010).

14. P. V. Petkov and A. Kolew, “Process optimisation for laser structuring of ceramic tapes”, *the Proceedings of the 9th International Conference on Multi-Material Micro Manufacture*. Eds. Humbert Noll. Nadja Adamovic and Stefan Dimov. (Vienna, 2012)
15. A. Kucera, S. Ziesche, H. Richter, and T. Moritz, “Green Tapes Developed for Structuring. Lamination and Inmould Labelling”, *the Proceedings of the 9th International Conference on Multi-Material Micro Manufacture*. eds. Humbert Noll. Nadja Adamovic and Stefan Dimov. (Vienna, 2012)
16. A. Kucera, S. Ziesche, D. Jurkow. H. Richter, T. Moritz, and L. Golonka, “Development of Micro Fluidic Component by Embossing. Laser Ablation and Screen Printing”, *the Proceedings of the 9th International Conference on Multi-Material Micro Manufacture*. Eds. Humbert Noll. Nadja Adamovic and Stefan Dimov. (Vienna, 2012)
17. C. Pecharromán, G. Mata-Osoro, L. A. Díaz, R. Torrecillas, and J. S. Moya, “On the transparency of nanostructured alumina: Rayleigh-Gans model for anisotropic spheres”, Opt. Express 17. pp. 6899-6912 (2009).
18. R. Apetz and M. P. B. van Bruggen. “Transparent alumina: a light-scattering model”, J. Am. Ceram. Soc. 86. pp. 480-486 (2003).
19. J. Klimke, M. Trunec and A. Krell, “Transparent Tetragonal Yttria-Stabilized Zirconia Ceramics: Influence of Scattering Caused by Birefringence”, Journal of the American Ceramic Society. 94: pp. 1850–1858 (2011).
20. T. Wriedt, “Mie Theory 1908-2008. Introduction to the conference”, in Mie Theory 1908-2008. Present developments and interdisciplinary aspects of light scattering, eds. T. Wriedt. W. Hergert, Universität Bremen, Bremen 2008, pp.17-21.
21. Hulst. H. C. van de, *Light scattering by small particles*. (New York. Dover Publications. 1981).
22. C. F. Bohren and D. R. Huffman, Absorption and Scattering of Light by Small Particles. (Wiley-VCH. 1998).
23. M. I. Mishchenko, L. D. Travis, and A. A. Lacis, *Scattering, Absorption, and Emission of Light by Small Particles*. (Cambridge University Press. 2002).
24. I. Yamashita and K. Tsukuma. “Light scattering by residual pores in transparent zirconia ceramics”, Journal of the Ceramic Society of Japan. Vol. 119 (2011) No. 1386 (February), pp. 133-135.
25. J. G. J. Peelen and R. Metselaar, “Light scattering by pores in polycrystalline materials: Transmission properties of alumina”, J. of Appl. Phys. **45**. pp. 216-220 (1974).

26. J. G. J. Peelen, “Alumina: sintering and optical properties”, doctoral thesis, Technische Hogeschool Eindhoven (1977).
27. A. A. Kokhanovsky, “Single light scattering: Bubbles versus droplets”, American Journal of Physics, 72, pp. 258-263 (2004).
28. J. M. Bennett and L. Mattsson, “Introduction to Surface Roughness and Scattering”, Optical Society of America: 2nd edition (June 1999).
29. A. Krywonos, “Predicting surface scatter using a linear systems formulation of non-paraxial scalar diffraction”, PhD thesis, the University of Central Florida, Orlando, Florida (2006).
30. J. Caron, J. Lafait, and C. Andraud, “Scalar Kirchhoff's model for light scattering from dielectric random rough surfaces”, Optics Communications. Volume 207. Issues 1-6. 15 June 2002. pp. 17-28.
31. J. Caron, C. Andraud and J. Lafait, “Radiative transfer calculations in multilayer systems with smooth or rough interfaces”, Journal of Modern Optics. Vol. 51. Iss. 4. 2004.
32. M. Nieto-Vesperinas, A. J. Sant, J. C. Dainty, and J. A. Sánchez-Gil, “Light transmission from a randomly rough dielectric diffuser: theoretical and experimental results”, Opt. Lett. 15. pp. 1261-1263 (1990).
33. L. Mattsson, V. Schulze, and J. Schneider, “Quality assurance and metrology”, *Ceramics Processing in Microtechnology* (Whittles Publishing. 2009), Chap. 22.
34. R. E. Chinn, *Ceramography: Preparation and Analysis of Ceramic Microstructures*. (Wiley, March 2006).
35. J. Gegner, “2D-3D conversion of object size distributions in quantitative metallography”, http://www.ariel.ac.il/sites/conf/MMT/MMT-2006/Service_files/papers/Session_3/3-138_2d.pdf.
36. G. V. Voort, “Introduction to Stereological Principles”, http://vacaero.com/information-resources/metallography-with-george-vander-voort/1137-introduction-to-stereological-principles.html.
37. A. Baddeley and E. B. V. Jensen, *Stereology for Statisticians*, (Chapman & Hall/CRC 2005).
38. S. Vasić, B. Grobéty, J. Kuebler, T. Graule and L. Baumgartner, “X-ray computed micro tomography as complementary method for the characterization of activated porous ceramic preforms”, Journal of Materials Research. 22. pp. 1414-1424 (2007).

39. M. Stuer, P. Bowen, M. Cantoni, C. Pecharroman and Z. Zhao, "Nanopore Characterization and Optical Modeling of Transparent Polycrystalline Alumina", Adv. Funct. Mater. 22: pp. 2303-2309 (2012).
40. L. Holzer and M. Cantoni, *Review of FIB-tomography*, (Oxford University Press 2012), chapter 11, pp.410-435.
41. J. Manara, R. Caps, F. Raether, and J. Fricke, "Characterization of the pore structure of alumina ceramics by diffuse radiation propagation in the near infrared", Opt. Commun. 168. pp. 237-250 (1999).
42. J. H. Nobbs, "Kubelka—Munk Theory and the Prediction of Reflectance", Review of Progress in Coloration and Related Topics. 15: 66–75 (1985).
43. D. Huang, E. A. Swanson, C. P. Lin, J. S. Schuman, W. G. Stinson, W. Chang, M. R. Hee, T. Flotte, K. Gregory, C. A. Puliafito, and J. G. Fujimoto, "Optical coherence tomography", *Science*. 254. 1178–1181 (1991).
44. J. M. Schmitt, "Optical coherence tomography (OCT): a review", Selected Topics in Quantum Electronics. IEEE Journal of. **5**. 1205-1215 (1999).
45. B. E. Bouma and G. J. Tearney, *Handbook of Optical Coherence Tomography*. (Marcel Dekker. 2002).
46. A. F. Fercher, W. Drexler, C. K. Hitzenberger, and T. Lasser, "Optical coherence tomography--principles and applications", Rep. Prog. Phys. 66. 239-303 (2003).
47. W. Drexler and J. G. Fujimoto, eds., *Optical Coherence Tomography Technology and Applications*. (Springer Berlin Heidelberg New York 2008).
48. D. Stifter, "Beyond biomedicine: a review of alternative applications and developments for optical coherence tomography", Appl. Phys. B 88. 337–357 (2007).
49. M. Bashkansky, M. D. Duncan, M. Kahn, D. Lewis III, and J. Reintjes, "Subsurface defect detection in ceramics by high-speed high-resolution optical coherent tomography", Opt. Lett. 22. 61-63 (1997).
50. M. D. Duncan, M. Bashkansky, and J. Reintjes, "Subsurface defect detection in materials using optical coherence tomography." Opt. Express 2. 540-545 (1998).
51. M. Bashkansky, D. Lewis III, V. Pujari, J. Reintjes, and H. Y. Yu, "Subsurface detection and characterization of Hertzian cracks in Si_3N_4 balls using optical coherence tomography." NDT E Int. 34. 547-555 (2001).
52. J. Veilleux, C. Moreau, D. Lévesque, M. Dufour, and M. I. Boulos. "Optical coherence tomography for inspection of highly scattering ceramic media: glass powders and

plasma-sprayed coatings." Review of Quantitative Nondestructive Evaluation 25. 1059-1066 (2006).

53. C. Sinescu, A. Bradu, M. Hughes, M. L. Negrutiu, C. Todea, et al. "Quality assessment of dental treatments using en-face optical coherence tomography", J. Biomed. Opt. 13(5). 054065 (2008).
54. W.A. Ellingson, R.J. Visher, and R.S. Lipanovich, "Optical NDT Techniques for Ceramic Thermal Barrier Coatings", Materials Evaluation (2006).
55. I. Grulkowski, J. J. Liu, B. Potsaid, V. Jayaraman, J. Jiang, J. G. Fujimoto, and A. E. Cable, "High-precision. high-accuracy ultralong-range swept-source optical coherence tomography using vertical cavity surface emitting laser light source", Opt. Lett. 38. 673-675 (2013).
56. U. Sharma, E. W. Chang, and S. H. Yun, "Long-wavelength optical coherence tomography at 1.7 μm for enhanced imaging depth." Opt. Express 16. 19712-19723 (2008).
57. C. S. Cheung, M. Tokurakawa, J. M. O. Daniel, W. A. Clarkson and H. Liang. "Long wavelength optical coherence tomography for painted objects". Proc. SPIE 8790. Optics for Arts. Architecture. and Archaeology IV. 87900J (May 30. 2013).
58. E. Rosen and K. Peterson, "Non-Destructive Evaluation of Gas Turbine Thermal Barrier Coatings". in the Proceedings of the First International Symposium on Optical Coherence Tomography for Non-Destructive Testing. Linz. Austria. 13-14 February 2013.
59. P. M. Moselund, C. Petersen, S. Dupont, C. Agger, O. Bang and S. R. Keiding, "Supercontinuum: broad as a lamp. bright as a laser: now in the mid-infrared." Proc. SPIE 8381. Laser Technology for Defense and Security VIII. 83811A (May 7. 2012).
60. Type II Super Lattice detector. IRnova AB. http://www.ir-nova.se/t2sl.
61. J. M. Schmitt, S. H. Xiang and K. M. Yung. "Speckle in optical coherence tomography." J. Biomed. Opt. **4**. 95-105 (1999).
62. C. K. Hitzenberger, A. Baumgartner, and A. F. Fercher. "Dispersion induced multiple signal peak splitting in partial coherence interferometry." Opt. Commun. 154. 179-185 (1998).
63. C. K. Hitzenberger, A. Baumgartner, W. Drexler, and A. F. Fercher. "Dispersion effects in partial coherence interferometry: implications for intraocular ranging". Biomed Opt. 1999. 144-51.

64. A.F. Fercher, C.K. Hitzenberger, M. Sticker, R. Zawadzki, B. Karamata, T. Lasser, “Dispersion compensation for optical coherence tomography depth-scan signals by a numerical technique”, Optics Communications, 204(1-6), pp. 67-74 (2002).
65. M. Maciejewski, M. Strąkowski, J. Pluciński, B. B. Kosmowski, “Dispersion compensation in optical coherence tomography”, Proc. SPIE 6347, Photonics Applications in Astronomy, Communications, Industry, and High-Energy Physics Experiments 2006, 63471K.
66. M. Bashkansky and J. Reintjes. “Statistics and reduction of speckle in optical coherence tomography”. Opt. Lett. 25. 545-547 (2000).
67. M. Pircher, E. Götzinger, R. Leitgeb, A. F. Fercher and C. K. Hitzenberger. “Speckle reduction in optical coherence tomography by frequency compounding”. J. Biomed. Opt. 8(3). 565-569 (2003).
68. N. Iftimia, G. J. Tearney, and B. E. Bouma, “Speckle reduction in optical coherence tomography by “path length encoded” angular compounding”. J. Biomed. Opt. 8(2). 260-263 (2003).
69. J. Kim, D. T. Miller, E. Kim, S. Oh, and J. Oh, et al. “Optical coherence tomography speckle reduction by a partially spatially coherent source”. J. Biomed. Opt. 10(6). 064034 (2005).
70. A. Ozcan, A. Bilenca, A. E. Desjardins, B. E. Bouma, and G. J. Tearney, “Speckle reduction in optical coherence tomography images using digital filtering,” J. Opt. Soc. Am. A 24. 1901-1910 (2007).
71. J. A. Eichel, A. K. Mishra, D. A. Clausi, P. W. Fieguth and K. K. Bizheva, “A novel algorithm for extraction of the layers of the cornea,” in 2009 Canadian Conference on Computer and Robot Vision, F. Ferrie, M. Fiala, eds. (IEEE. 2009). pp. 313-320.
72. M. K. Garvin, M. D. Abràmoff, X. Wu, S. R. Russell, T. L. Burns, and M. Sonka, “Automated 3-D intraretinal layer segmentation of macular spectral-domain optical coherence tomography images,” IEEE Transactions on Medical Imaging 28, 1436-1447 (2009).
73. V. Kajić, B. Považay, B. Hermann, B. Hofer, D. Marshall, P. L. Rosin and W. Drexler, “Robust segmentation of intraretinal layers in the normal human fovea using a novel statistical model based on texture and shape analysis,” Opt. Express 18. 14730-14744 (2010).

74. I. Ghorbel, F. Rossant, I. Bloch, S. Tick and M. Paques, “Automated segmentation of macular layers in OCT images and quantitative evaluation of performances,” Pattern Recognit. 44. 1590–1603 (2011).
75. A. Mishra, A. Wong, K. Bizheva and D. A. Clausi, “Intra-retinal layer segmentation in optical coherence tomography images,” Opt. Express 17. 23719-23728 (2009).
76. M. Kass, A. Witkin, and D. Terzopoulos, “Snakes: active contour models,” Int. J. Computer Vision 1(4). 321-331 (1988).
77. A. Fard, C. Wang, O. Malik, G. Fu, A. Quach, K. Goda and B. Jalali, “Near-100 MHz optical coherence tomography at 800 nm,” presented at the First International Symposium on Optical Coherence Tomography for Non-Destructive Testing, Linz, Austria, 13-14 February 2013.
78. M. Wojtkowski, “High-speed optical coherence tomography: basics and applications,” Appl. Optics 49, D30-D61 (2010).
79. J. Czajkowski, P. Vilmi, J. Lauri, R. Sliz, and T. Fabritius, et al. “Characterization of ink-jet printed RGB color filters with spectral domain optical coherence tomography”, Proc. SPIE 8493. Interferometry XVI: Techniques and Analysis. 849308 (September 13, 2012);
80. L. Thrane, T. M. Jørgensen, M. Jørgensen, F. C. Krebs, “Application of optical coherence tomography (OCT) as a 3-dimensional imaging technique for roll-to-roll coated polymer solar cells”, Solar Energy Materials and Solar Cells, Volume 97, February 2012, pp. 181-185.
81. Y. Ahn, W. Jung and Z. Chen, “Optical sectioning for microfluidics: secondary flow and mixing in a meandering microchannel”, Lab on a Chip, Issue 1, 2008.
82. D. Stifter, E. Leiss-Holzinger, Z. Major, B. Baumann, M. Pircher, E. Götzinger, C. K. Hitzenberger, and B. Heise, “Dynamic optical studies in materials testing with spectral-domain polarization-sensitive optical coherence tomography,” Opt. Express 18, 25712-25725 (2010).
83. M. Strąkowski, J. Pluciński, B. B. Kosmowski, “Multilayered structures examination using polarization sensitive optical coherence tomography”, Photonics Letters of Poland, Vol. 1, No. 2 (2009).
84. A. Dubois, K. Grieve, G. Moneron, R. Lecaque, L. Vabre, and C. Boccara, “Ultrahigh-Resolution Full-Field Optical Coherence Tomography,” Appl. Opt. 43. 2874-2883 (2004).

85. W. Drexler, "Ultrahigh-resolution optical coherence tomography", J. Biomed. Opt. 9(1). 47-74 (Jan 01, 2004).
86. T. Chen, N. Zhang, T. Huo, C. Wang, and J. Zheng. et al., "Tiny endoscopic optical coherence tomography probe driven by a miniaturized hollow ultrasonic motor", J. Biomed. Opt. 18(8). 086011 (Aug 16, 2013).
87. A. Prylepa1, J. Duchoslav, T. Keppert, G. Luckeneder, K.-H. Stellnberger, and D. Stifter, "Nonlinear imaging with interferometric SHG microscopy using a broadband 1550 nm fs-fiber laser", in the Proceedings of the 1st International Symposium on Optical Coherence Tomography for Non-Destructive Testing. Linz. Austria. 13-14 February 2013.
88. A. S. Birks, and R. E. Green, *Ultrasonic Testing 2nd ed* (Columbus. 1991).
89. P. Zinin and W. Weise, "Theory and applications of acoustic microscopy", in *Ultrasonic Nondestructive Evaluation: Engineering and Biological Material Characterization*, T. Kundu. ed. (CRC Press. Boca Raton. 2003)
90. N. Chawla, J. J. Williams, X. Deng, C. McClimon, L. Hunter, and S. H. Lau, "Three-dimensional characterization and modeling of porosity in powder metallurgical steels," Int. J. Powder Metall. **45**. 19-28 (2009).
91. S. R. Stock, MicroComputed Tomography: Methodology and Applications. (CRC Press. 2008).
92. R. Nagata, C. R. Appoloni and J. S. Fernandes, "Determination of sic ceramic foams microstructure properties by x-rays microtomography", 2009 International Nuclear Atlantic Conference - INAC 2009 Rio de Janeiro, RJ, Brazil. September27 to October 2, 2009.
93. J. P. Kruth, M. Bartscher, S. Carmignato, R. Schmitt, L. De Chiffre, and A. Weckenmann, "Computed tomography for dimensional metrology", CIRP Annals - Manufacturing Technology, Volume 60, Issue 2. 2011, pp. 821-842.
94. S. Carmignato, "Accuracy of industrial computed tomography measurements: Experimental results from an international comparison", CIRP Annals - Manufacturing Technology, Volume 61, Issue 1. 2012, pp. 491-494.
95. B. M. Patterson and C. E. Hamilton, "Dimensional Standard for Micro X-ray Computed Tomography", Analytical Chemistry 2010 82 (20), 8537-8543.
96. S. Carmignato, D. Dreossi, L. Mancini, F. Marinello, G. Tromba and E. Savio, "Testing of x-ray microtomography systems using a traceable geometrical standard", 2009 Meas. Sci. Technol. 20 084021.

97. B. D. Evans and M. Stapelbroek, “Optical properties of the F+ center in crystalline Al2O3”, Phys. Rev. B 18. 7089-7098 (1978).
98. J. Vallayer, C. Jardin, and D. Tréheux, “Optical and dielectric behaviors of alumina after an electromagnetic irradiation”, Optical Materials, Volume 16, Issues 1-2, February–March 2001, pp. 329-333.
99. M. Matysiak, J. P Parry, F. Albri, J. G. Crowder, N. Jones, K. Jonas, N. Weston, D. P. Hand and J. D. Shephard, “Infrared confocal imaging for inspection of flaws in yttria-stabilized tetragonal zirconia polycrystal (Y-TZP)”, 2011 Meas. Sci. Technol. 22 125502.
100. S. Wang and X. Zhang, “Pulsed terahertz tomography”, J. Phys. D: Appl. Phys. 37 R1-36 2004.
101. M. Jewariya, E. Abraham, T. Kitaguchi, Y. Ohgi, M. Minami, T. Araki, and T. Yasui, “Fast three-dimensional terahertz computed tomography using real-time line projection of intense terahertz pulse”, Opt. Express 21. 2423-2433 (2013).
102. Terahertz measuring technology for non-destructive testing of materials, Fraunhofer Institute for Physical Measurement Techniques IPM, http://www.ipm.fraunhofer.de/en/terahertz.
103. K. Kawase, T. Shibuya, K. Suizu and S. Hayashi, “Terahertz-wave generation for industrial applications”, Terahertz Physics, Devices, and Systems IV: Advanced Applications in Industry and Defense, edited by Mehdi Anwar, Nibir K. Dhar, Thomas W. Crowe, Proc. of SPIE Vol. 7671. 76710P.
104. C. Chen, D. Lee, T. Pollock, and J. F. Whitaker, “Pulsed-terahertz reflectometry for health monitoring of ceramic thermal barrier coatings”, Opt. Express 18. 3477-3486 (2010).
105. M. Born and E. Wolf, *Principles of Optics*. (New York: Pergamon Press. 1980:265).
106. B. Povazay, K. Bizheva, A. Unterhuber, B. Hermann, H. Sattmann, A. F. Fercher, W. Drexler, A. Apolonski, W. J. Wadsworth, J. C. Knight, P. St. J. Russell, M. Vetterlein, and E. Scherzer, “Submicrometer axial resolution optical coherence tomography”, Opt. Lett. 27. 1800-1802 (2002).
107. V. R. Shidlovski and J. Wei, “Superluminescent diodes for optical coherence tomography”, Proc. SPIE4648, Test and Measurement Applications of Optoelectronic Devices, 139 (April 18, 2002).
108. J. W. Goodman, *Statistical Optics* (Wiley-Interscience, 1985).

109. M. A. Choma, and M. V. Sarunic, and C. Yang, and J. A. Izatt, “Sensitivity advantage of swept source and Fourier domain optical coherence tomography”, Optics Express, 11 (18), pp. 2183-2189 (2003) .

110. J. F. de Boer, B. Cense, B. H. Park, M. C. Pierce, G. J. Tearney, and B. E. Bouma, “Improved signal-to-noise ratio in spectral-domain compared with time-domain optical coherence tomography”, Opt. Lett. 28. 2067-2069 (2003).

111. R. Leitgeb, C. Hitzenberger, and Adolf Fercher, “Performance of fourier domain vs. time domain optical coherence tomography”, Opt. Express 11. 889-894 (2003).

112. S. Yun, G. Tearney, J. de Boer, N. Iftimia, and B. Bouma, “High-speed optical frequency-domain imaging”, Opt. Express 11. 2953-2963 (2003).

113. J. Plucinski, P. Wierzba, and R. Hypszer, “Fiber optic sensor based on optical frequency domain reflectometry”, Proc. SPIE 5028, Optical Fibers and Their Applications VIII, 155 (April 14, 2003).

114. G. Häusler and M. W. Lindner, ““Coherence Radar” and “Spectral Radar” - New Tools for Dermatological Diagnosis”, J. Biomed. Opt. 3(1). 21-31 (Jan 01. 1998).

115. S. Yun, G. Tearney, B. Bouma, B. Park, and Johannes de Boer, “High-speed spectral-domain optical coherence tomography at 1.3 μm wavelength”, Opt. Express 11. 3598-3604 (2003).

116. R. Bracewell, “The Sifting Property”, in *The Fourier Transform and Its Applications, 3rd ed.* (New York: McGraw-Hill, pp. 74-77, 1999).

117. G. M. Hale and M. R. Querry, “Optical Constants of Water in the 200-nm to 200-μm Wavelength Region”, Appl. Opt. 12. 555-563 (1973).

118. L. L. Carter, and E. D. Cashwell, “Particle-transport Simulation With the Monte Carlo Method”, January 01, 1975.

119. I. Lux and L. Koblinger, Monte Carlo particle transport methods: neutron and photon calculations.

120. S. A. Prahl, M. Keijzer, S. L. Jacques, A. J. Welch, “A Monte Carlo model of light propagation in tissue”, SPIE Proceedings of Dosimetry of Laser Radiation in Medicine and Biology, IS 5. 102-111 (1989).

121. L. Wang, S. L. Jacques, and L. Zheng, “MCML-Monte Carlo modeling of photon transport in multi-layered tissues,” Comput. Meth. Programs Biomed. **47**. 131-146 (1995).

122. J. Pluciński, A. F. Frydrychowski, “New aspects in assessment of changes in width of subarachnoid space with near-infrared transillumination/backscattering sounding, part 1: Monte Carlo numerical modeling”, J Biomed Opt., 12(4):044015 (2007).
123. M. Kirillin, “Optical coherence tomography of strongly scattering media”, Doctoral thesis, Faculty of Technology, University of Oulu (2008).
124. A. Tycho, T. M. Jørgensen, H. T. Yura, and P. E. Andersen, “Derivation of a Monte Carlo Method for Modeling Heterodyne Detection in Optical Coherence Tomography Systems”, Appl. Opt. 41. 6676-6691 (2002).
125. R. K. Wang, “Signal degradation by multiple scattering in optical coherence tomography of dense tissue: a Monte Carlo study towards optical clearing of biotissues,” Phys. Med. Biol. **47**. 2281-2299 (2002).
126. M. Kirillin, E. Alarousu, T. Fabritius, R. Myllylä and A. V. Priezzhev, “Visualization of paper structure by optical coherence tomography: Monte Carlo simulations and experimental study”, J. Eur. Opt. Soc.-Rapid Publ. 2. 07031 (2007).
127. M. Kirillin, I. Meglinski, V. Kuzmin, E. Sergeeva and R. Myllylä, “Simulation of optical coherence tomography images by Monte Carlo modeling based on polarization vector approach,” Opt. Express 18. 21714-21724 (2010).
128. L. G. Henyey and J. L. Greenstein, “Diffuse radiation in the Galaxy”, Astrophysical Journal. vol. 93. pp. 70-83 (1941).
129. G. Dougherty (ed.), Medical Image Processing: Techniques and Applications, (Springer, 2011).
130. R. C. Gonzalez and R. E. Woods, *Digital Image Processing 3rd edition* (Prentice Hall, 2008).
131. P. Ekberg, “Development of ultra-precision tools for metrology and lithography of large area photomasks and high definition”, Doctoral thesis, KTH Royal Institute of Technology, Stockholm (2011).
132. Swerea IVF, “Ceramic materials”, Swerea IVF, Mölndal (head office), P. O. Box 104. SE-431 22 Mölndal, Sweden, http://swerea.se/en/.
133. D.T. Pham, S.S. Dimov, and P.V. Petkov, “Laser milling of ceramic components”, International Journal of Machine Tools and Manufacture, 47. March 2007. pp. 618-626.
134. D. Karnakis, G. Rutterford, M. Knowles, T. Dobrev, and P. Petkov, et al. “High quality laser milling of ceramics, dielectrics and metals using nanosecond and picosecond lasers”, Proc. SPIE 6106. Photon Processing in Microelectronics and Photonics V. 610604 (March. 2006).

135. I. H. Malitson, F. V. Murphy, and W. S. Rodeny, “Refractive index of synthetic sapphire,” J. Opt. SOC. Am. 48. 72 (1958).

136. D. L. Wood, and K. Nassau, “Refractive index of cubic zirconia stabilized with yttria”, Appl. Opt. 21. 2978-2981 (1982).

137. A. Roos, “Use of an integrating sphere in solar energy research,” Sol. Energy Mater. Sol. Cells 30. 77-94 (1993).

138. Thorlabs OCT systems, http://www.thorlabs.com/.

139. Zygo NewView7300 3D optical surface profiler, http://www.zygo.com/?/met/profilers/newview7000/

140. T. Doiron and J. Beers, *The Gauge Block Handbook* (National Institute of Standards and Technology. 2009).

141. S. K. Kachigan, *Statistical Analysis* (Radius Press, 1986).

142. M. Wirth, M. Fraschini, M. Masek, and M. Bruynooghe, “Performance evaluation in image processing”, EURASIP J. Adv. Sig. Pr. 2006, 1-4 (2006).

143. Amira, 3D Analysis Software for Life Sciences, http://www.vsg3d.com/amira/overview.

144. 1951 USAF resolution test chart, http://en.wikipedia.org/wiki/1951_USAF_resolution_test_chart.

145. J. C. Wyant and K. Creath, “Basic Wavefront Aberration Theory for Optical Metrology”, in *Applied Optics and Optical Engineering, Volume XI*. Edited by Robert R. Shannon and James C. Wyant. (Academic Press, Inc., New York, 1992).

146. S-334 Miniature Piezo Tip/Tilt-Mirror, Physik Instrumente (PI) GmbH & Co. KG, http://www.physikinstrumente.com/en/products/prdetail.php?sortnr=300710.

Errata – paper 3

Location: equation (1).

Written:

$$n = \left(1 + \frac{1.023798 \times \lambda^2}{\lambda^2 - 0.00377588} + \frac{1.058264 \times \lambda^2}{\lambda^2 + 0.0122544} + \frac{5.280792 \times \lambda^2}{\lambda^2 - 321.3616}\right)^{\frac{1}{2}}$$

Should be:

$$n = \left(1 + \frac{1.023798 \times \lambda^2}{\lambda^2 - 0.00377588} + \frac{1.058264 \times \lambda^2}{\lambda^2 - 0.0122544} + \frac{5.280792 \times \lambda^2}{\lambda^2 - 321.3616}\right)^{\frac{1}{2}}$$

Location: at the end of the second paragraph in section 2.3.1.

Written: Using this model, the coefficients of diffuse transmittance (T_d) and reflectance (R_d) in a non-absorbing sample of thickness l can be calculated as follows.

Should be: Using this model, the coefficients of total transmittance (T_d) and reflectance (R_d) in a non-absorbing sample of thickness l can be calculated as follows.